JUMR

Journal for Undergraduate Materials Research

Promoting Undergraduate Research

The Voice of Future Scientists and Engineers

Featuring Research from

Massachusetts Institute of Technology
University of Kentucky
Virginia Tech

A Publication of the Department of Materials Science and Engineering at Virginia Tech

Volume 5 | 2015

Welcome Letter

Dear Colleagues,

The Journal for Undergraduate Materials Research Editorial Board is pleased to present Volume 5. JUMR is a platform for undergraduate students to present their research. We are proud to be part of this organization that provides a bridge for interdisciplinary involvement by our authors from a variety of departments and universities. This issue includes papers from Materials Science and Engineering, Biomedical Engineering, and Chemistry Departments. In future volumes, we hope to continue providing materials research publishing opportunities for undergraduates students of diverse disciplines and universities.

The JUMR Volume 5 issue was led by a new editorial board. The editorial staff was a team assembled from departments including Architecture, English, Business and Engineering. JUMR provides the unique opportunity for student board members to be involved in the publication process. The goal of the journal is to support the undergraduate authors so that they may be able to present their research in a peer-reviewed journal. It is impressive to see the type of research undergraduates have been able to accomplish, ranging from fundamental theory to applications in engineering. The organizations represented by the undergraduate researchers in this volume are well-represented and should be proud of the work those students have done.

With the publication of JUMR Volume 5, the Editorial Board would like to thank our reviewers, faculty advisors and authors. Furthermore, we are excited to begin preparations for JUMR Volume 6. As we transition into the future, we are working toward electronic publication of the journal and wider accessibility.

Again, thank you for supporting our journal. Our readers and our contributors make possible these opportunities for students to develop and display their professional skills.

Sincerely,
The JUMR Editorial Board

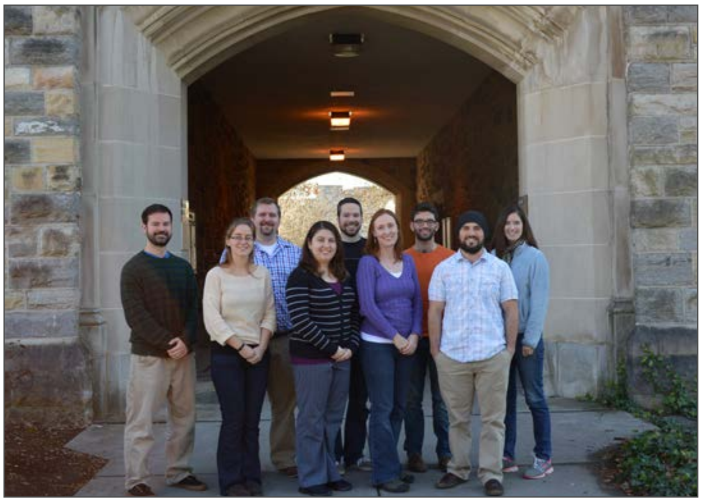

Back Row (L-R): Johan Foster, Cameron Crowell, Andrew Pfaff, Olivia Wilson **Front Row**: Josh Stuckner, Rose Roberts, Kayla McNabb, Kelly Stinson-Bagby, Andrew Schultz **Not Pictured**: Simon Babin, Rachel Corell, Steve Seichepine, Michelle Czamanke, LeeAnn Ellis, Nicholas Chartrain, Kris Shen, Elizabeth Bonnell

On the Cover

The cover features the author Priya Venkatraman holding a polyurethane film containing cellulose nanocrystals. Film provided by Ainara Saralegi and photograph taken by Johan Foster. Front cover edited by B Bagby.

Disclaimer

The views, opinions, and findings contained in the enclosed works are those of the individual authors. The publisher, editors, and authors assume neither responsibility nor liability for errors or any consequences arising from the use of the information contained herein. Mention of trade names or commercial products does not constitute endorsement or recommendations for use by the publishers, editors, or authors.

Final determination of the suitability of any information, procedure, or product for use contemplated by any user, and the manner of that use, is the sole responsibility of the user. This collection of works is intended for informational purposes only. Expert advice should be obtained at all times when implementation is being considered, particularly where hazardous materials or processes are encountered.

Journal of Undergraduate Materials Research (ISSN 1934-7677)
Copyright © 2016 by the Virginia Tech Department of Materials Science and Engineering.

Contents

FEATURE ARTICLES

RESEARCH ARTICLES

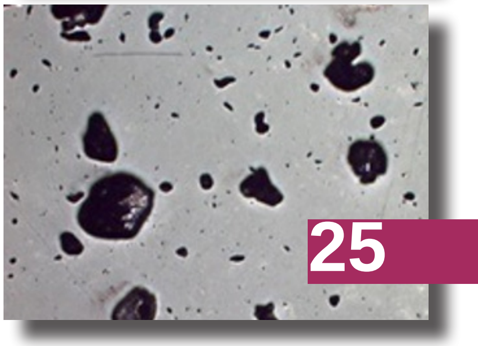

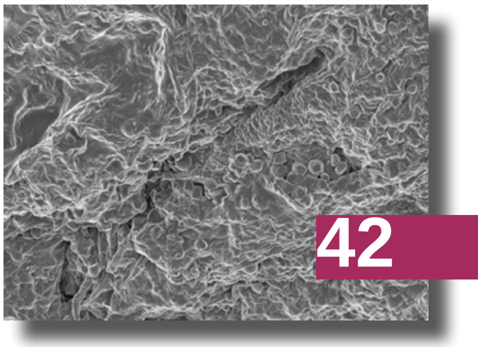

Industry Reviewers:

Terryl Wallace, NASA Langley Research Center

Mia Siochi, NASA Langley Research Center

Jennifer Brooks, Polymer Solutions

Faculty Reviewers

Dr. Reza Mirzaeifar, Mechanical Engineering, Virginia Tech

Dr. Sean McGinnis, Material Science and Engineering, Virginia Tech

Dr. George Scherer, Civil and Environmental Engineering, Princeton

Dr. Thomas Staley, Material Science and Engineering, Virginia Tech

Dr. Diane Folz, Material Science and Engineering, Virginia Tech

Special Thanks:

Materials Science and Engineering Department, Virginia Tech

Architecture Department, Virginia Tech

MSE Communications Program, Virginia Tech

Virginia Tech Foundry Institute for Research and Education

Diane Folz, Materials Science and Engineering

Student Editorial Board

Editor	Kelly Stinson-Bagby Materials Science and Engineering
Assistant Editor and Feature Articles Manager	Kayla McNabb Instructional Design and Technology
Assistant Editor and Data Manager	Rose Roberts Materials Science and Engineering
Production Manager	Andrew Pfaff Materials Science and Engineering
Assistant Production Manager	Andrew Schultz Materials Science and Engineering
Assistant Feature Articles Manager	Rachel Corell English
Operations Manager	Cameron Crowell Materials Science and Engineering
Design and Layout Editor	Simon Babin Architecture
Assistant Operations Manager	Josh Stuckner Materials Science and Engineering
Support Staff	Olivia Wilson Steve Seichepine Michelle Czamanske LeeAnn Ellis Nicholas Chartrain Kris Shen Elizabeth Bonnell

Faculty Advisory Board

Johan Foster
JUMR Faculty Advisor, Materials Science and Engineering

Alex Aning
Materials Science and Engineering

David Clark
Materials Science and Engineering

Letter from the Department Head

David Clark, Materials Science and Engineering

Dear Students and Colleagues:

Have you ever asked yourself what got you involved in Materials Science and Engineering? For many of us, the answer is the same—a mentor, advisor, or friend who shared their excitement of the discipline with us. Professor Larry Hench is responsible for my choosing MSE as a career. I was an average student with a burning desire to do something to change the world in a positive way. Larry helped me to believe that I could achieve that dream. He did the same for countless others. What makes MSE unique and indispensable is the diversity of people and ideas that it represents. Our ranks include physicists, chemists, mathematicians, computational scientists, theoreticians, doctors, lawyers, astronauts, and of course engineers. What we have in common is our enthusiasm and love for research and discovery. The expression on Priya Venkatraman's face on the cover of this volume captures this enthusiasm perfectly.

Each year I conduct face to face exit interviews with our seniors. In addition to the typical questions regarding employment and graduate school, I also ask them what they enjoyed most about MSE. Always at the top of the list is their laboratory and research experiences. The quality of research resulting from these experiences, especially the senior design capstone courses, is excellent and could provide a valuable resource to the larger materials community. This brings me to the reason that the JUMR was started and why it plays an important role in our future. The JUMR was designed to foster enthusiasm in the youth of our discipline by providing them with a venue to publish their research. Like other journals, publication is not guaranteed. Every paper is carefully critiqued and returned to the student author for any necessary modifications. The editorial board, comprised of graduate students and a faculty advisor, makes the final determination regarding publication.

Although the JUMR began as a local publication for Virginia Tech undergraduates, it has quickly evolved to include research articles from undergraduates at other universities. The range of topics covered in this volume illustrates the diversity of our discipline. I believe that you will be impressed with the quality of the research and communication skills that our undergraduates are receiving. The faculty are to be commended for their mentorship of these students. There is no doubt that many of these students will be inspired to continue their efforts thereby insuring the future of our fantastic discipline.

I would like to close with a special tribute to my mentor and advisor, Larry Hench. He was best known for his research in biomaterials, especially for his discovery of Bioglass. I first met Larry when I was a sophomore and he was an assistant professor. I was very close to dropping out but Larry convinced me that engineering and science through research was the pathway to a better future. Two days after meeting Larry for the first time I was working side by side with him in the laboratory helping to develop a new fiber glass insulation. The excitement of being part of a team developing something useful for society was contagious. That excitement has never faded. Sadly, he passed away in December 2015, leaving a legacy that will live for decades and continue to transform the lives of many individuals.

David Clark

David E. Clark
Professor and Head
Materials Science and Engineering
Virginia Tech

VTFire: Casting the Future

By: Geoffrey Merritt

Photography By: LeeAnn Ellis

Concealed in the depths of Plantation Drive, at the end of a long country road lined with cattle and farmland scenery from the Virginia Tech agricultural department lies Virginia Tech's Foundry Institute for Research and Education (VT FIRE). VT FIRE is a relatively new program at Virginia Tech having been established in the spring of 2011, it aims to teach students the fundamentals of foundry operation, equipment, and safety as well as the art of metallurgical design. In the past 4 years, VT FIRE has grown and prospered immensely due to the continued interest of college students in areas such as metal casting and alloying as well as the experience of Dr. Alan Druschitz. For four and a half years, Dr. Druschitz has continued to accomplish more growth, and attract new students, developing an entire metal castings minor around the extensive list of courses the foundry has to offer. Dr. Druschitz, in addition to earning a Ph.D. in metallurgical engineering, has had prior real world experience in industry. This benefits the students by having the opportunity to learn how to operate the various types of foundry equipment safely and effectively, a proficiency that could prove valuable in many future careers.

The foundry is home to a wide variety of metallurgical equipment. When walking through the double doors leading to the foundry room, the first noticeable thing is the large overhead crane sitting high above in the tall ceilings. This convenient piece of equipment makes pouring large amounts of molten metal in huge stone crucibles a piece of cake, opening up the amount of options available for metal casting capabilities. The foundry is also home to two large induction furnaces, a large sand mixer for creating molds of up to 650 lbs. in weight, a dust collection fume system to provide clean breathable air, a 3D printer for creating small intricate molds and many other top of the line machines that complete the full foundry experience. During all operation at the foundry one must adhere to strict safety guide lines that include facemasks, safety glasses, fire proof aprons, jackets, and leather boots. Safety is an important aspect in any industrial setting but it is especially significant in the presence of large quantities of highly dangerous molten metal and substantial amounts of heat generated by the large furnaces. When in operation, this can all seem a little overwhelming at first, but over/time the foundry can become an exciting and interesting place to experience and explore valuable real world applications in metallurgy.

There is an undeniable need for metallurgists in today's economy, having the experience the foundry provides can make any young engineer look attractive to many major engineering fortune five hundred companies.

This practical experience is what attracted me towards the foundry as a material science student. Having already committed towards a minor in green engineering, I was unable to take any of the classes the foundry had to offer. With this realization I sought out Dr. Druschitz himself to see if he needed any research assistants at the foundry, stressing my interest in gaining experience in a foundry environment. He allowed me to assist in steel quenching research conducted with him at the foundry. I was looking at how changing the ratio of the steel quench bath size to the size of your sample and initial quench bath temperature can affect the acquired internal and surface cooling rates of steel. By producing models from this data, one can produce an effective means of acquiring specific cooling rates desired for hardening purposes in the quenching and heat treatment process. I enjoyed the experience I gained in not only the theoretical aspects of the data we collected, but also the operation of the furnaces and creating the quench baths. I believe it will undoubtedly benefit me in years to come after college. Above all, I learned how to conduct myself in a foundry setting, which I believe gave me both the experience and confidence that I needed in order to consider pursing a job in the metallurgical engineering industry.

Although VT FIRE has proven itself to be a self-standing and beneficial program to both students and the university, continued support and contributions are always appreciated. Donations and funding are put towards furthering the foundry's capabilities for the growing number of students and future possibilities for metallurgy related materials research. In the past 4 years the foundry has already gained notoriety as a fun and exciting place as well as a reputation for excellence in all things metallic. Students gain the ability and freedom to conduct fun personal projects, such as casting life-size versions of brass Iron Man masks and aluminum Halo helmets, among many other cool castings. The foundry has room and time to grow before it reaches true adulthood, but the progress it has achieved in the last few years has been impressive to say the least.

Geoffrey Merritt, Materials Science and Engineering, Virginia Tech

Biomorphic Materials: Silicon Carbide Derived from Natural Carbon Precursors

By: Wyatt Surbey

The recent initiative to cater toward an environmentally efficient lifestyle has put pressure on many industries and practices. However, the success of these green initiatives has not been an easy achievement. During the past decade, scientists and engineers have worked tirelessly to discover a more natural way to process Silicon Carbide (SiC). A new category of materials, called biomorphic materials, has provided insight into how materials can be synthesized from bio-organic materials while retaining similar properties and performance.[1] In comparing SiC with its biomorphic cousin, BioSiC, there are notable similarities and differences in the properties, structure, processing, performance, and environmental concerns between each material discussed in this article.

Properties and Structure

SiC (also known as carborundum[2]), is a ceramic material with multitudes of industrial applications. The industrial applications range from use as an abrasive (SiC cutting blades) to use as a semiconducting material (SiC microchips). Properties of SiC include high hardness, high strength, thermal stability, oxidation resistance, and erosion resistance.[3] The high thermal and electrical stability of SiC have allowed it to be accepted as a wide band gap (WBG) semiconductor.[3] A WBG semiconductor allows for "smaller, faster, more reliable, and more efficient" electronic components.[4] SiC also "has the highest [chemical] corrosion resistance of all advanced ceramics".[2] Each of these properties support the performance of SiC in high temperature and abrasive technological applications. SiC has many different crystalline structures (polytypes). There are over two hundred polytypes of SiC, which contribute to slight alterations in the properties of SiC. The most common polytype is alpha SiC which has a hexagonal crystalline structure.[3] Each polytype is varied by the stacking sequence of the tetrahedrally bonded SiC bilayer.[3] This allows for differences in band gap energies and electronic properties of each polytype.

The differences in the properties of SiC and BioSiC are very minimal because the biomorphic properties of BioSiC mimic the properties of SiC. BioSiC behaves as a ceramic material, but its microstructure (Figure 1) and properties are determined by the material it is derived from.[5] The similar structure of BioSiC to SiC allows BioSiC to retain important properties such as high conductivity and other WBG classifications. BioSiC is mainly hexagonal as well but its dependency on the natural material it is derived from (wood, bamboo, etc.) cause the Si to infiltrate the amorphous C scaffolding differently when processing BioSiC. However, an advantage of the natural derivation is that BioSiC and other biomorphic materials tend to interact better with biological systems.[6] The natural derivation of BioSiC imposes advancements in bioelectronics[6] and medical implant technologies[7] that synthetic SiC cannot achieve. BioSiC is more porous and this porosity affects the density of the material, which can lower the overall hardness and strength of BioSiC.[8] However, porosity increases thermal resistivity and insulation which is useful for the electronic applications of BioSiC.

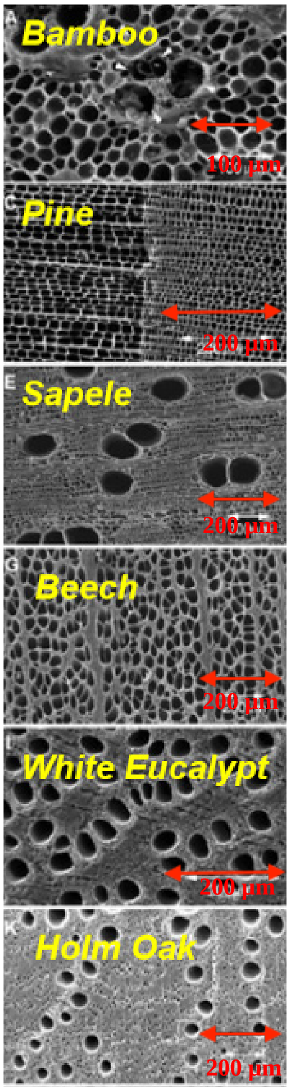

Figure 1: Represents a comparison of the various natural precursors and their final microstructures for BioSiC.[9]

Processing

SiC and BioSiC are processed in fairly different ways. SiC can actually be found in the enviroment naturally as a mineral known as moissanite.[3] Moissanite is rare and only found in certain types of meteorites.[3] SiC is generally syntehetically grown. The many polytypes of SiC result from different processing methods, but the most common ones are known as the Acheson Process and the Lely Method. The Acheson Process is typically used when abrasive properties are desired for SiC. This process involves a solid-state reaction between silica sand and petroleum coke (a solid form of carbon).[3] Processing SiC in this way requires a lot of energy (due to the large furnances) and oxygen, nitrogen, and aluminum impurities are common in the final material.[3]

An alternative method to grow SiC is called phsyical vapor transport (PVT) and one of the first methods using this was called the Lely Method. The Lely Method grows synthetic SiC crystals in an inert gas environment and graphite container at high temperatures.[3] This method consumes less energy (depending on the quanity of crystals to be grown) but is equally as time consuming as the Acheson method.

BioSiC proves some advantages in its processing. One important aspect in processing of BioSiC is that the reneweable or natural material it is made from alters the microstructure and properties of the material. Being derived from renewable materials is also key in considering any environmental concerns of BioSiC. The density of the precursor also has an effect on the final density of the BioSiC and ansiotropic properties.[5] To begin processing BioSiC the cellulose from which the biomorphic material will begin from must be chosen. Cellulose is a natural polymer and the main component of plant cell walls. For purposes of BioSiC, cellulose refers to the type of carbon precursor (examples shown in Figure 1). The next step is pyrolosis, which is a method of separating out C by heating up the carbon precursor in a low-oxygen environment.[5] The carbon precursor is dehydrated of any excess water then higher temeperatures are reached to separate C from the cellulose. At these high temperatures, the cellulose is essentially vaporized from the carbon precursor, leaving a C scaffolding to be infiltrated. The leftover amorphous C may then preciesly machined (this step is optional) to achieve complex shapes prior Si infiltration. Once the machining process is complete, the Si is infiltrated into the C scaffolding using the Si-melt method. This method involves pouring molten silicon over the pyrolyzed carbon so that Si may ifiltrate the pourous microstructure. This reaction is both spontaneous and exothermic.[5] The result of this process is a ceramic matrix composite termed BioSiC which is cooled and can be used in the applications previously described. One advantage in the processing of BioSiC is that this method of pyrolosis and Si-melt infiltration is fairly rapid. The characteristics of BioSiC can be altered easily using this processing method too because the liquid Si is restricted by the precursor's microstructure. This process does not only affect the properties of BioSiC but the performance of BioSiC as well.

Performance

When it comes to the performance of SiC, there are several different applications that are enhanced by this material. SiC performs well under high temperature and conductivity conditions which is why it is generally used for semiconducting wafers.[10] SiC wafers can improve the energy efficiency of solar panels and in some semiconducting three-phase inverters, SiC can withstand temperatures of up to 200°C.[10] Prior to its acceptance in the semiconductor and electronic field, SiC was more traditionally recognized for its abrasive uses. The high strength and thermal resistance of SiC allow it to maintain its properties in high stress applications. The abrasive technologies are mainly utilized for cutting and sanding in industrial workplaces.

One of the main advantages of BioSiC is its "tailorability".[5,7] By being able to change the carbon template of the SiC, there becomes a wide range of performance options for BioSiC. BioSiC exhibits high thermal resistivity and mechanical properties, similar to that of SiC.[5] These properties make BioSiC a competitive replacement for SiC since its processing methods are less expensive and faster. BioSiC can also withstand strengths in a range of 1100-1400 MPa.[5] However, depending on the porosity of the natural precursor the mechanical strength can diminish due to the density of the final product. Increasing porosity also decreases the thermal conductivity of BioSiC.[11] On the other hand, porosity has been advantageous in a study of bone implants. The porosity of BioSiC may mimic that of the porosity of bone making it suseptible to tissue growth.[7] Since BioSiC is a bio-organic material, it has shown improvements toward bioelectronic and biomaterial applications as well.[6]

Environmental Concerns

BioSiC is a more environmentally conscious material than SiC. SiC must be processed at temperatures over 2000°C[3] while BioSiC can be processed at around 1000°C.[5] The low processing temperatures of BioSiC make it a more environmentally conscious material that produces less contamination and uses less energy. Another advantage of BioSiC is that it does not require high-purity starting powder and aditional additives (such as high quality seed-crystals and graphite for growing traditional SiC crystals).[9] The porosity of BioSiC allows it to be manufactured into a recyclable absorbers which can be used for solar power plants. [5] BioSiC absorbers are both more efficient at absorbing heat produced by solar radiation and more cost effective than current ceramic absorbers.[5] Both BioSiC and SiC are generally processed in gas/vapor environments, which can contaminate the air, but BioSiC is processed more rapidly which allows less time for contamination.[5] BioSiC and SiC are also recylable. They can be taken to a ceramic recycling facility where froth floatation, filtration, and centrifugation technologies are used.[12] Most SiC and BioSiC is recycled into grit for abrasive applications.

Conclusion

In comparing SiC and BioSiC there are notable similarities and differences. SiC is processed at higher temperatures and requires more time to generate higher quality and larger crystals. BioSiC is processed at lower temperatures and uses a natural C template that is infiltrated with Si. The mechanical, thermal, and electronic properties of SiC and BioSiC are very similar, resulting in high strength and high thermal resistivity. BioSiC has more diverse applications due to the wide range of natural precursors from which it can be derived. Lastly, BioSiC is more environmentally efficient than SiC due to the lower amount of energy and lack of additives required for its processing. BioSiC is relatively new and future advances are leading the material toward medical implant and recycleable solar panel applications.

References

1. Zhu, J.; Kwong, F. L.; L Ng, D. H. Journal of Nanoscience and Nanotechnology **2009**, 1564-1567.

2. CES Edupak, version 2014; Granta Design: Cambridge, UK, 2014.

3. Abderrazak, H.; Bel Hadj Hmida, E. Silicon Carbide: Synthesis and Properties. In Properties and Applications of Silicon Carbide; In Tech: Rijeka, Croatia, 2011; 361-388.

4. Wide Band Gap Semiconductors: Pursuing the Promise; Technical Report from the U.S. Department of Energy/EE-0910: 2013

5. De Arellano-Lopez, R.; Martinez-Fernandez, J.; Gonzalez, P.; Domingues, C.; Fernandez-Quero, V.; et al. International Journal of Applied Ceramic Technology **2004**, 56-67.

6. Lanzani, G. Nature Materials **2014**, 13, 775-776.

7. Torres-Raya, C.; Hernandez-Maldonado, D.; Ramirez-Rico, J.; Garcia-Ganan, C.; Arellano-Lopez, A.; Martinez-Fernandez, J. Journal of Materials Research **2008**, 3247-3254.

8. Yukhymchuk, V.O.; Kiselev, V.S.; Belyaev, A.E.; Chursanova, M.V.; Danailov, M.; Ya Valakh, M. Functional Materials **2010**, 520-527.

9. Martinez-Fernandez, J.; Quispe, J.; Vicente Garcia Barbosa, J. 12-3: Biomorphic Ceramics Materials for High Temperature and Pressure Industrial Filtration Processes. In IEC Gasification Conference, University of Seville; Technische Universitat Bergakademie Freiberg: Online, 2010.

10. Ozpineci, B.; Tolbert, L. Silicon Carbide: Smaller, Faster, Tougher. IEEE Spectrum [Online] **2011** http://spectrum.ieee.org/semiconductors/materials/silicon-carbide-smaller-faster-tougher/0

11. Johnson, M.T.; Wang, H.; Porter, W.D; Faber, K.T. Composites Science and Technology **2008**, 70(3), 478-484.

12. Sergiienko, S.; Pogorelov, B.; Daniliuk, V. Separation and Purification Technology **2014**, 133, 16-21.

Wyatt Surbey, Materials Science and Engineering, Virginia Tech

Chitosan: An Antimicrobial Polymer

By: Priya Venkatraman

Antibiotic resistant infections are a rising problem in the United States and globally. These infections are listed as a top concern by the Center for Disease Control and Prevention (CDC) as well as by the World Health Organization. Antibiotic resistance is a phenomenon where microorganisms acquire or innately possess resistance to antimicrobial agents. Antibiotic resistant infections significantly reduce the effectiveness of the treatment causing patients to remain infectious longer and increasing the risk of spreading the resistant microorganisms. Antibiotic resistant infections are incredibly detrimental to society and are threatening many of the medical advances made in the past century.[1]

The World Health Organization's 2014 report states that these antibiotic resistant infections are no longer a problem of the future and are in fact impacting the lives of people worldwide currently. The world is headed towards a "post-antibiotic era" where common infections and minor injuries, which have been treatable for decades, can once again lead to disabilities and death.[1] The CDC estimates the annual death toll in the United States alone to be 23,000 and the British government estimates the current death toll worldwide to be 700,000 per year.[1,2] The projected mortality rate by 2050 is to be 10 million annually, which is more than the projected rate for cancer.[2] In addition to higher mortality rates, health care costs significantly increase as more expensive therapies must be sought to treat these antibiotic resistant infections. Furthermore, antibiotic resistant infections are impairing the success of major medical procedures, such as organ transplantation and cancer chemotherapy. These infections can also severely prolong or completely prevent the wound healing process.[3] Due to the imminent risk of these antibiotic resistant infections, an immense amount of research is being done to find new ways of curbing this chronic wound problem. One area of focus has centered on the exploration of biomaterials with antimicrobial properties.

Antimicrobial polymers have emerged as promising deterrents to the spread of antibiotic resistant infections. One polymer known especially for its antimicrobial properties is chitosan. Chitosan, formed by the deacetylation of chitin, is a natural polymer derived from crustacean shells. It is also biocompatible, biodegradable, nontoxic, anti-inflammatory, and anti-fungal, making it an extremely suitable polymer for biomedical applications.[4] The discovery of chitosan dates back to 1859, when Charles Rouget described in his paper the deacetylation of chitin.[5] Following the discovery, research of chitin and chitosan burgeoned in the 1930s and 1940s. The focus of all the research was on the potential bioactivity of chitosan.[4] A major issue with currently available antimicrobial products is their toxicity to mammalian cells. The natural polymer, chitosan, is a solution as it is non-toxic towards mammalian cells and has been shown to be extremely effective against bacteria.[4] However, chitosan does have some drawbacks to being utilized in biological applications.

The use of chitosan is heavily limited by its inability to solubilize in water. Due to excessive hydrogen bonding in the structure, chitosan degrades prior to melting, and therefore, it is necessary to dissolve chitosan in a solvent to impart functionality. Improving the solubility of chitosan is crucial for the material to be used to its full potential. Chitosan has the ability to dissolve only in certain acids such as hydrochloric acid, lactic acid, succinic acid, acetic acid, and formic acid etc. Chitosan is insoluble in water, alkali or aqueous solutions above a pH of 7. The solubility of chitosan has become an essential aspect of antimicrobial research.[4]

Chemical modifications have been attempted to improve its solubility in order to widen its applications.[6] Chemical techniques such as PEG-grafting, sulfonation, partial N-acetylation, chitosan branching with oligosaccharides, chitosan-saccharide derivatives, as well as O-succinyl-chitosan have been conducted to make water soluble derivatives of chitosan. More methods such as alkylation, acetylation, carboxymethylation chitosan and quaternization have been attempted as well.[6-8]

Researchers studied if nitric acid could dissolve chitosan only to discover that a white gelatinous precipitate would instead form. They also tried sulphuric acid which did not dissolve the chitosan and instead formed chitosan sulphate, a white crystalline solid. It was determined that the solubility of chitosan very heavily depends on the pKa values of these acids and their concentrations.[4]

In one study, quaternary ammonium chitosan was prepared and tested for its antimicrobial activity. The quaternized chitosan derivatives in fact exhibited stronger antibacterial activity than just chitosan.[4] However, another study reported otherwise, claiming that the quaternized chitosan failed to exemplify antibacterial activity against S. aureus, an antibiotic resistant infection that causes over 11,000 deaths annually in the United States alone.[6]

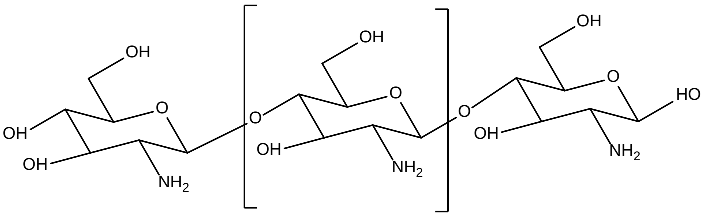

Figure 1: Structure of Chitosan

The partial hydrolization of chitosan by enzymatic processes has also been studied in order to enhance the solubility of chitosan. This process decreases the molecular weight of chitosan, shortens the chain lengths, and results in free amine groups. This makes the chitosan readily soluble in water. The greater solubility and low viscosity of the partial hydrolyzed chitosan has drawn many researchers to use chitosan in its lower molecular weight form.[4,7]

The antimicrobial mechanism of chitosan is still not completely understood, and the search continues to find better ways of processing chitosan to acquire the desired properties. The characteristics of chitosan are influenced by molecular weight, as well as the degree of acetylation. These factors impact the solubility of the chitosan, which in turn determines the rheological and physical properties.[9] In several papers, researchers have reported that they improved the solubility of the chitosan by reducing the degree of deacetylation. However, the reacetylation of chitosan reverts the polymer back to chitin. The question then arises as to why chitin is not used directly instead since theoretically it should exhibit higher antimicrobial activity.

The $-NH_2$ groups in the chitosan molecule, as shown in Figure 1, are highly reactive. Therefore processes to increase the free amine groups will directly correlate with a higher antimicrobial effect.[4] The more deacetylated the molecule is, the higher the antimicrobial impact. Since reducing the degree of acetylation increases the antimicrobial activity, using chitin would not result in equivalent antimicrobial results in comparison to using the deacetylated chitosan in the development of these antimicrobial hydrogels.

The distribution of the acetyl groups as well as the free amino groups make chitosan a very unique polymer as it impacts the bonding behavior. It also makes chitosan soluble in solutions below pH of 6.5. The amino groups make chitosan a cationic polyelectrolyte, unlike other polysaccharides.[10] Chitosan is protonated in aqueous acidic solutions and, when dissolved, takes on high positive charges on NH_3^+ groups.[4] The resultant polysaccharide is positively charged making it attracted to negatively charged surfaces. The solubility of chitosan in acidic solutions as well as its aggregation with polyanions contribute to chitosan having excellent properties for gel-forming.[4]

The increasing prevalence of antibiotic resistant infections, especially those stemming from impaired wound healing as well as biomedical implant failure, has led to the development of materials with antimicrobial activity such as hydrogels. Hydrogels are biocompatible and can be incredibly useful in drug delivery, wound healing, and several other biomedical applications. Chitosan-based hydrogels are extremely sought after materials for use as wound dressings since the wound area is aided by the hydrated environment the hydrogel offers while simultaneously imparting antimicrobial activity.[11] Additionally, hydrogels can also incorporate a controlled release system to deliver drugs.

Over the years, researchers have been attempting to perfect the process of creating hydrogels using chitosan. Scientists at the University of Otago attempted to make antimicrobial chitosan dextran-based hydrogels. However, they determined that the antimicrobial activity was to be credited to the dextran aldehyde instead of the chitosan because their processing of the hydrogel led to the chitosan losing its polycationic nature.[8] Others have immobilized the chitosan, encapsulating it into a gel to prepare a wound dressing using glutaraldehyde as the cross-linker. The authors in that study showed that the chitosan hydrogel layer did lower the microbial activity.[8]

Antimicrobial hydrogels have also been developed as coatings for medical implants. Scientists developed an antimicrobial hydrogel based quaternized chitosan-graft-PEG methacrylate. Several samples were created with different variability in each from degree of acetylation to degree of quaternization.[6] Of the hydrogels that were tested, the dimethyldecylammonium chitosan (highly quaternized)-graft-PEG methacrylate gel showed the most antimicrobial activity. The researchers proposed that the polycationic hydrogel is contact active, working as a sponge and attracting the anionic microbial membranes into the hydrogel nanopores. The cationic amino groups of the chitosan bind with the anionic groups of the microorganisms and fungi, resulting in the inhibition of the bacterial growth.[7]

Over the last couple decades, chitosan has grabbed researchers' attentions due to its potential as an antimicrobial agent. While a significant amount of progress has been done in the characterizing of chitosan, there are many areas that require further research. Various results reported by researchers under similar or even identical conditions tell different and even completely opposing stories.[7] Testing methods have not been standardized, thereby making it difficult to compare different studies. Furthermore, the development of a process for increasing chitosan's solubility that does not diminish its antimicrobial properties is a priority. This discovery alone can open a whole world of applications for chitosan in, the biomedical field and beyond. Future work in this field can provide clarity to the underlying mechanisms furthering our understanding of chitosan and its behavior and characteristics. The development of materials that are active against these infectious microorganisms is proving essential, particularly in biomedical implants as well as wound healing. Chitosan is a game changing polymer with its anti-inflammatory, antifungal, and antimicrobial properties as well as its biocompatibility, biodegradability, and ability to bypass mammalian cells and specifically attack foreign microbes.[7] Additionally, chitosan-based antimicrobial hydrogels are ideal for injectable, topical, and coating applications among others.[9] Needless to say, the focus on chitosan will continue to proliferate, especially as antibiotic resistant infections are on the rise.

References

1. Antimicrobial Resistance: Global Report on Surveillance; World Health Organization: Geneva, 2014.

2. O'Neill, J. Antimicrobial Resistance: Tackling a crisis for the health and wealth of nations; Government of the U.K. and Wellcome Trust, 2014.

3. Centers for Disease Control and Prevention. Antibiotic Resistance Threats in the United States. U.S. Department of Health and Human Services, 2013.

4. Goy, R. C.; de Britto, D.; Assis, O.B.G. Polimeros: Ciencia e Tecnologia **2009**, 19, 241-247.

5. Rouget, C. Comptes Rendus Hebdomadeires des Seances de l'Academie des Sciences **185**9 48, 729-795.

6. Tan, H.; Ma, R.; Lin, C.; Liu, Z.; Tang, T. International Journal of Molecular Sciences **2013**, 14, 1854-1859.

7. Kong, M.; Guang Chen, X.; Xing, K.; Jin Park, H. International Journal of Food Microbiology **2010**, 144, 51-63.

8. Aziz, M.A.; Cabral, J.D; Brooks, H.J.L; Moratti, S.C; Hanton, L.R. American Society of Microbiology **2012**, 280-287.

9. Salome Veiga, A.; Schneider, J.P. Biopolymers **2013**, 637-644.

10. Chen, Y.L. Preparation and Characterization of Water-Soluble Chitosan Gel for Skin Hydration. Universiti Sains Malaysia, 2008.

11. Li, Y.; Fukushima, K.; Coady, D.; Englier, A. Angewandte Chemie International Edition in English **2013**, 52, 647-648.

Priya Venkatraman, Materials Science and Engineering, Virginia Tech

Strength and Microscopy Analysis of Surface-modified Soda-lime-silicate Glass Rods

Amy Bumbaco, Jacob Young, and Michael Zachar

Virginia Tech, Department of Materials Science and Engineering, College of Engineering, 213 Holden Hall, Virginia Tech, Blacksburg, VA 24060

Abstract

Glass has high theoretical strength; however, microcracks on the surface of the glass greatly decrease the strength. Various methods to alleviate the effects of these cracks have been devised, including ion-exchange, mechanical abrasion, and acid etching. The goal of this experiment was to compare these methods by quantifying the strength via three-point bend testing to determine the modulus of rupture. Optical microscopy confirmed results, including the data that indicated that ion-exchange had the largest effect on strength by either widening or forcing shut cracks. Acid etching produced a moderate improvement in modulus of rupture by smoothing cracks. Finally, mechanical abrasion decreased strength but provided a more uniform strength distribution.

Keywords: soda-lime-silicate glass, glass microscopy, three-point bend testing, modulus of rupture

1. Introduction

Soda-lime-silicate glass is one of the most commonly used glasses due to ease of production and high theoretical strength. Covalent bonding prevalent in glasses results in theoretical strength on the order of 7 GPa. However, glasses actually fall far short of this theoretical strength, failing at around 100 MPa.[1]

This large discrepancy in theoretical strength versus actual strength is believed to be the result of microcracks across the surface of the glass. Cracks act as stress multipliers, and the high number of cracks present on the surface of glasses result in the large reduction in strength observed. Additionally, these cracks are randomly distributed over the surface of the glass, making the actual failure stress varied and unpredictable. Various methods have been developed to compensate for these effects.[1] This experiment compares these treatment methods.

1.1 Ion-exchange

The presence of cracks in a material causes a reduction of strength, and ultimately brittle failure, when the material is loaded in tensile fashion. A common method for increasing the strength of a material prone to cracking is to introduce residual compressive stresses.[2] Soda-lime-silicate glass contains between 12 and 16% by weight sodium oxide. At elevated temperatures, ion-exchange can occur where sodium ions diffuse out of the glass to be replaced by ions from a reactive material. One common method of ion-exchange is putting soda-lime-silicate glass in a bath of potassium nitrate. This causes ion-exchange between the sodium ions in the glass and the potassium ions in the bath. The larger potassium ions introduce residual compressive stresses on the surface of the glass, and this residual stress compensates for the presence of microcracks.[2]

1.2 Acid Etching

The effect a crack has on a material is directly related to the size of the crack. Longer crack lengths result in lowering of the stress required for fracture. Additionally, the shape of the crack affects the reduction of strength. A sharp pointed crack is much more of a stress riser than a blunt crack tip.[3]

Acid etching is used to help compensate for these crack properties. By etching away the surface layer of a glass, the length of the microcracks on the surface is reduced. Additionally, the use of acid etching has been shown to help reduce the sharpness of the crack tips. This process, in turn, reduces the stress riser effect of these microcracks and increases the strength of the glass.[3]

1.3 Mechanical Strengthening

As previously noted, microcracks formed across the surface of the glass result in a large decrease in the actual strength. These cracks are randomly distributed on the surface of the glass, with widely varying concentrations and crack lengths. As a result, two pieces of glass that were prepared using the exact same methods can have a large variation in strength.

In order to account for this large deviation in properties, some glasses go through a mechanical surface modification process where the glass is rolled in an abrasive substance, such as alumina. This process, while increasing the prevalence of microcracks on the surface of a glass and decreasing the overall strength of the glass, does result in a more uniform composition of microcracks and limits the variability of the strength, ultimately making it easier to predict at what stress the glass will fail.[4]

1.4 Three-point Bend Testing

Surface flaws in glass cause brittle failure of the parts when under tension. These microcracks have no effect on the glass in compression, since compression forces the cracks closed and allow the glass to behave as though they were not present. Thus, it is most advantageous to test the glass for failure in tension.[5]

However, testing brittle materials in tension via traditional means of pulling in two vice grips often leads to failure at the grips. An alternative method of testing is used where a sample is placed on two supports, with an unsupported span in between. At the halfway point of this span, a force is applied until fracture. From this test, the stress at failure, also known as the modulus of rupture (MOR) in bending, can be determined according to Equation 1:

$$\sigma_{fb} = \frac{PL}{\pi r^3} \tag{1}$$

where P is the load at failure, L is the length of the span between supports, and r is the radius of the test specimen.[5] A sample in the testing set up is shown in Figure 1.

Three-point bend test creates a linear variation of bending moment with the maximum at the center load, shown with Equation 1, while the four-point bend test allows the specimen to fail at its weakest point. The four-point bend test was originally chosen for this project, but due to the size of the rods as well as equipment available to us, the three-point bend test was decided to be the more feasible option. This affects the data by showing failure at the center of the rods and not the overall failure of the rods.

1.5 Surface Analysis

To qualitatively determine how the variation of crack size compared to the control sample, optical microscopy was used to observe the surface of the glass. The shape and size of cracks can be told from micrographs of a thin lengthwise section of the rod. Thus, the effects of a treatment can be compared to the control by visual inspection, which will reinforce the results of the three-point bend testing.

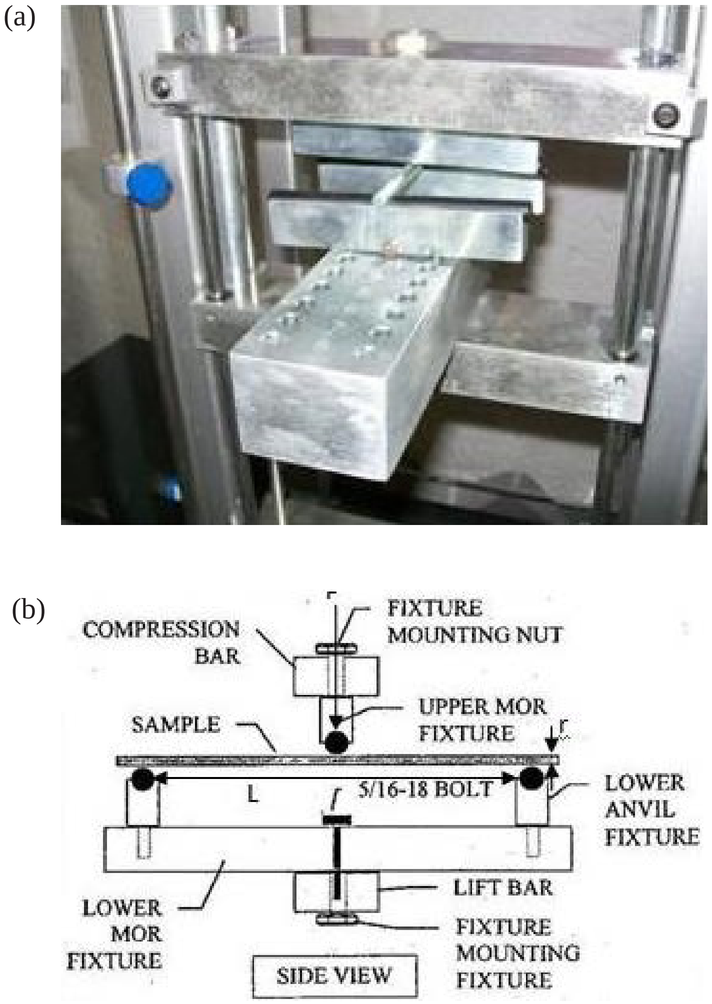

Figure 1: (a) Three-point bend testing set up with sample in supports; (b) diagram of applied loads during testing. [6]

2. Procedure

The rod surfaces were altered using three different techniques: mechanical surface modification, molten salt baths, and acid baths. The acid baths and mechanical surface modification were performed for two different lengths of time. Two different compositions of molten salt baths were used for one fixed time. A flowchart of all experimental processing and testing is seen in Figure 2.

2.1 Rod Preparation

A low-speed diamond blade saw was used to cut 25 cylindrical glass rods in half. The rods were received from Fisher Scientific and were approximately 150 millimeters long with an approximate 5 millimeter diameter. Cooling fluid/oil was used to decrease the cutting temperature due to friction.

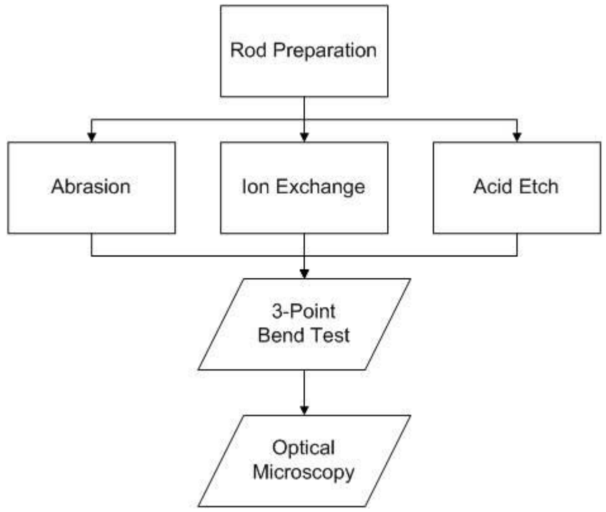

Figure 2: Flowchart of experimental processing and testing

After the cutting was completed, the rods were cleaned using soap and water to remove oil residue that could have skewed experimental results.

2.2 Mechanical Surface Modification

Alumina was measured to completely cover 6 glass rods for 3- and 24-hour mechanical surface modification tests. Approximately 212 grams were used for each test to fully cover the samples. Glass rods and alumina were placed in a screw cap plastic bottle taped on the outside to ensure enough friction against the rollers. The bottles were placed on a US Stoneware Roller at a moderate rate of rotation along with a weight for optimal rolling.

2.3 Nitric Acid Surface Modification

Two sets of rods were completely submerged in full strength (15.6 M) nitric acid (HNO_3) at room temperature for time lengths of 1 and 2 hours, respectively. Rods were washed off with water once withdrawn from the bath.

2.4 Molten Salt Surface Modification

Rods were submerged in molten salt baths at 375°C for 24 hours. Two baths were used, one of 250g of lithium nitrate (LiNO3) and one of potassium nitrate (KNO3), with 6 rods per bath. Rods were covered in salt and the entire contents of the bath were slowly warmed in a ThermoLyne furnace until 375°C. Upon removal from the furnace after 24 hours, the glass was taken out of the bath, left to cool on a refractory block, and then rinsed with water to remove excess salt.

2.5 Three-point Bend Testing

A Com-Ten Series 95 VC three-point bend tester was used to determine the MOR as a result of the different treatments. Rods were placed on supports with a 50 mm unsupported span. A force was applied at the midpoint of the span, and the rate of loading was set at five mm/minute. The load was increased until fracture, at which point the force and MOR were recorded. This test was performed for ten control samples and five samples for each treatment. Following the testing, the mean was calculated for both the force at fracture and the MOR.

2.6 Surface Analysis

A section no more than 2 millimeters lengthwise in thickness was cut off from the inner part of a rod. This operation was performed on each treatment and a control sample. The section was then examined using an Olympus BH2-UMA optical microscope. The amount and shape of surface cracks were noted. Digital images were taken and other observations recorded about the overall appearance of each sample.

3. Results and Discussion

3.1 Surface Analysis

Optical microscopy was used to observe the resultant microcracks stemming from the different glass treatments. For the 3-hour mechanically abraded sample, the cracks appeared similar to the control, but higher in concentration. The highest crack concentration was found in the 24-hour sample, which showed very wide cracks, seen in Figure 3. Greater crack prevalence was a result of the Vickers hardness of alumina being two orders of magnitude higher than that of soda-lime-silicate glass.[7] Therefore, the alumina powder chipped into the glass during rolling and created more cracks. This increase in crack concentration results in a more predictable MOR.

The 1-hour acid-etched sample showed smoother cracks in comparison to the control sample seen in Figure 4 (a). This effect was more pronounced in the 2-hour sample due to the presence of jagged cracks with large surface areas that were easily etched by the nitric acid. The smoother cracks had a lower stress riser effect, allowing the glass to withstand higher stresses before failure.

The ion-exchange samples showed the most profound departure from the control. The lithium nitrate sample showed cracks that were much larger both in length and width

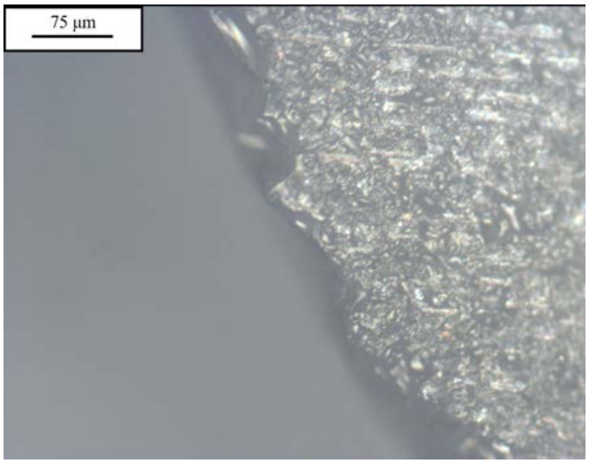

Figure 3: Edge of 24-hour mechanically abraded glass.

(a) (b)

Figure 4: (a) Edge of control, and (b) 2-hour acid-etched glass samples.

Table 1: Results of three-point bend testing.

Group	Force at Fracture (N)	Modulus of Rupture (MPa)	Standard Deviation in MOR
Control Group	104.98	106.93	12.87
Mechanical - 3 Hour	82.74	84.28	5.16
Mechanical - 24 Hour	87.19	88.81	8.23
HNO_3 - 1 Hour	109.43	111.46	17.86
HNO_3 - 2 Hour	126.33	129.40	16.50
$LiNO_3$ Bath	35.72	36.25	2.03
KNO_3 Bath	429.70	437.69	155.96

than the control section, one of which is circled in Figure 5(a). The potassium nitrate showed cracks that had been forced shut, such as the one circled in Figure 5(b). These results were due to an ion-exchange in which the sodium ions in the glass were exchanged with the alkali metal ions in each salt. The smaller lithium ions caused a shrinkage effect in the surface, spreading out the cracks and resulting in a residual tensile stress. The larger potassium ions created an expansion effect in the crystal lattice that closed cracks and introduced a compressive stress.

3.2 Three-point Bend Testing

The experimental values found from completing three-point bend testing for the force at fracture and the calculated MOR are given in Table 1 above. Figure 6 shows the relative differences in the MOR for all the treatments. The top of the blue column for each treatment corresponds to the average MOR. The black bar represents the range of measurements per treatment.

The force at fracture was measured directly from the testing apparatus, and the MOR was calculated using Equation 1.

Mechanical rolling of the glass rods resulted in a decrease in the strength of the glass, due to the increase in surface cracks seen in the micrographs. However, this also resulted in more predictable fracture strengths. The standard deviation in the fracture strengths for the 3-hour samples was lower than the standard deviation for the 24-hour samples, suggesting that the 24-hour samples were rolled for too long.

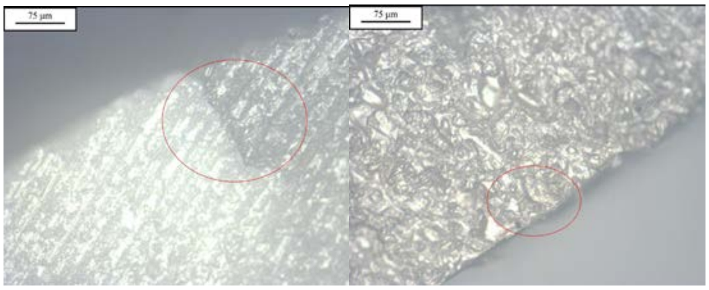

(a) (b)

Figure 5: (a) Edge of glass treated with lithium nitrate molten salt bath; (b) edge of glass treated with potassium nitrate molten salt bath.

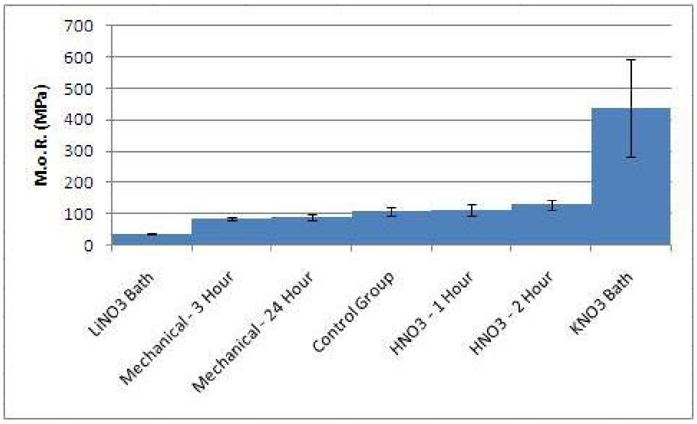

Figure 6: Modulus of rupture averages and ranges for each treatment.

The acid-etched samples both showed increased strength, with the 2-hour acid samples experiencing a larger increase than the 1-hour. This outcome was a result of the smoothing effects of the acid seen in the micrographs, which blunted the crack tips.

Finally, the $LiNO_3$ samples lost a considerable amount of strength, due to the residual tension opening the cracks and increasing significantly the stress riser effects. Conversely, the KNO_3 samples were much stronger than the controls because of the residual compression effects closing the cracks.

4. Conclusions

This experiment attempted to determine the relationship between surface modification of glass with respect to the surface cracks and resultant change in the strength measured by the MOR. The lithium nitrate-treated glass had the lowest MOR and exhibited wide cracks. Glass that was mechanically abraded showed a slight decrease in strength and a lower standard deviation in its MOR, as well as a larger amount of surface cracks. The acid treatments produced a moderate increase in strength with smoother cracks. Finally, rods placed in the potassium nitrate bath displayed a drastic increase in strength, with cracks being forced shut by the expanded lattice. For the strongest glass possible, a potassium nitrate molten salt bath should be used to treat the rods.

Further work is recommended to discover the optimal processing specifications, such as time and temperature, to maximize the increase in MOR. Also, it may be beneficial to attempt to combine the potassium nitrate salt bath with mechanical abrasion in order to create a stronger glass that fails at a more predicable energy.

Acknowledgements

Special thanks to the instructors, Ms. Diane Folz and Ms. Christine Burgoyne, and graduate teaching assistants, Mr. Andrew Ziegler and Ms. Anne Coppa, of MSE 4424 Materials Laboratory II for guidance with our experiment and for obtaining materials. Thanks also to Professor Norman Dowling for aid with the MOR calculations.

References

1. Garza-Méndez, F. J.; Hinojosa-Rivera, M.; Gómez, I.; Sánchez, E. M. Applied Surface Science **2007**, 254(5), 1471-1474.

2. Abrams, M. B.; Green, D. J.; Jill Glass, S. Journal of Non-Crystalline Solids **2003**, 321(1–2), 10-19.

3. Kolli, M.; Hamidouche, M.; Bouaouadja, N.; Fantozzi, G. Journal of the European Ceramic Society **2009**, 29(13), 2697-2704.

4. Nordberg, M. E.; Mochel, E. L.; Garfinkel, H. M.; Olcott, J. S. Journal of the American Ceramic Society **1964**, 47(5), 215-219.

5. Dowling, N. E., Mechanical Behavior of Materials. 3 ed.; Pearson Education: Upper Saddle River, New Jersey, 2007.

6. Industries, C.-T., User's Manual for Series 95 VC. Granta Design Limited: Cambridge, UK, 2009.

Authors

Amy Bumbaco

Contact at: simsgirl89@gmail.com

Jacob Young graduated from Virginia Tech in 2011 with a Bachelor's of Science in Materials Science and Engineering. After graduation, his interest in metallurgy and casting led him to employment as a Foundry Engineer and Quality Assurance Supervisor at Conbraco Industries in Pageland, South Carolina until 2014. Jacob is currently pursuing his Master's Degree in Metallurgy at the University of Alabama in Tuscaloosa, Alabama as a Graduate Research Assistant under Dr. Ramana Reddy. His current research interest is the synthesis and characterization of novel thermoelectric alloys.

Domain Wall Collision-Induced Spin Waves

Tristan Delaney

Massachusetts Institute of Technology, Department of Materials Science and Engineering, 77 Massachusetts Ave, Cambridge, MA 02139

Abstract

A series of micromagnetic simulations are conducted whereby two transverse domain walls are injected into a straight magnetic nanowire under an applied field. It is found that, based on the relative orientation of the domain walls, the two may annihilate, resulting in the generation of an intense spin-wave burst. Since the applied magnetic fields for these simulations are smaller than the Walker breakdown field, these results present an extremely low-energy means of generating and controlling spin waves for engineering applications.

Keywords: spin waves, Landau-Lifschitz-Glibert Equation, magnetic domain walls, magnonics

1. Introduction

1.1 Spin Wave Fundamentals

The temporal evolution of the magnetization vector M(r) in a material is given by the Landau-Lifschitz-Gilbert (LLG) Equation,

$$\frac{d\hat{m}}{dt} = -\gamma\left(\hat{m} \times \vec{H}\right) + \alpha\left(\hat{m} \times \frac{d\hat{m}}{dt}\right) \quad (1)$$

where α is the phenomenological damping constant, γ is the gyromagnetic ratio, $\boldsymbol{m}$ is the unit magnetization vector, and $\boldsymbol{H}$ is the effective field comprised of the exchange, dipolar, anisotropic, and external applied fields acting upon M. In this paper, only the exchange, dipolar, and external fields and their associated energies are taken into account to accurately model permalloy, a soft magnetic material. The exchange field arises from nonzero gradients in the magnetic configuration of lattice moments in the crystal structure of a magnetic material. The dipolar field, also known as the demagnetizing field, arises when "free poles" – magnetic moments which orient themselves orthogonal to a surface – emit stray fields outside of the material itself; the dipolar field usually forces magnetic moments in magnetic media to orient themselves such that stray fields are kept inside the media itself, often at the expense of exchange or anisotropic energies. The experimental value of α is usually measured to be of order 0.01 for soft magnetic materials. The LLG Equation describes the nature of the precession of each lattice moment as it aligns with the sum of all effective magnetic fields presently acting on them. Spin waves (SWs) are collective excitations of these lattice moments that propagate through a magnetic medium, leading to the redistribution of energy introduced into a ferromagnetic system due to external excitation (e.g. an external Oersted field) or internal changes of the topological spin texture within a ferromagnetic structure. SWs were first observed as resonant microwave modes of the magnetization in ferrite samples[1] The nature of these modes was later derived analytically by Walker[2] for spheroids and Damon and Eschbach[3] for ferromagnetic slabs, in the long-wavelength limit of strictly dipolar modes by simultaneously solving Equation 1 together with Maxwell's Equations. In both works, only dipole-dipole interactions are taken into account as this allows one to analytically derive the nature of the resonant modes; thus the modes have a long-wavelength, low frequency character which makes them only applicable on the scale of several millimeters. Thus, many of the applications for these resonant modes in ferrite have been in the areas of measurement and material characterization,[11] antennae,[12] and other applications where a characteristic length of more than a few micrometers is desired.

Recently, interest in spin waves has shifted to higher frequency, shorter wavelength modes that are on the scale of several nanometers. These SWs arise from exchange-dipole and purely exchange modes in high-moment metallic ferromagnets with frequencies of tens to hundreds of GHz depending on the geometry and material parameters of the medium through which they propagate. The short wavelengths of exchange and dipole-exchange SWs make it necessary to take into consideration the effects of all possible fields acting upon the magnetic moments in a nanostructure, making an analytic result of the general dispersion relation unfeasible without the help of numerical simulations.[6] Due to their large group velocities, these SW modes have potential applications in ultra low power information processing and logic devices[4] based on nanoscale geometrical structures such as nanowire conduits, in which the spin wave modes and propagation characteristics can be precisely engineered. The emerging subfield of "magnonics"[23] seeks to understand and control SW excitations in nanoscale magnetic devices, and is focused on such issues as SW band structure and band-gap engineering,[5,13] predictably and controllably generating SW excitations,[13] and understanding the effects of phase shift of SWs as they propagate through domain walls and other nonuniform magnetic textures.[4,15,16]

A challenge for future applications of high frequency SWs in magnonic devices is overcoming the relatively short attenuation length due to the exponential decay in the amplitude of the SWs as they propagate, imposed by the damping term in Eq. 1. Two general approaches have been proposed to compensate for the effect of attenuation: first, to lower the effective damping through materials engineering or using other interactions such as spin-transfer torques induced by spin-polarized current; or, second, to enhance the efficiency of generating large-amplitude SW excitations such that they can be detected at long distances even with the effects of attenuation. The former is quite difficult to accomplish experimentally due to the intrinsic nature of damping and our rather poor microscopic understanding of the phenomenological damping and term, and the effects of spin-transfer in real materials.[16] The latter approach is experimentally fairly simple in principle, but difficult in practice. The conventional means of high-power excitation of SWs is through the application of a large external Oersted field. This in turn requires a large current to generate the required field, which can be very power demanding and often inefficient. This paper explores the possibility of releasing the energy stored in magnetic domain walls through controlled DW collision and annihilation as a means of generating large amplitude SWs on demand using very low power consumption.

1.2 Domain Wall Structure and Topology

Magnetic domain walls (DWs) are local regions where the magnetization undergoes an abrupt change in direction.[17] In order to understand the mechanisms of DW interactions and annihilation, a thorough analysis of the physical structure and topological properties of DWs must be presented. In macroscopic magnetic materials, DWs serve to lower the magnetic energy of the sample as a whole by minimizing stray fields due to free poles at the surface, which require a large amount of energy to maintain. However, DWs themselves cost energy (due to the exchange interaction that prefers uniformly-oriented magnetization). In smaller structures, especially for structures whose dimensions are less than one micron, DWs become energetically unfavorable and serve only as a transition area between two or more domains of differing magnetization. The internal structure of a DW is highly dependent upon the parameters of the material present and upon the size of the sample. This paper is concerned with quasi-one-dimensional magnetic nanowires of rectangular cross-section: high aspect ratio nanostripes of width w, thickness t, and length L, with L>>w>>t. In such structures, the simplest 180° DW in a rectangular nanowire typically comes in two variations: a transverse wall (TW), where the internal magnetization of the wall is orthogonal to the magnetization on either side and directed along the width of the nanowire (assuming that the width is considerably larger than the thickness); and a vortex wall (VW), where the internal magnetization of the wall rotates around a single moment known as the vortex core (which is directed orthogonal to the plane of rotation).

The topological properties of these two types are quite different. As much of the internal magnetization of a TW is directed to a hard-axis imposed by the narrow width of the wire, the internal energy due to the demagnetizing field is large compared to that of a VW. On the other hand, the rotation of the internal magnetization of a VW greatly increases its internal exchange energy when compared to that of a TW. These differences in internal energy also affect the dynamics of each wall, which have been studied for quite some time. Especially peculiar is the effect of applied field magnitude on TW motion as small fields (often below 15-25 Oe, depending on the dimensions of the wire) will quickly drive a TW into motion up to the critical Walker breakdown field after which the TW undergoes a slower oscillatory motion, mediated by the periodic nucleation and motion of a vortex core across the domain wall.[18,19]

More important for the purposes of this paper is the presence of a topological "charge" within the DWs, which determines several characteristics including DW pinning, injection, and packing.[8,10,20] Figure 1 details the magnetic configurations of these topological defects along with their winding numbers associated with each defect and the position of each defect for both a transverse and vortex DW. For DWs, the winding numbers of all defects contained within the wall sum to zero; this indicates that each wall is a stable structure, but that energy is stored primarily in each defect which makes up the wall. Like protons and electrons, the interaction between two topological defects is determined by their winding numbers – that is, defects of opposite sign annihilate one another while those of the same sign will preserve their overall structure.[8]

2. Procedure

The simulations are run using the Object-Oriented Micromagnetics Framework (OOMMF), a finite differences micromagnetics package developed at NIST. The overall geometry of the structure is of a 1000x40x10 nm^3 nanowire, initially magnetized in the +x-direction, placed between two 200x200x10 nm^3 nucleation pads each with a vortex core. A cell size of 2.5x2.5x10 nm^3 was used in the simulations with the material parameters resembling those of permalloy (M_s = 8.0x10^5 A/m, A = 1.3x10^{-11} J/m^3). The TWs were

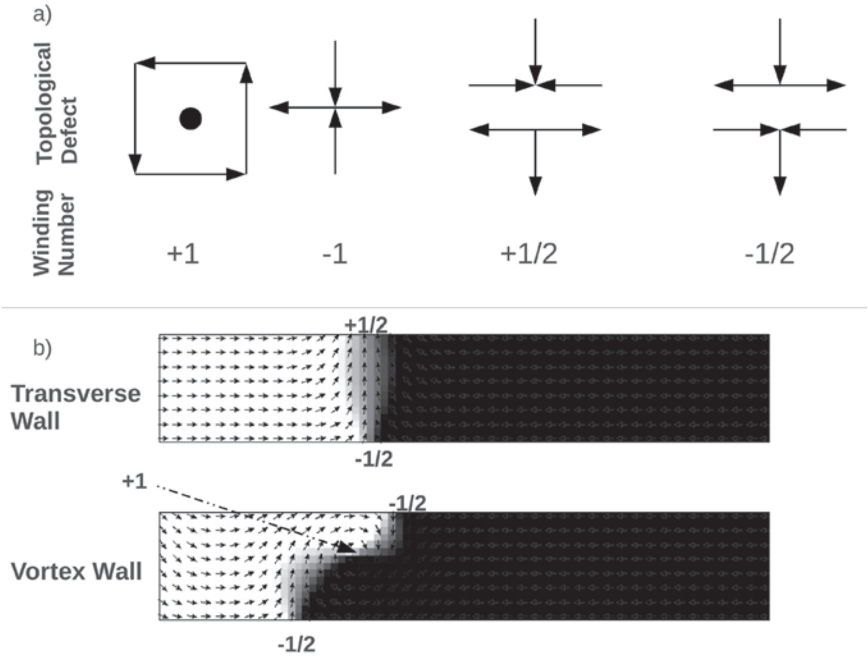

Figure 1: a) Internal and edge defects with associated integer and half-integer winding number b) An example of a transverse wall and a vortex wall. In both cases, the net winding number of the wall is n = 0.

nucleated by applying a 200 Oe field in the –x-direction for approximately 1 nanosecond, after which the applied field was dropped values ranging between 1 and 25 Oe and applied to the system for another 4 nanoseconds. The vorticity of each nucleation pad determines the direction of the internal magnetizations of the injected TWs, and initial configurations of both similar and opposite vorticity are used.

3. Results & Discussion

Controlling the internal magnetization of a TW is found to be very simple as the internal magnetization is determined by the magnetization of the part of the vortex adjacent to the beginning of the nanowire. Thus, nucleation pads of the same vorticity nucleate TWs of opposite internal magnetization while pads of opposite vorticity nucleate TWs of the same internal magnetization. Thus, SWs can only be generated if the nucleation pads are of opposite vorticity (Figure 2).

Another set of simulations was run to compare the amplitude of SWs generated using a powerful Oersted field. Using the same geometry and material parameters, but not nucleating any DWs into the nanowire beforehand, an Oersted field was applied to a row of cells in the center of the wire in the z axis in the form of a sine cardinal function,

$$H_Z = H_{MAX}\frac{\sin(2\pi\nu t)}{2\pi\nu t} \quad (2)$$

where ν = 100 GHz and H_{MAX} ranged between 100 Oe and 10 kOe. The sine cardinal function serves to equally excite all modes of SWs up to 100 GHz and its dispersion relation gives all possible modes allowed in the geometry. The dispersion relations were determined by calculating the Discrete Fourier Transform of the z-component (out of plane) magnetization for a 400 nm line of cells within the middle of the nanowire for 2 nanoseconds after the external Oersted field was applied, and are plotted on a logarithmic scale since the Fast Fourier Transform (FFT) power of all possible modes scales several orders of magnitude. The parabolic relation between frequency (*f*) and wave vector (*k*) is characteristic of the generally dispersive nature of SWs; thus SWs of higher frequency propagate at higher velocities than those of lower frequency. The dispersion relations for H_{MAX} = 100 Oe and H_{MAX} = 10 kOe, shown in Fig 3(a-b), show that all of the modes up to 50 GHz are equally excited, and that the FFT power of these modes rises in proportion to the value of H_{MAX}.

In contrast with those generated by the external Oersted Field, the SWs generated via TW annihilation using a 1 Oe and 25 Oe field, Fig 3(c-d), show very little differences in the FFT powers of the SW modes generated. The data show that the TW annihilation scheme produces SWs ranging between 12 and 50 GHz in a nearly uniform population of allowed modes, all of extremely large amplitude. The uniformity of the SWs generated, regardless of the magnitude of the driving field, shows that these modes generated are directly related to the energy stored in the magnetic configurations of the TWs themselves. This result has great implications on the efficiency of TW annihilation as a means of generating SWs, compared to the conventional externally applied field

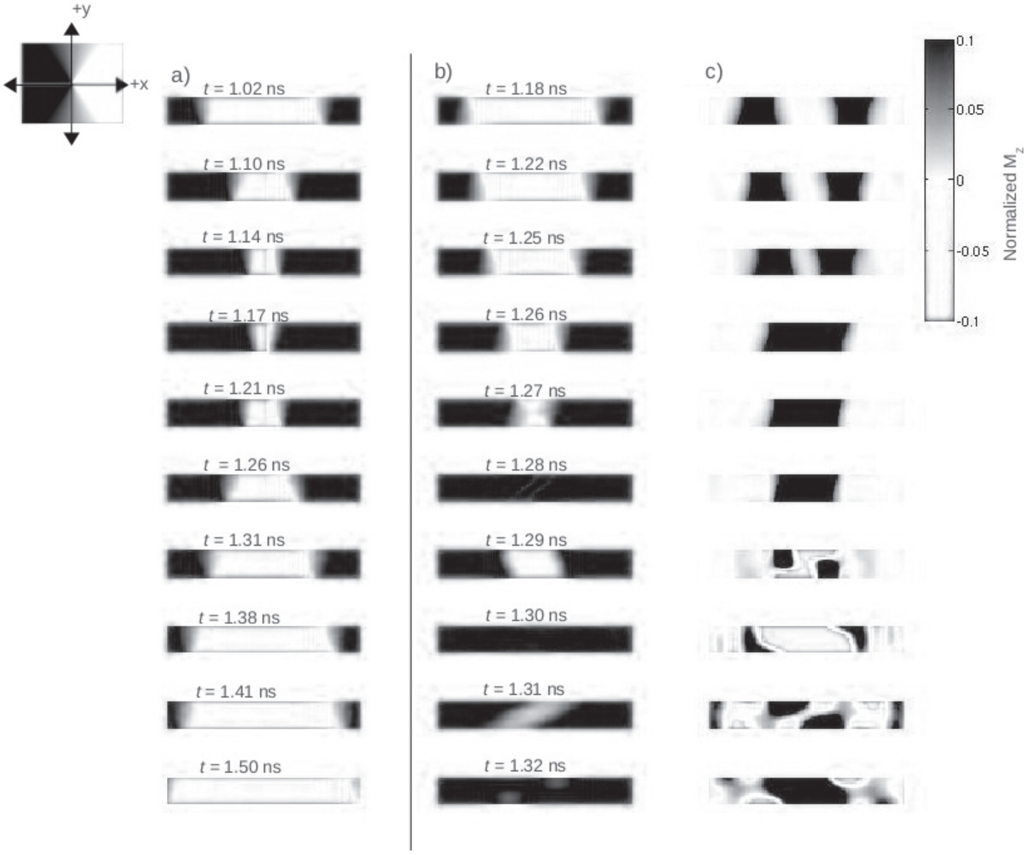

Figure 2: Side by side comparison of the collision between TWs of various internal magnetizations: a) opposite (-y/+y) and b) similar (+y/+y). c) When two walls are of the same internal magnetization, their topological defects of opposite winding number annihilate generating large amplitude SWs.

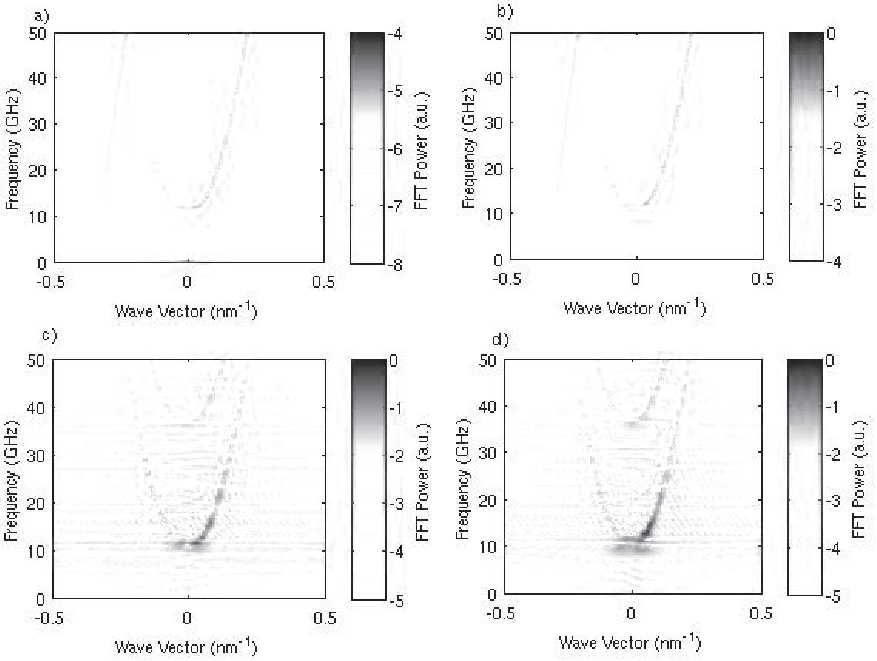

Figure 3: Dispersion relations for sine cardinal Oersted fields with H_{MAX} = 100 Oe (a) and H_{MAX} = 10 kOe (b) as well as TW collision induced SWs at driving fields of H_d = 1 Oe (c) and H_d = 25 Oe (d).

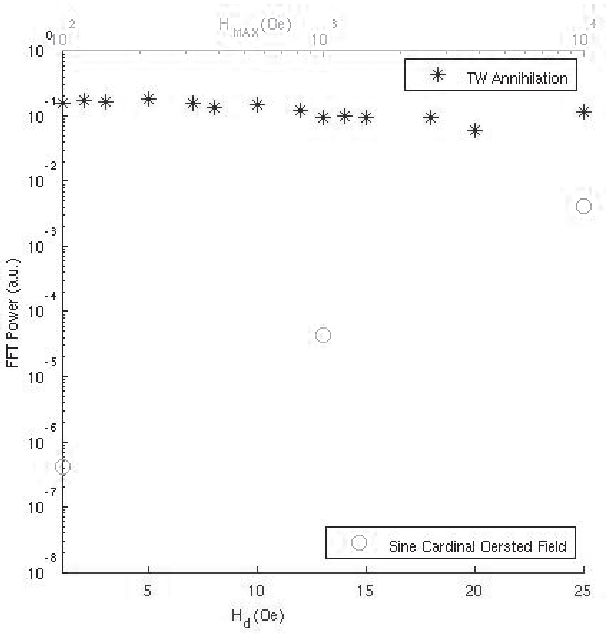

Figure 4: Comparison of FFT Power of the two methods.

as most TWs only require minimal field to actually drive their motion.

The extreme advantage of this method, however, lies in the amplitude of the SWs generated for extremely low power input. Figure 4 compares the FFT power of the SW packet with $k = 0.1133$ nm^{-1} and $f = 21$ GHz for both TW annihilation-induced SWs and the Oersted fields. As was stated before, SWs generated via TW annihilation are largely the same in amplitude regardless of the strength of the applied field; however, this is not true for the Oersted fields which require an extremely large applied field in order to excite large amplitude SWs. Yet even with the large field, the SWs generated by the Oersted fields pale in comparison to the ones generated by the annihilation of the TWs (Figure 4).

The key to generating large amplitude, high frequency SW pulse lies in the efficiency with which energy can be stored within the magnetic moments and transmitted through SWs. For the method proposed in this paper, the energy in the system is stored in the exchange and dipolar energy in a nucleated TW. These energy components are released upon annihilation at the collision site of the two TWs, which serves as a high energy oscillatory region which continuously generates SWs until it has relaxed to an equilibrium state. However, for the applied Oersted field, energy is introduced into the system solely through the Zeeman interaction of the applied field with the moments subjected to the field. The maximum Oerstead field that could be experimentally generated is of order 10 kOe using a microelectromagnet, and only hundreds of Oe using the fringing fields from current-carrying excitation wires. By contrast, the effective exchange fields within a DW are of order 10^3-10^4 kOe, and is independent of the driving field that propels the domain walls together. This effect is also supported by the SWs generated by TW annihilation whose overall nature is not affected by the magnitude of the driving field.

The means of inserting energy into the system for both methods contrast heavily in terms of efficiency. The applied Oersted field requires an extremely large amount of power to simply generate a magnetic field large enough to generate SWs, but in the experimental setting, this would require large amounts of current to generate this field only to produce extremely small SWs. However, for the nucleation of two TWs, the field required can be lowered to as low as 20 Oe, based on changes to geometry of the nanostructure into which the walls are injected. After the TW is generated, the only external field necessary is one strong enough to drive a TW across a wire, which requires a field of less than 1 Oe for soft magnetic materials such as permalloy. The results show that higher fields only serve to minimize the time of TW annihilation so long as the field is below the Walker breakdown field of the wire.

4. Conclusion

This paper presents an efficient and generally simple means of generating SWs by controlling the orientation of two TWs so that they will annihilate upon contact. Using the large densities of exchange and dipolar energies stored in the wall, the method proposed generates large amplitude SWs which remain of reasonable size even in the presence of attenuation over large distances. Due to the fact that the SWs generated are characteristic of the internal energy structure of a TW, their amplitude and dispersion relation are uniform regardless of the external field applied – thus a small field-driven collision generates the same SWs as does a field near the Walker breakdown threshold of the TW. Once again, the size of the external field necessary to generate SWs using TW annihilation makes this method much more power efficient than the conventional means of generating SWs in the lab, which requires a large Oersted field which, in turn, requires a large current. The amplitude of the SWs generated via TW annihilation is also much larger than those generated by an external field, and this could allow for the easier study of nonlinear behavior of SWs which cannot normally be done without extremely high applied fields. The crucial element of this method lies in the control of the orientation of the TW, as only TWs of the same internal magnetization will actually annihilate and create SWs, but several means of controlling TW orientation have been suggested and confirmed by simulation. Overall, this method provides a promising solution which takes advantage of the selective nature of TW topology and uses this energetically unfavorable structure as a means of reliably generating large amplitude SWs which can then be used for study or application.

Acknowledgements

Funding support through the MIT Undergraduate Research Opportunities Program (UROP) is gratefully acknowledged. The author would like to thank Professor Geoffrey Beach for his support and contributions to this paper.

References

1. White, L.R.; Solt, I.H. Physical Review Letters **1956**, 104, 56-62.

2. Walker, L. R. Physical Review Letters **1957**, 105, 390-399.

3. Damon, R. W.; Eshbach, J. R. Journal of Physics and Chemistry of Solids **1961**, 19, 308-320.

4. Hertel, Ricardo; Wulfhekel, Wulf; Kirschner, Jürgen. Physical Review Letters **2004**, 93, 257202

5. Lee, K.; Han, D.; Kim, S. Physical Review Letters **2009**, 102, 127202.

6. Soohoo, R.F. Physical Review Letters **1960**, 120, 1978-1982

7. Atkinson, D.; Eastwood, D.S.; Bogart, L. K. Applied Physics Letters **2008**, 92, 022510

8. Kunz, A. Applied Physics Letters **2009**, 94, 13502

9. Lee J.; Lee, K; Choi, S.; Guslienko, K.; Kim, S. Physical Review B **2007**, 76, 184408.

10. Kunz, A.; Reiff, S. Applied Physics Letters **2009**, 94, 192504.

11. Chen, L.; Ong, C.K.; Neo, C.P.; Varadan, V.V; Varadan, V.K. Microwave electronics: measurement and materials characterization; John Wiley & Sons: West Sussex, 2000.

12. Lee, S.; Kim, Y.; Lee, J.; Kim, S.; Krylov, S. K. Samsung Electronics Co., Ltd. Active Magnetic Antenna with Ferrite Core. U.S. Patent 20090289860, November 26, 2009.

13. Barman, A. Journal of Applied Physics D: Applied. Physics **2010**, 43, 195002.

14. Choi, S.; Lee, K.; Yu, K.; Guslienko; Kim, S. Physical Review Letters **2007**, 98, 087205.

15. Choi, S.; Lee, K.; Kim, S. Applied Physics Letters **2006**, 89, 062501.

16. Seo, S.; Lee, K.; Yang, H.; Ono, T. Physical Review Letters **2009**, 102, 147202.

17. Zhang, S.; Li, Z. Physical Review Letters **2004**, 93, 127204.

18. O'Handley, R. Modern Magnetic Materials; John Wiley & Sons: New York, 2000.

19. Beach, G.; Nistor, C.; Knutson, C.; Tsoi, M.; Erskine, L. Nature Materials. **2005**, 4, 741-744.

20. Porter, D.; Donahue, M. Journal of Applied Phyics **2004**, 95, 6729-6731.

21. Atkinson, D.; Eastwood, D.; Bogart, L. Applied Physics Letters **2008**, 92, 022510.

22. Tretiakov, O.; Tchernyschyov, O. Physical Review B **2007**, 75, 012408.

23. Kruglyak, V. V.; Demokritov, S. O.; Grundler, D. Magnonics. Journal of Applied Physics D: Applied. Phyics **2010**, 43, 264001.

About the Author

Tristan Delaney graduated with a Sc. B. in Mathematics from MIT in 2011 and continued onto a PhD in Computational Applied Mathematics at Stony Brook University in New York. His research focus is on mesh generation, computational geometry and finite element analysis. Contact at: tdelaney@ams.stonybrooke.edu.

Magnesium-PMMA Composites Formed by Mechanical Alloying

Matthew A. Hiser

Virginia Polytechnic Institute and State University, Department of Materials Science and Engineering,
212 Holden Hall, Blacksburg, VA 24061

Abstract

The mechanical alloying process is used to form poly methyl methacrylate (PMMA)-5 vol.% magnesium (Mg) composites by high-energy ball milling the blends for up to 10 hours. The milling products and their compacted composites are characterized and compared with milled pure PMMA. Mechanical alloying can cause degradation of the amorphous thermoplastic polymer in the powder mixture but also allows for increasingly fine dispersion of Mg in the PMMA matrix with milling. X-ray diffraction (XRD) and image analysis of optical micrographs show that the magnesium remains crystalline, and its particle size reduces with milling time from an average of 200 microns to under 10 microns after 10 hours milling. Additionally, peak broadening from XRD analysis shows decreasing crystallite size within the particles. The hardness of the composite increases with milling time by up to 7%, whereas the hardness of the milled pure PMMA decreases with milling time by about 5%.

Keywords: mechanical alloying, metal-polymer composite, particle size

1. Introduction

The combination of metals and polymers to form a composite material can be used to expand the range of achievable properties over that of each class of materials individually.[1] In particular, the addition of metallic particles to a polymeric matrix can increase density and electrical and thermal conductivity.[2] Significant research has been performed into the effects of dispersing metal particles into polymeric matrices using high-temperature processes.[1-3] However, less research has been done into forming metal-polymer composites by the low-temperature solid-state process of mechanical alloying, which has been shown to produce unique properties different from high-temperature processes.[4]

In mechanical alloying, two powders are placed in a vial with several hardened metal or ceramic charge balls. The vial is then milled by vigorous agitations, causing high-energy collisions between the balls in which powder particles are trapped between the balls, leading to deformation, fracture, and fusion of the powder particles. The important parameters in this process are milling time, specific energy input, and milling temperature. The specific energy input correlates to the mass of the charge balls compared to the mass of the powders in the vial, a parameter referred to as charge ratio.[5] Milling temperature can be controlled or allowed to increase due to the heat from the high-energy milling. Particle size decreases as milling continues, leading to closer interaction between the two powdered phases and, in many cases the formation of unique metastable structures.[4-5]

Mechanical alloying was originally developed by Benjamin *et al.* to produce oxide dispersion strengthened superalloys and has been studied extensively in metals to control microstructure, induce amorphization[7-9] and extend solubility limits.[6] Mechanical alloying has also been found to be a useful technique for forming polymer blends in the solid state.[5] In light of the potential property advantages that can be achieved with metal-polymer composites, it seems a logical next step to investigate mechanical alloying with metal and polymer powders.

Work done by Ishida and Tamaru studied the use of mechanical alloying to create metal-polymer composites with polytetrafluoroethylene (PTFE) powder for a polymer and copper or nickel for a metal. In both systems (PTFE/Cu and PTFE/Ni), the researchers found significant decreases in particle size with milling time.[4] Particle size was observed by Ishida and Tamaru to reach a steady state particle size by about 10 hours milling time.[4] However, other experiences with mechanical alloying of metals indicate that refinement of crystallite size can be achieved by continued milling once the steady state particle size has been reached.[10] This research will expand on the prior work described above with a new materials system and more emphasis on the resulting mechanical properties.

2. Procedure

2.1 Sample Preparation

The materials used in this research were a thermoplastic powder of poly methyl methacrylate (PMMA, >99% purity) produced by Precision Surfaces International (PSI-213-5) and a magnesium powder (99.8% purity, 50-100 mesh) produced by Atlantic Equipment Engineers. Mechanical alloying with a tungsten carbide vial and ball set was used to process the powders. A 19:1 volume ratio was held constant for the mixture of PMMA and Mg powders (5 V% Mg), which were prepared in an Ar-atmosphere glove box to avoid oxidation. The specific energy input was also held constant with a charge ratio of 3:1 (three charge balls with mass of 32.28 g, powder mass of 10.76 g). Five samples were prepared and milled for five milling times: 0, 1, 2, 5, 10 hours. Two control samples of pure PMMA with no Mg were also prepared, one not milled at all and the other milled for 10 hours, but with small samples removed at 1, 2, and 5 hours.

To assess the effect of milling time on mechanical properties (Vickers hardness) and microstructure, approximately five grams of each of the mixtures and the unmilled control were pressed into hardened specimens at 150˚C and 4 ksi (27.6 MPa) for 10 minutes. These specimens were then polished with alumina to the 0.05 µm particle size.

2.2 Thermal Analysis

The five mixture powder samples and the unmilled PMMA control powder were thermally analyzed using a Neztsch STA 449 C Jupiter simultaneous thermal analyzer to perform differential scanning calorimetry (DSC) and thermogravimetric analysis (TGA) concurrently. Each sample was heated from room temperature up to 350˚C at 20˚C/min in air to examine the alteration of the mixture with milling time. Sample masses were between 6 and 10 mg and the results were normalized by mass.

2.3 Microscopy

Optical microscopy was performed on the polished specimens at magnifications up to 100X to assess the variation in microstructure with milling time, particularly the interaction between the Mg and PMMA particles.

2.4 Hardness Testing

Vickers hardness tests (LECO LV 700 AT) were performed with 1 kgf for 10 seconds at ten locations on each of the hardened specimens for the five mixtures and the unmilled control. Averages of the ten readings on each were compared to analyze changes in mechanical properties with milling time.

2.5 Structure

The crystal structures of the four milled mixture powders and three milled compacts were analyzed by powder X-ray diffraction (XRD) using a PANalytical X'pert Pro PW3040 instrument. The peaks were analyzed to assess the decrease in Mg crystallite size with increasing milling time. Full-width half-maximum values were calculated by the X'Pert High Score Plus software at five prominent diffraction peaks as a function of milling time to quantify peak broadening and associated crystallite size reduction and d-spacing was used to analyze peak shifting.

2.6 Particle Size Analysis

A particle size analysis was performed on the micrographs at 5X and 10X magnifications using ImageJ 1.41 software. To perform this analysis, the micrograph images were converted first to 8-bit grayscale and then to binary by adjusting the threshold brightness to identify Mg particles from the PMMA matrix. The binary image was then refined to fill in holes and eliminate single-pixel indications. Finally, the software performed a particle size distribution analysis on the refined binary image to determine the average size (pixel area) and number of Mg particles in the micrograph. These pixel areas were converted to physical areas based on the magnification of the image and the average particle size for all the micrographs taken at the 5X and 10X magnifications were calculated. This limited sampling of the surface is not expected to give a definitive value for particle size as a function of milling time, but should provide an indication of the general trend, subject to variability.

3. Results and Discussion

3.1 Thermal Analysis

DSC and TGA curves for all five of the powder mixtures at milling times of 0, 1, 2, 5, and 10 hours are shown below in Figures 1 and 2, respectively, along with a 100% PMMA sample. All six DSC curves in Figure 1 show an endothermic event occurring from about 250-300˚C. This endothermic event decreases in intensity with increasing milling time and also occurs at a higher critical temperature as milling time increases. If one notes that the melting point of Mg is greater than 600^{o}C, it is safe to conclude that this endothermic event is the melting of the PMMA, which has been recorded in the literature to occur at 220-250^{o}C. It is, therefore, interesting to observe that the melting of the PMMA occurs with less intensity and at a higher critical temperature as milling time increases, probably due to smaller molecular weight as a result of bond-breaking during milling along with more intimate and homogeneous mixing with Mg. One should also note that by 10 hours milling time, the endothermic melting is no longer observed in the DSC curve, suggesting that the PMMA structure has been significantly changed due to the milling.

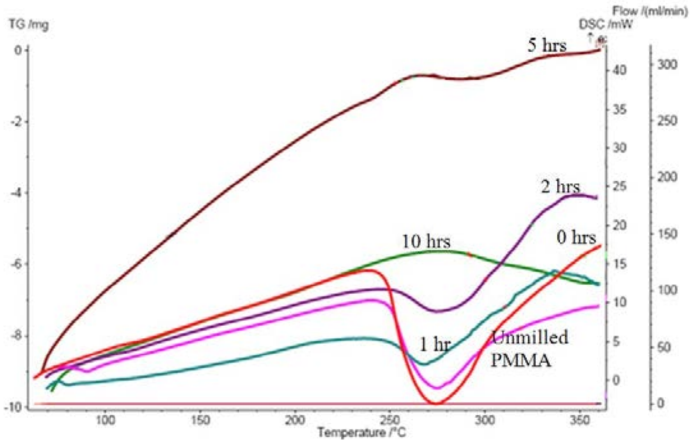

Figure 1: DSC curves for milling times of 0, 1, 2, 5, and 10 hours and unmilled pure PMMA

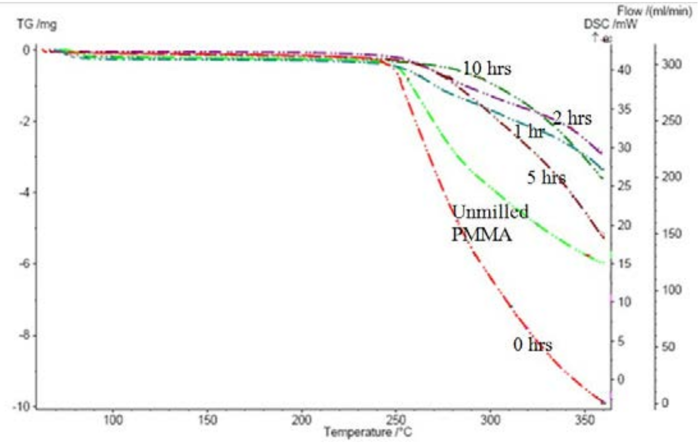

Figure 2: TGA curves for milling times of 0, 1, 2, 5, and 10 hours and unmilled pure PMMA

Consistent with the DSC curves, the TGA curves in Figure 2 show the greatest mass loss for the unmilled sample and decreasing mass loss with milling time. This would indicate that as milling time increases, less PMMA is melting and then volatizing to cause the loss in mass. The mass loss in the TGA also coincides with the endothermic event (PMMA melting and volatizing) seen in the DSC curves and shows the same increase in critical temperature with milling time that was observed by DSC. Overall, the thermal analysis by DSC and TGA indicates a change in the structure of the PMMA due to milling, most likely smaller molecular weights due to bond breaking during milling as seen by other researchers.[5] More intimate and homogeneous mixing with Mg with milling time could also contribute to the shift in critical temperature observed in the thermal analysis.

3.2 Microscopy

Micrographs of pressed specimens of the powder mixture are shown at 5x magnification in Figure 3. In Figures 3a and 3b, the decrease in magnesium (dark due to oxidation) particle size with milling time can be clearly seen. The PMMA is seen in these figures as the lighter region and is translucent when observed directly, allowing view of internal Mg particles. When the specimens are pressed with heat, the PMMA crosses its glass transition and flows easily to form a polymeric matrix around the Mg particles, allowing for easy analysis of the change in Mg particle size. A distinct heterogeneity is present in the 1 and 2 hour samples, with little to no fine mixing between the Mg and PMMA, but simply Mg particles suspended in a PMMA matrix.

In Figures 3c and 3d, the 5 and 10-hour milled samples can be seen, showing much more homogeneity than the shorter mill times. It is apparent that a significant transition occurs between milling times of 2 and 5 hours. Up to 2 hours milling, Mg particle size is decreasing with milling time, but the specimens are distinctly heterogeneous, with little or no fine mixing between the two phases. However, by 5 hours milling significant homogenization and fine mixing has occurred with a decreasing percentage of distinct Mg particles (now lighter regions due to less oxidation) present and an increasing percentage of matrix (darker due to dispersion of Mg), which consists of a mixture of PMMA and Mg. The key transition from 2 to 5 hours milling is in the degree of fine mixing of the two phases within the matrix; up to 2 hours milling, this matrix is composed almost exclusively of PMMA, but by 5 hours the matrix has begun to disperse and mix with Mg homogeneously.

In Figure 4, the four milled mixture samples can be seen at higher magnification, clearly demonstrating the change occurring within the matrix from pure PMMA to a fine homogeneous mixture involving Mg and PMMA. Figures 4a and 4b show a translucent matrix (now darker due to optical microscope effects) of pure PMMA with particles of Mg (grayish or black depending on oxidation at surface or being trapped internally) suspended, while Figures 4c and 4d illustrate an opaque matrix (multicolored region) of finely mixed PMMA and Mg still containing Mg particles (now primarily grayish), but in decreasing size and quantity. In Figures 4c and 4d, there appears to be a varied, almost bimodal distribution of particle sizes with the largest particles up to around 50 µm, ranging down to less than 10 µm.

3.3 Hardness Testing

Vickers hardness testing was performed on the pressed specimens to observe the effect of milling time on the mechanical properties of the material. Although hardness is just one surface measure of a material's mechanical properties, hardness measurements tend to reflect general trends of mechanical strengthening in a material.[11] The change in hardness with milling time is shown in Figure 5 for both pure PMMA and the 5 V% Mg mixture. The results of hardness testing showed an increase in hardness with milling time for the mixture and a decrease in hardness with milling for the pure PMMA. After 10 hours of milling, the mixture is significantly harder than the pure PMMA.

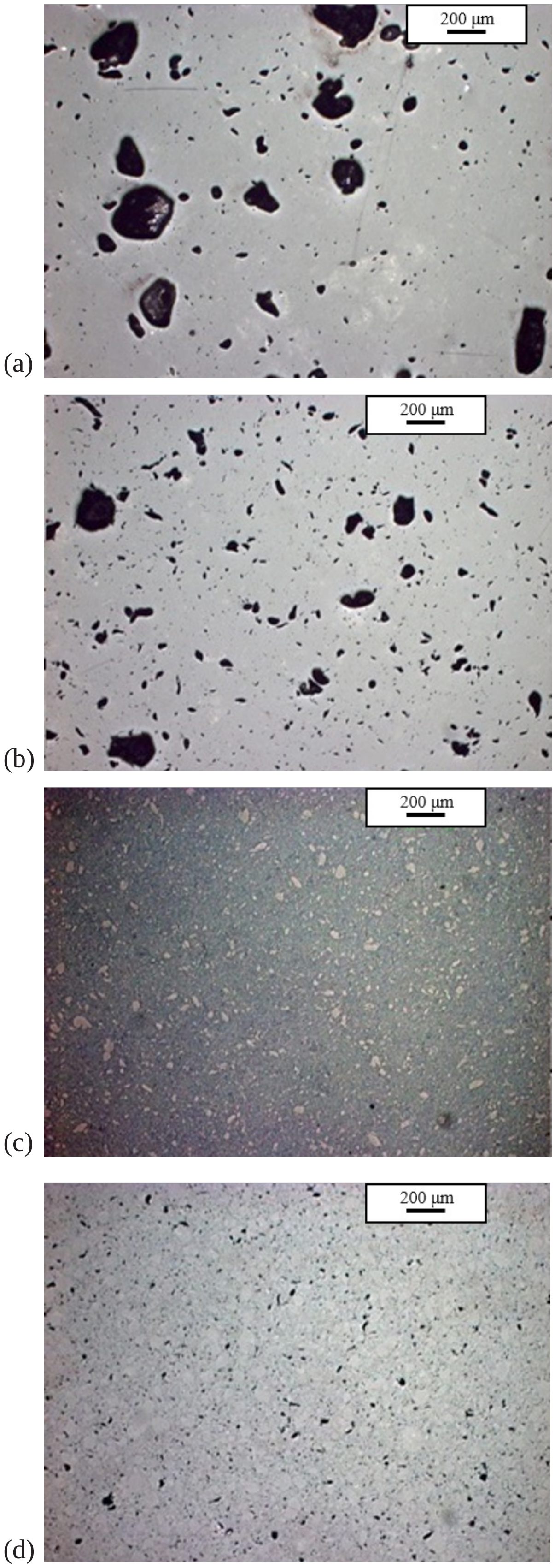

Figure 3: Micrographs at 5x magnification showing specimens milled for (a) 1 hour, (b) 2 hours, (c) 5 hours, and (d) 10 hours

However, the greatest average Vickers hardness recorded was for the unmilled pure PMMA, indicating that mixing with Mg and milling failed to improve hardness.

These results are consistent with experimental observations documented by other researchers mechanically alloying polymers[5] and can be explained by the degradation of the polymer during milling due to bond breaking and the corresponding chain molecular weight decrease. A reduction in hardness with increasing milling time is clearly observed in the pure PMMA data and is most likely caused by PMMA degrading during milling. Little change is seen from 5 to 10 hours as it appears that a steady state chain molecular weight is reached by 5 hours milling, with little change occurring due to additional milling. Likewise, the trend of increasing hardness in the PMMA/Mg mixture could be explained by the fine homogeneous mixing of the two phases leading to a strengthening of the matrix. The milling process yields Mg dispersed very finely within the PMMA matrix, offering strengthening over the milled pure PMMA.

3.4 Structure

The structure of the powders as a function of milling time was analyzed by XRD to see the effect of milling. The full XRD spectrum can be seen for the powder form in Figure 6. A similar XRD curve was observed for the compact form not shown. Observation of the largest Mg peaks from the powder and compact forms demonstrates the decrease in Mg peak intensity with milling time. This decrease in peak intensity is caused by the decrease in crystalline particle size and crystallite size within the particles with milling time. Decreasing crystallite and particle size with milling seen in the XRD peaks correlate well with increasing hardness with milling. These decreases in particle and crystallite size can also be observed through peak broadening in the XRD spectrum by analysis of the change in a particular peak's full-width at half-maximum (FWHM). Particle size analysis by observation of optical micrographs provides another assessment of change in crystalline particle size, although not crystallite size.

Observation of peak broadening with increasing milling time shows that significant crystallite size reduction does not occur until 5 hours milling time as the 1 and 2 hours milled curves are quite similar, but considerable intensity decreases are seen at 5 and 10 hours milling. There is also an indication that a grain texture may be forming, due to the differing drops in peak intensity with milling time in the largest peaks. This differing peak behavior with milling indicates that preferential grain alignment is occurring among the crystallites within the Mg particles.

To analyze potential grain texture, crystallite size inferred from XRD peaks was plotted against milling time utilizing the Scherrer formula to calculate "effective crystallite sizes" from XRD peak broadening in the compact and powder form of the mixture.[7] In this analysis, with random grain orientation the various diffraction peaks should give the same

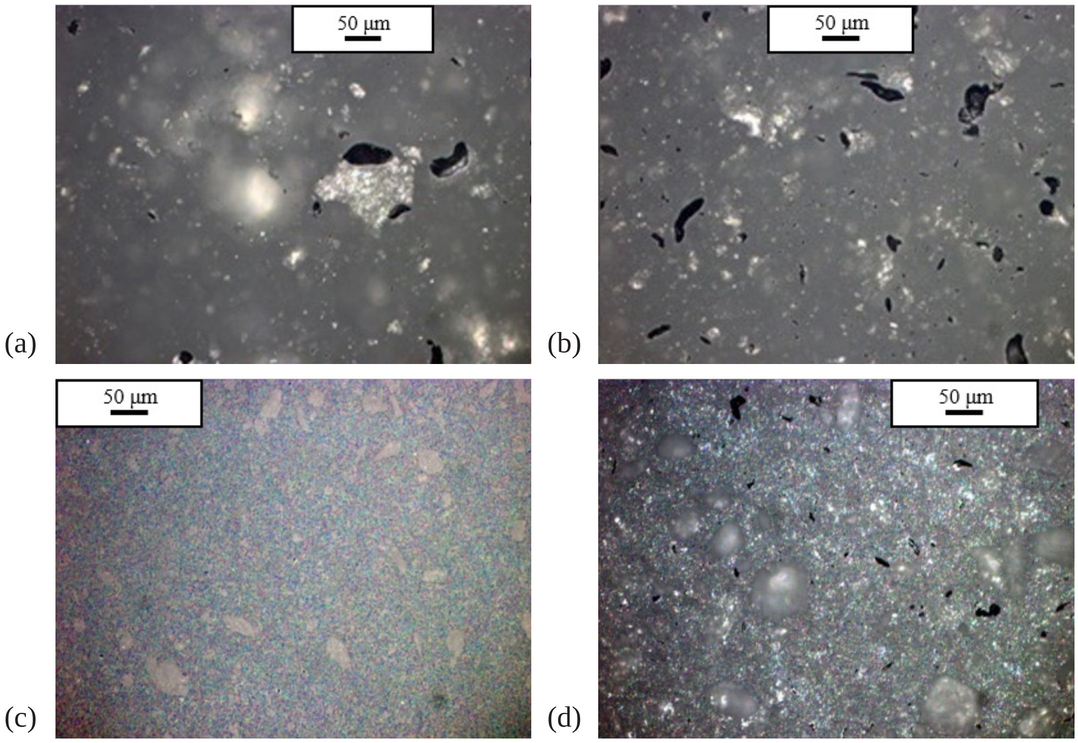

Figure 4: Higher magnification micrographs; (a) 1-hour milling at 20x, (b) 2-hour milling at 20x , (c) 5-hour milling at 20x, (d) 10-hour milling at 20x

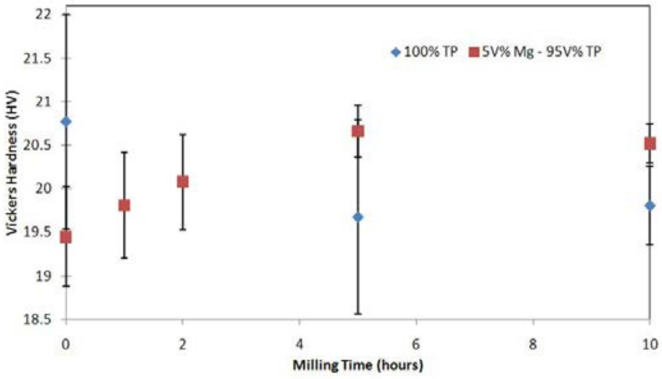

Figure 5: Comparison of Vickers hardness for pure PMMA and mixture as a function of milling time with error bars of one standard deviation

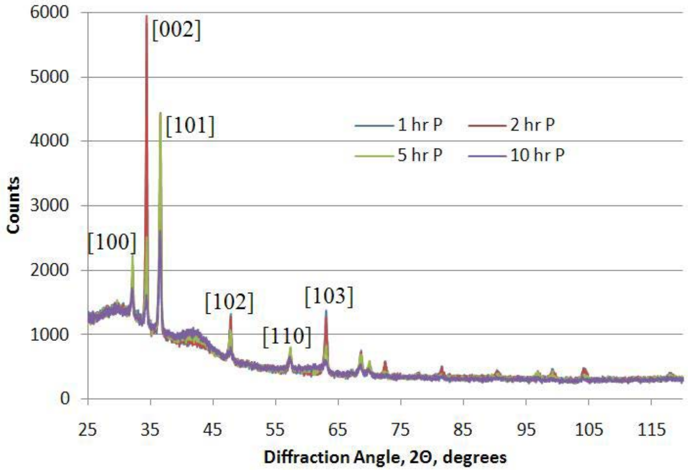

Figure 6: XRD graph for PMMA/Mg powder mixture for 4 milling times with full spectrum.

effective crystallite size because they are reflecting from the same lattice. If the sizes are not the same, this indicates the development of grain texture to cause preferential alignment of the grains. This analysis for both the powder and compact forms show little numerical indication of grain texture.

These largest Mg peaks also show some evidence of peak shifting with increasing milling time, with the peak angle variation potentially indicating a changing lattice parameter. To assess this, d-spacing was calculated for the largest XRD peak on the spectrum centered at about 2Θ = 34.3˚. These results seem to show a slight increase in the d-spacing with milling time, indicating the lattice planes are becoming slightly more spread apart, which could be caused by the minor diffusion of interstitial carbon into the Mg crystalline matrix with milling. However, while these trends are common in both the powder and compact form, it is difficult to draw any strong conclusions of the cause due to the small variation in d-spacing.

3.5 Particle Size Analysis

To optically assess the change in Mg particle size with milling time, a particle size analysis was performed using micrographs at 5X and 10X magnification along with ImageJ software as described in the procedure section. This particle size analysis showed an expected sharp decline in visible particle size with milling time. Similar to the other analyses, the majority of the change in particle size occurred up until 5 hours milling, with very little change beyond that point. Figure 7 shows a graph of average particle size against

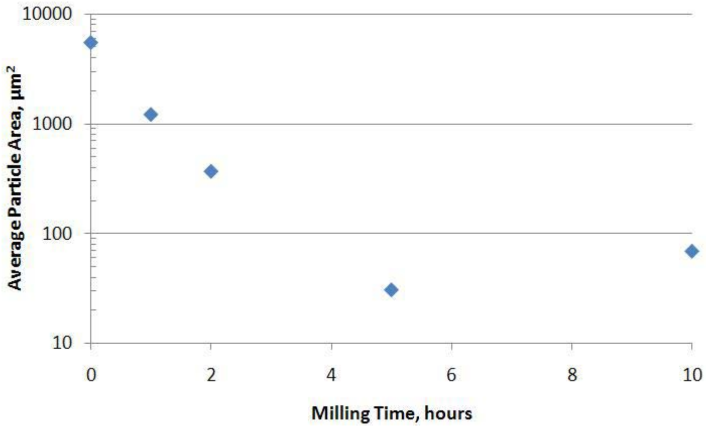

Figure 7: Particle size analysis results from micrographs at 0, 1, 2, 5, and 10-hour milling times

milling time illustrating the sharp reduction in particle size from 0 to 5 and 10 hours milling. The particle size analysis is generally consistent with other analyses performed, showing that the greatest effect of milling is seen up to 5 hours, with little change from 5 to 10 hours milling.

4. Summary

Low-temperature, solid-state mechanical alloying was used to produce metal-polymer composites of Mg and PMMA resulting in unique structures and altered mechanical properties. X-ray diffraction and microscopy point clearly to a reduction in Mg particle and crystallite size and increasing homogenization of the Mg within PMMA matrix with milling time. Hardness of the mixture increases with milling time, due to fine mixing and homogenizing of the matrix with milling, improving on the decreasing hardness trend exhibited by pure PMMA when milled.

This research provides a baseline for further work involving metal-polymer composites and mechanical alloying. The technique of mechanical alloying is ideal for producing metal-polymer composites, but is in need of more study and fine-tuning of the composition and milling time to maximize the resulting material's properties.

Acknowledgements

This work was done as part of undergraduate research, under the supervision of Dr. Alex Aning. Dr. Aning provided guidance, direction, and support in this work, along with doctoral students Andrew Zeagler and Niven Monsegue for technical guidance on the paper and laboratory equipment education with using the XRD, DSC, and optical microscope. I would also like to acknowledge the Virginia Tech Department of Materials Science and Engineering for the equipment and space that made this research possible.

References

1. Nesher, G.; Marom, G.; Avnir, D. Chemistry of Materials **2008**, 20, 4425-4432.

2. Nicodemo, L.; Nicolais, L. Journal of Materials Science Letters **1983**, 2, 201-203.

3. Bloor, D.; Donnelly, K.; Hands, P. J.; Laughlin, P.; Lussey, D. Journal of Physics D: Applied Physics **2005**, 38, 2851-2860.

4. Ishida, T.; Tamaru, S. Journal of Materials Science Letters **1993**, 12, 1851-1853.

5. Farrell, M. P.; Kander, R. G.; Aning, A. O. Journal of Materials Synthesis and Processing **1996**, 4, 151-161.

6. Benjamin, J. S. Metallurgical Transactions **1970**, 1, 2943-2951.

7. Aning, O.; Wang, Z.; Courtney, T. H. Acta Metallurgica et Materialia **1992**, 41, 165-174.

8. Schwarz, R. B. Materials Science and Engineering **1988**, 97, 71-78.

9. Petzoldt, F. Journal of the Less-Common Metals **1988**, 140, 85-98.

10. Benjamin, J. S. Scientific American **1976**, 5, 40-48.

11. Pilipenok D. A.; Melentev, P. V. Mechanics of Composite Materials, **1965**, 1, 110-112.

About the Author

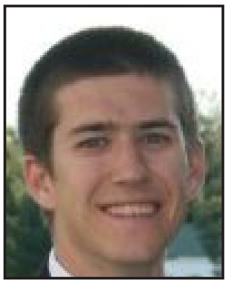

Mr. Hiser earned his bachelor's degree with honors in Materials Science and Engineering at Virginia Tech in 2010. He was honored as the Virginia Tech College of Engineering Outstanding Senior and ACC Undergraduate Research Scholar and held a position as co-op with the Nuclear Regulatory Commission (NRC).

Contact at: mhiser@vt.edu

Aerogel Fabrics in Advanced Space Suit Applications

Cameron Crowell[1], Cameron Reynolds[1], Andrew Stutts[1], and Hunter Taylor[1]

[1] Virginia Tech, Department of Materials Science and Engineering, 213 Holden Hall, Blacksburg, VA 24061

Abstract

New insulating materials for spacesuits will need to be able to function well in low-pressure and gaseous environments, such as the Martian atmosphere. In order to address this need, Orbital Outfitters, a small spacesuit company, is currently investigating new materials for the insulating layer of the space suit. One such material is an aerogel fabric composite, promising because of its flexibility and low thermal conductivity. The purpose of this study is to characterize the effect stitching an outer layer has on the stiffness, strength, and thermal conductivity of two types of aerogel fabric, ThermalWrap and Pyrogel 2250. Tension tests were used to investigate the mechanical properties, while two different methods were used to evaluate the thermal conductivity of the materials. Results showed a dramatic increase of thermal conductivity when an outer material was stitched directly to the aerogel fabric, while two other geometries showed a decrease in thermal conductivity. Tension tests revealed that stitching increased the strength of the ThermalWrap. Overall, it was determined that stitching the material was not a viable option due to the increase in thermal conductivity and difficult manufacturing. The two other geometries tested proved much more effective, as they were easier to manufacture and showed a decrease in thermal conductivity.

Keywords: aerogel, pyrogel, thermalwrap, thermal conductivity, space suits

1. Introduction

Current spacesuit multi-layer insulation (MLI) is very heavy and has a baggy look while in use. NASA astronauts wear the current suit during extra-vehicular activity (EVA) missions, more commonly known as spacewalks, while stationed in the International Space Station. Figure 1 shows a breakdown of the components in MLI.

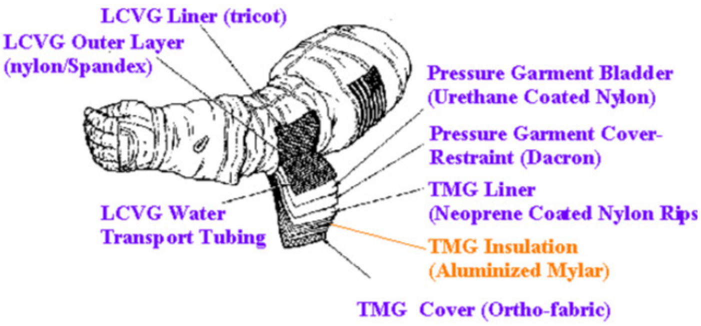

Figure 1: Current NASA standard MLI space suit[1]

Although the current design works well for its intended function in Low Earth Orbit, they would not adequately insulate in higher pressure environments such as the Martian atmosphere[1]. To address this issue, Orbital Outfitters and NASA are separately investigating and testing new candidate materials for use as insulation in a future space suit design. These materials must be flexible, lightweight, and have low thermal conductivity. Fabric aerogel composites have shown promise as light, thin insulation that can meet the requirements of an insulating layer for a spacesuit without adding excess bulk. Orbital Outfitters has partnered with this senior design group in seeking to describe the properties these aerogel fabric materials used as an insulating layer would give to a spacesuit. Orbital Outfitters is also interested in the effect of stitching on thermal conductivity and mechanical strength of fabric aerogels.

1.1 NASA Standards

NASA has determined that the maximum thermal conductivity value for an insulating layer used in the future space suit be 0.005 W/m*K (5 mW/m*K) at pressures between 10^{-6} and 8 torr. In addition to thermal conductivity standards, NASA also set an operating temperature range of -157 ^{o}C to 121 ^{o}C, a maximum thickness of 12.7 mm, and a denstiy of less than 0.68 kg/m^{2}.[1]

1.2 Overview

This study aims to investigate and determine the effect that stitching has on the thermal insulation and mechanical characteristics of aerogel fabric. Two different materials were studied, Thermal Wrap and Pyrogel 2250. Both contain granules of silica aerogel suspended in a nonwoven polymer fiber matrix and can be seen in Figure 2. To evaluate the materials, several different tests were run to ensure that they would not degrade in the operating temperature range suggested by NASA. Enough material was used to show the representative behavior of the bulk materials. Once baselines were established, stitched samples were manufactured and tested.[1,7]

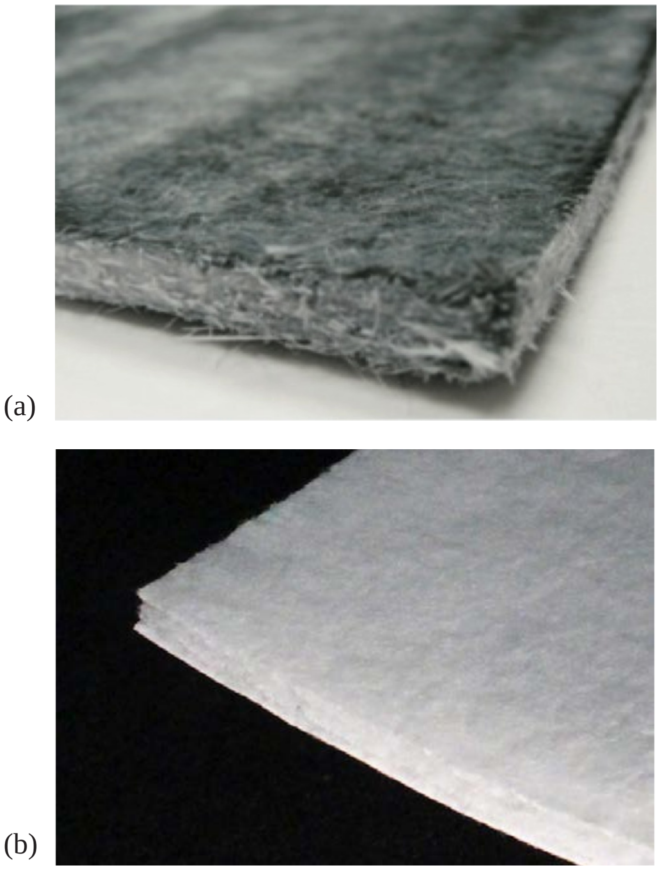

Figure 2: (a) Thermal Wrap (b) Pyrogel 2250. Both fabrics are approximately 3mm thick.

2. Procedure

2.1 DSC

A TA Instruments Q20 Differential scanning calorimeter (DSC) was used to investigate any possible physical transitions (such as glass transition or phase transitions) experienced by the materials when heated. Due to physical limitations of the machine in relation to sample size, only Thermal Wrap 350 and Pyrogel 2250 were able to be tested. Each sample was taken from room temperature to 140^{o}C in the DSC at a rate of 10^{o}C/min. Results were analyzed following the testing.

2.2 TGA

Thermogravimetric analysis (TGA) testing was done with a TA Instruments Q50 to determine if the materials would be usable in the NASA specified temperature range. Both the Thermal Wrap and Pyrogel 2250 materials were prepared and tested using a ramp from room temperature to 750^{o}C. A ramp rate of 20^{o}C/min was used for all tests. Since the maximum operating temperature was set at 121^{o}C, results were examined between 20 and 140^{o}C for each sample run.

2.3 DMA

Dynamic mechanical analysis (DMA) was performed on the samples with a TA Instruments Q800 to determine how their flexibility changes with temperature. Both static force bending and static force tension tests were run on rectangular samples, with a temperature range of -140 to 140^{o}C.

2.4 Tension Testing

To test the unstitched aerogel material in tension, 150 x 25 mm samples were cut out from the larger sheets of material. An ASTM standard dogbone could not be used due to the difficulty in cutting the material. Extra consideration was also taken to investigate whether heat exposure would affect the flexibility of unstitched material. Samples of each type of fabric were heated in a furnace for eight hours at 121^{o}C. This time and temperature combination represents the most extreme conditions that would be expected from an EVA mission and the highest range of NASA specified temperature.[4] After heating, the samples were then tested in tension in an Instron with roller grips to determine whether there was a significant change to the flexibility.

For the quilted samples, the larger 127 mm squares were cut into strips. Each square was able to yield several tensile specimens. To test the outer muslin fabric, 150 x 25 mm strips were cut from a larger sheet of material. The samples were loaded onto an Instron load frame with a 5 kN load cell using fabric roller grips. All of the samples were tested at a constant strain rate of 10 mm/min.

2.5 Hot Disk Testing

Initial thermal conductivity measurements were taken using a Hot Disk thermal measurement system with a 9.73 mm radius Kapton sensor. Prior to testing the aerogel samples, the machine was calibrated using two stainless steel calibration disks. Following calibration, two small samples of material were cut out and used, sandwiching the Kapton sensor in between them. The samples and sensor were held in place using a screw apparatus to ensure that they would not move during testing and disrupt measurements.

2.6 Forward Looking Infrared (FLIR) Imaging

Infrared video of the samples being heated was captured using two FLIR A665sc cameras. Before imaging, each sample was topically coated using Rust-Oleum High Heat black spray paint to get a known emissivity value on the surface of the samples. Once the coatings were properly applied and dried, the samples were hung on a static load frame using 24 gauge stainless steel wire. One FLIR camera was set in front of the samples and focused to capture the front of the sample. The second FLIR camera was placed at an angle behind the sample and focused to capture the back of the sample. Four quartz-panel heaters were placed behind the samples and set at 497^{o}C to produce a heat flux of 10 kW/m^2. The samples were heated and IR images were recorded for 30 minutes each, ensuring that they reached a steady-state of through-thickness heat diffusion.

3. Results and Discussion

3.1 Proof of Concept

The results obtained from the thermogravimetric analysis indicated that no thermal degradation occurred in the Thermal Wrap and the Pyrogel 2250 samples in the typical EVA temperature range. The DSC measurements revealed that in the Thermal Wrap samples there was melting occurring in the material at 121.76^{o}C, right outside the typical EVA range. This is attributed to the proprietary copolyolefin sheath of the matrix fibers melting.[8] The DSC findings for the Pyrogel did not indicate any physical transitions upon heating. The flexural modulus of both materials did show a temperature dependency, according to the DMA results. These changes ranged, for ThermalWrap, from 9.06 Pa to 115 Pa and from 92.8 Pa to 360.5 Pa, for Pyrogel.

3.2 Recommendation Testing

3.2.1 Thermal Conductivity Testing

Both the HotDisk and FLIR thermal conductivity measurement systems proved to be fruitful measurement techniques. The thermal conductivity results for the various geometries of both ThermalWrap and Pyrogel are shown in Figure 3a below. No measurements were obtained for the pocketed ThermalWrap and quilted Pyrogel samples due to issues in fabrication: the pocketed ThermalWrap samples were not fabricated in time, and the Pyrogel fabric could not be punctured by the needle and therefore could not be stitched. No HotDisk data were taken for the windowed and pocketed samples, because the contours and changes in topography of these samples proved to be too great and made measuring thermal conductivity accurately with the HotDisk impractical. The simplified findings of the plot in Figure 3a are shown in Figure 3b.

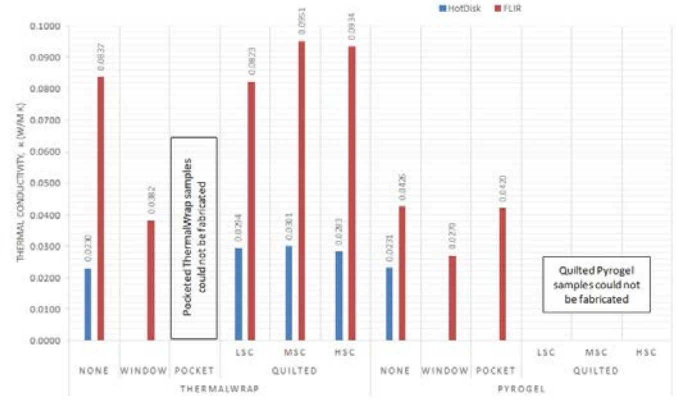

Figure 3a: Thermal Conductivity of Various Samples measured by HotDisk and FLIR. The seemingly large systematic difference between the two methods is apparent because the HotDisk is measuring a single area, and the FLIR is averaging larger areas in the sample. LSC, MSC and HSC stand for low stitch count, medium stitch count and high stitch count, respectively.

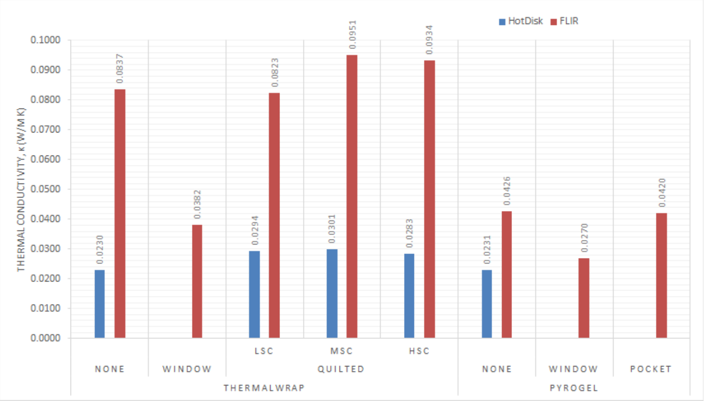

Figure 3b: Thermal Conductivity of various samples measured by HotDisk and FLIR

The Hot Disk measurements show that the Thermal Wrap and Pyrogel samples exhibit almost the same thermal conductivity without stitching. It is also shown that for the stitched Thermal Wrap samples there is an apparent increase in thermal conductivity for all stitch counts compared to unstitched. Similarly, for the FLIR data, there appears to be an increase in thermal conductivity for all samples other than the low stitch count. Conversely, the FLIR data in Figure 3b shows that in all instances, both for the Thermal Wrap and Pyrogel, there was a decrease in thermal conductivity in the windowed and pocketed samples.

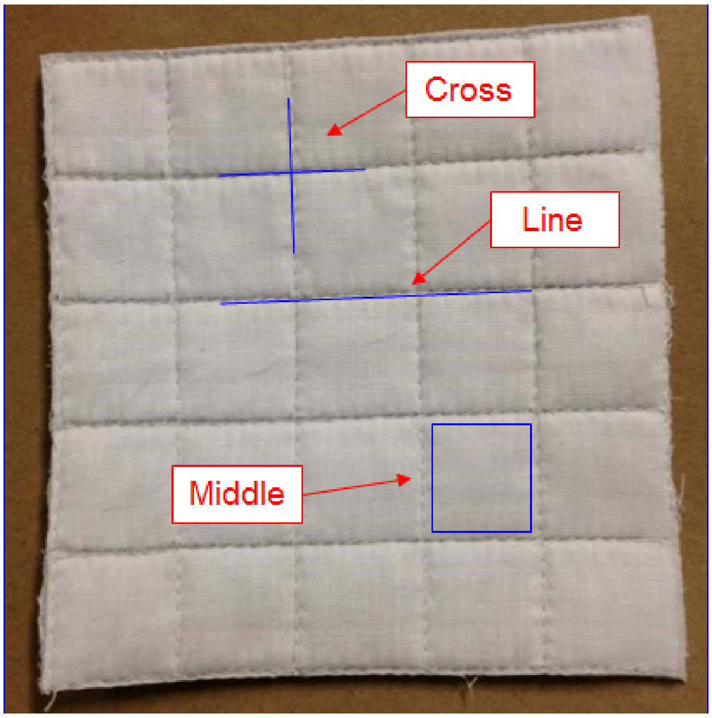

Figure 4: Stitched thermal wrap sample showing zones.

To obtain a better idea of how the stitching affected the thermal conductivity of the aerogel fabrics the thermal conductivity was measured at different zones: lines, which are linear sections of stitching, crosses, where two lines intersect, and middles of the stitched samples, where no stitching is present. Figure 4 shows the different zones of the stitched samples. Crosses were the intersection of two lines of stitching, while lines were single lines of stitching, and middles were unstitched areas.

Figure 5 summarizes the measurements of thermal conductivity for the stitched Thermal Wrap samples in different zones. Measurements by HotDisk are shown first in the blue colors and those measured by FLIR are shown second and in shades of red. The horizontal lines represent the thermal conductivity values of the unstitched samples as measured by HotDisk (bottom, green) and FLIR (top, orange). The data in Figure 5 confirm the observation made from Figure 3b that the addition of stitching increases thermal conductivity, regardless of measurement technique. The FLIR measurements also have a much larger standard deviation than any other measurement shown in Figure 5. Also of note is that there seems to be a large increase in thermal conductivity in the samples measured in FLIR compared to those measured using the HotDisk.

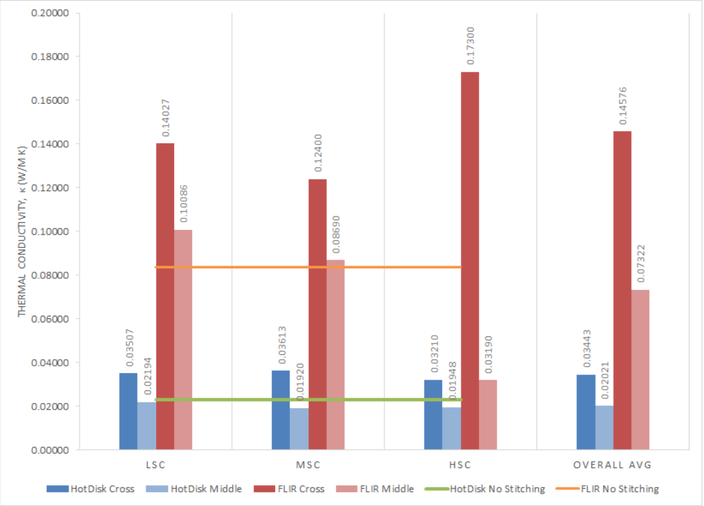

Figure 5: Thermal conductivity of stitched thermal wrap samples in different zones by hot disk and FLIR

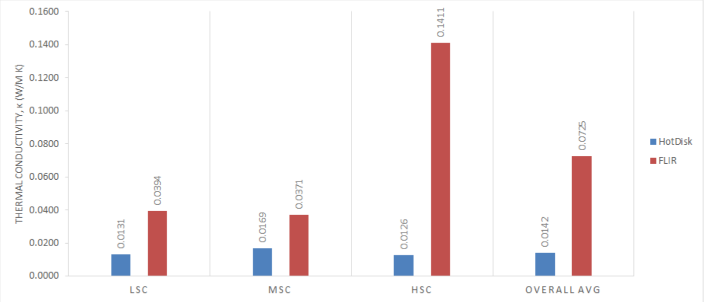

Figure 6: Change in thermal conductivity upon stitching of thermal wrap for various stitching densities

These results can be further summarized by the plot in Figure 6. Here the net change in thermal conductivity from stitching is shown, in all cases the change is an increase. As previously mentioned, the FLIR measurements have both a larger increase in thermal conductivity than the Hot Disk measurements as well as a larger standard deviation when comparing stitched samples to unstitched samples.

To further understanding of what significantly affects the thermal conductivity results, an analysis of covariants (ANCOVA) was done for the Hot Disk data. ANCOVA is a statistical analysis tool that is used to create a linear model to estimate how much change each factor and the interactions between the factors contributes to the results. One level of each factor is arbitrarily chosen as a baseline of comparison for the other levels in that factor. The analysis in this report chose the low stitch count and cross zones as the baseline of comparison, and the model equation is shown below in Equation 1.

$$\kappa = \beta_o + (\beta_1 \cdot stitch_i) + (\beta_2 \cdot zone_i) + (\beta_3 \cdot stitch{:}\, zone_i) + (\beta_4 \cdot probedepth) + \varepsilon_i$$
$$i = 1,2,3..$$

Equation 1: ANCOVA model for hot disk data

In Equation 1, κ is the thermal conductivity measured by the instrument, β_0 is the intercept of the equation, and ε_1 is the error involved. β_1, β_2, β_3 and β_4 are either 1 or 0, depending on which area of the sample is being interrogated. The stitch:zonei and probedepth variables are the interactions between the zone and stitch factors and the machine variance, respectively. Probe depth is the size of the area measured by the Hot Disk.

The results of the ANCOVA analysis show that all the variables included in the model significantly affect the thermal conductivity reported by the Hot Disk. This is determined by the p-value, which is a measure of the probability that the estimated value occurs by random chance. For this project, any factor that has a p-value less than 0.05 is considered significant. This p-value corresponds to a 95% confidence that the estimates calculated for the factors and levels chosen are realistic approximations for how the stitching affects the thermal conductivity.

Finally, the analysis results show that both the medium and high stitch counts increase the thermal conductivity over the low stitch count, but, surprisingly, the medium stitch count increases the thermal conductivity more than the high stitch count. This can be attributed to the difficulty in manufacturing of the samples, as the seamstress reported that some rows had to be stitched over and some stitches were skipped because of the nature of sewing a non-woven fabric filled with aerogel. The line zone showed an increase in thermal conductivity, and the middle zone a decrease compared to the cross zone, which was expected. The largest contribution to the thermal conductivity reading was the machine variance itself, since the probe depth gives the highest estimated contribution. This is also expected, as the HotDisk was being operated near its lower ability to give accurate results, where intrinsic error becomes a larger factor.

This table shows the numerical values resulting from an analysis of covariants done on the HotDisk data. The first column is the estimated value that each level of each factor contributes to the thermal conductivity results, in W/m^{2}K. The second column is the standard error calculated between three data points in each row, and the third column is the t-value which is the estimate divided by the standard error. The last column shows the p-values, which are the probability as to whether or not the estimated values occur by random chance or not. The closer the p-values are to zero, the lower the chance that the t-values are a random occurrence.

Table 2: Young’s Modulus in relation to stitch count.

Stitch Count	**Young’s Modulus (MPa)**	**Stand. Dev (MPa)**
Low	20.13	6.49
Medium	13.10	1.20
High	13.80	1.41
Outer Fabric	161.05	13.45

Table 1: ANCOVA of Hot Disk Results

	Estimate	Std. Error	t value	Pr. t
(Intercept)	0.0122	0.0023	5.407	4.715E-05
Stitch350 HSC	0.0031	0.0010	3.164	5.677E-03
Stitch350 MSC	0.0061	0.0010	6.690	3.802E-06
ZoneLine	0.0090	0.0011	7.845	4.758E-07
ZoneMiddle	-0.0031	0.0012	-2.541	2.108E-2
ProbDepth	0.0141	0.0013	10.477	7.790E-09
Stitch350 HSC:ZoneLine	-0.0077	0.0014	-5.574	3.358E-05
Stitch350 MSC:ZoneLine	-0.0010	0.0014	-7.298	1.244E-06
Stitch350 HSC:ZoneMiddle	-0.0029	0.0011	-2.573	1.975E-02
Stitch350 MSC:ZoneMiddle	-0.0074	0.0011	-6.484	5.612E-06

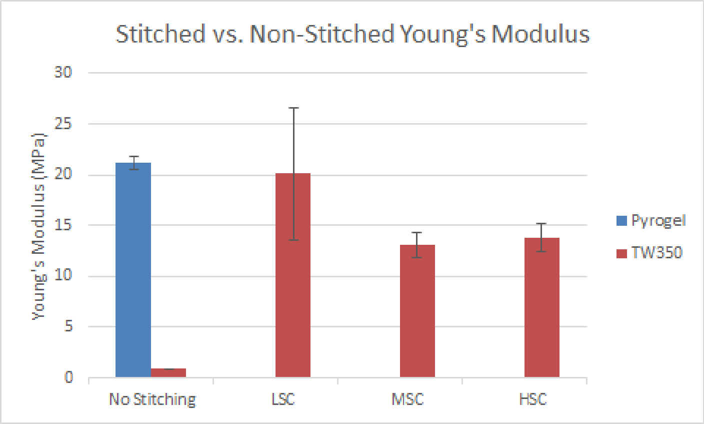

Figure 7: Young’s Modulus in relation to stitch count.

3.2.2 Mechanical Testing

The results of the tension tests run on the stitched Thermal Wrap samples are shown in Table 2. The tests were performed with a strain rate of 10mm/min.

From Table 2 and analysis of variance it can be seen that the stitch count does not have an effect on modulus. However, stitching an outer layer directly to the Thermal Wrap samples did increase the resilience of the material system when compared to normal, non-stitched samples. During the tests, the inner aerogel fabric would tear at very low loads, but the overall structure of the system would remain intact for a significantly higher strain. This is encouraging, as it indicates a minimal loss of aerogel insulation even after the insulating layer has failed within the system. Further testing would be needed to quantify the ability of the system to insulate following inner aerogel failure.

The null hypothesis is that the stitch count did not have an effect on modulus and since our p-value is greater than our alpha of 0.05 and our f value was less than our f-crit we fail to reject the null and will proceed with the assumption that stitch count does not have an effect in this stitch density range.

Figure 8 shows that the outer fabric increased breaking strength and that the stitch count did not have an effect on strength in the range of stitch density we looked at.

Table 3: ANOVA comparing stitch counts

ANOVA						
Source of Variation	*SS*	*Df*	*MS*	*F*	*P-value*	*F crit*
Stitch Density	104.97	2.00	52.49	3.34	0.08	4.26
					F < F crit	
Total	246.28	11.00		α=0.05	P>α	

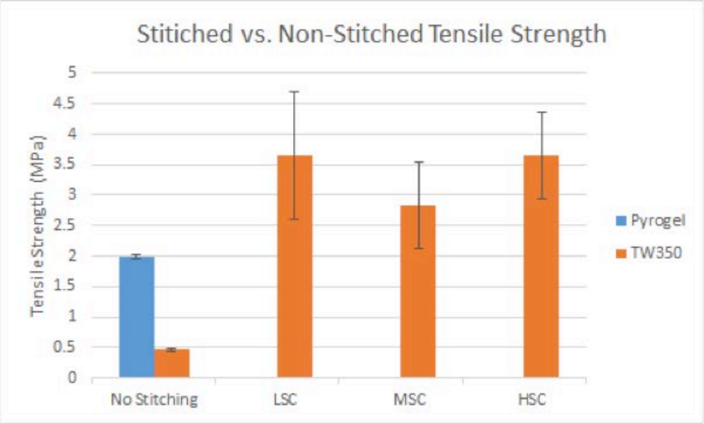

Figure 8: Breaking strength in relation to stitch count.

4. Conclusions

4.1 Materials Conclusions

From the results of this project, two major conclusions have been drawn. First, it is clear that stitching an outer fabric layer directly onto the aerogel fabric is not a viable option. This is due to the fact that the stitching had a significant negative impact on the thermal conductivity of the material system and the difficulty in manufacturing the samples. Without either a way to mitigate the increase in thermal conductivity at the stitches or a much better method of manufacturing the samples, this will not be an optimal geometry.

Second, it has been determined that future work with this materials system should focus on the windowed and pocketed geometries with Pyrogel inside. The Pyrogel demonstrated a lower thermal conductivity and is more mechanically sound than the thermal wrap. Additionally, the windowed and pocketed geometries exhibited a reduction in thermal conductivity, as compared to both the unstitched and stitched samples.

4.2 Future Work

Future work should investigate the effects of lower pressure environments on the thermal conductivity of the material. Literature indicates that a reduction in external pressure will reduce the thermal conductivity for several materials,[3] so it should be determined if this holds true for the aerogel fabric systems as well. Also, different geometries that would work well in flexible joints will need to be investigated. Having adequate thermal protection without sacrificing mobility at joints will be a mission critical aspect to future space suits.

Acknowledgements

This work was performed at Virginia Tech as a senior design project under the supervision of Dr. Scott Case and in collaboration with Orbital Outfitters in California. In addition to Dr. Case, the team would like to thank Thomas Staley, PhD^2, for his valuable input during the course of the year, Sarah Mgeni, Christine Burgoyne, Dr. Patrick Summers, as well as the Departments of MSE and ESM at Virginia Tech for the use of lab space and equipment.

References

1. Tang, H.; Orndoff, E.; Trevino, L. SAE Technical Papers **2002**, 2002-01-2316.

2. Tang, H.; Orndoff, E.; Trevino, L. SAE Technical Papers **2003**, 2003-01-2446.

3. Tang, H. H.; Orndoff, E. S.; Trevino, L. A. SAE Technical Papers **2006**, 2006-01-2235.

4. Paul, H. L.; Diller, K. R. Journal of Biomechanical Engineering **2003**, 125, 639-647.

5. Ordnoff, E.; Trevino, L. A. SAE Technical Papers **2006**, 2006-01-2235.

6. Tang, H. H.; Orndoff, E. S.; Trevino, L. A. SAE Technical Papers **2001**, 2001-01-2166.

7. Trevino, L.; Orndoff, E.S. NASA Johnson Space Center Unpublished

8. Cabot Aerogel Thermal Wrap **2013**, Material Safety Data Sheet.

Authors

Cameron Crowell received his bachelor's in materials science and engineering in the spring of 2015 at Virginia tech. He is an advocate for the space industry and is pursuing a master's degree focused on nano-structured metals. Contact at: ccrow@vt.edu

Cameron Reynolds is currently employed as a Research and development engineer for Bridgestone Americas in Mesa, Arizona,working on producing natural rubber from Guayule. While in college, he played intramural hockey and was the president of the Materials Engineering Professional Societies at Virginia Tech.

Andrew Stutts graduated in 2015 with his bachelors in MSE from Virginia Tech. He is currently working as a process engineer at Corning and enjoys spending time outdoors when not working.

Hunter Taylor is an athlete who played on the USA Ultimate Frisbee team while in his senior year in college. He now works for Matsys Inc. working in powder metallurgy.

Exploration of Shape Memory Polymer for Automotive Coating Applications

Ming Wang

Institute of Research for Technology Development of University of Kentucky, College of Chemical and Materials Engineering, 117 F. Paul Anderson Tower, Lexington, KY 40506

Abstract

Shape memory polymer (SMP) is one special kind of polymer which can recover back to permanent shape after being mechanically deformed. As for automotive coating, most of the defects occurs on the clear coat layer, if it can be replaced by shape memory polymer, the defects can be easily removed due to the self-healing ability of shape memory polymer. In this experiment, the self-healing ability of epoxy based shape memory polymer thin film (around 100µm) is examined. Five indents on the thin film shape memory polymer with depths from 4.9µm to 5.5µm are all disappeared after 15 minutes heating at 70^{o}C. The average hardness of the polymer is 165 ± 2MPa and the modulus is 5.76 ± 0.02GPa (assume Possion's ratio 0.4).

Keywords: Epoxy, shape memory polymer, automotive coating,

1. Introduction

Shape memory polymer is one class of the smart materials.[1] Shape memory polymer, typically has two different phases: the permanent phase (frozen phase) and temporary phase (reversible phase). The cause of the recoverability of shape memory polymer is based on the change of properties of the cross lined polymer chains. When the shape memory polymer is deformed by mechanical deformation and fixation of that deformation, the polymer will stay in the deformed phase, which is so called temporary phase. Once the deformed polymer is exposed to an appropriate external stimulus, the polymer recovers back to the permanent phase. Such deforming-recovering cycle can be repeated for several times.[2]

1.1 Thermalset Epoxy Shape Memory Polymer

The shape memory polymer used in this experiment is an epoxy shape memory polymer. This polymer's recover ability can be triggered through thermal stimulus. The recoverability is based in the change in material properties above and below the glass transition temperature, T_g. At temperature above T_g, the polymer is in a rubbery state and the polymer chains have a high number of available configurations. When external mechanical deformation is applied, the spatial change will limit chains' mobility and decrease the entropic energy. To create the shape of permanent phase, the polymer needs to be heated above T_g and an external mechanical load applied. With the load still applied, cool down the temperature to below T_g. Once the temperature is below T_g, the polymer will change from a rubbery state to a glassy state (temporary phase) and the available configurations are significantly decreased. When the temperature is above T_g again, the entropic energy increases and the polymer can recover its original set shape.

The chemical compositions of this epoxy based shape memory polymer are EPON 826, Jeffamine D-230 and NGDE. During the curing process, the EPON 826 chains will cross link with Jeffamine D-230, therefore creating cross-linked points. As the glass transition temperature is closely related to chains mobility and the chains mobility is related to the flexibility. By replacing EPON 826 with NGED, a flexible aliphatic diepoxide with lower epoxy equivalent weight (108) than EPON 826 (approximately equal to 180), the crosslink density and flexibility of the polymer will increase. Therefore, the glass temperature of shape memory polymer will decrease. Based on Tao Xie's previous paper, when the molar ratio of EPON 826 and NGDE is 3:1, the glass transition temperature should be around 70^{o}C.[2]

1.2 How may epoxy polymer be applied to automotive coating

In automotive industries, a coating is applied on the automobile in order to both protect the substrate materials and improve the appearance.[3] Typically, automotive coating contains three layers: primer coat, base color coat and clear coat.[4] Typically, the thickness of clear coat is around 38µm to 103µm[4] and most of shallow scratches such as the coating defects, swirl marking marring, random deep marring and buffer marks occur in the clear coat. So if the clear coat can be made by shape memory polymer, most of the shallow scratches can be removed due to the good recovery ability of shape memory polymer with external heating.

2. Procedure

2.1 Materials

The diglycidyl ether of bisphenol A (EPON 826) was obtained from Hexion, the poly(propylene glycol)bis(2-aminopropyl) ether curing agent (Jeffamine D-230) was obtained from Huntsman and the neopentyl glycol diglycidyl ether (NGDE) obtained from Aldrich Chemistry.

2.2 Fabrication of Shape Memory Polymer

The solid EPON 826 was heated up to 70°C until all solids turn to liquid. The EPON 826, Jeffamine D-230 and NGDE were added into a clear glass jar with molar ratio 1.5:1:0.5. The mixture was shaken by hand for few seconds until the interface between EPON and other two liquid polymers disappeared.

The glass jar was placed in a vacuum oven at 70°C for 10 minutes. One piece of Teflon (101µm thickness) was cut into a half box bracket shape, as shown in Figure 1, and placed on a clear glass slide as a spacer. The polymer mixture was then poured on to the glass slide. The polymer was then casted into film by a film caster.

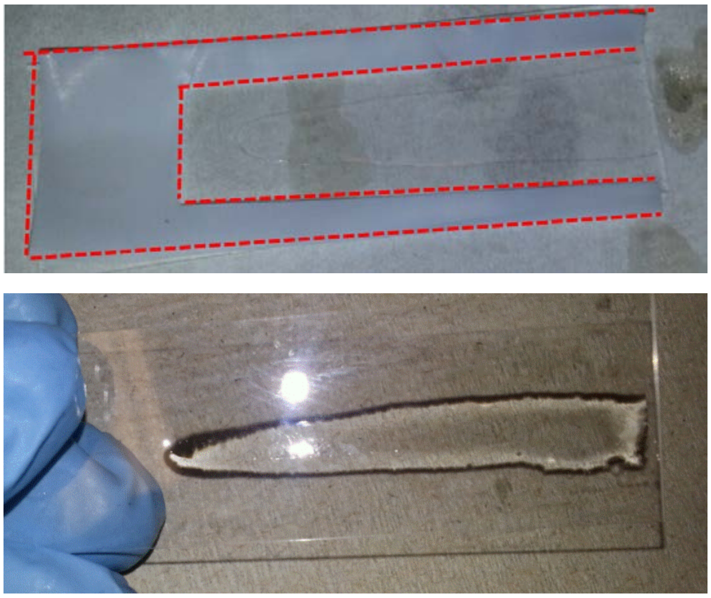

Figure 1: Shape memory polymer fabrication. (a) The polymer casted on glass slide. Note the red dash line indicates the shape of Teflon spacer. (b) Polymer after curing and post-curing.

The casted polymer with glass slide was put into a oven at 100°C and cured for 1.5 hours and then post-cured at 130°C for 1 hour.

2.3 Nano indentation test and thermal self-healing examination

The post-cured sample was marked and fixed on a sample platform of an nano indenter (Agilent Technologies Nano Indenter G200). Five indents were applied on the sample surface around the mark with a 500 mN force. The sample with indents were heated at 60°C for 15 minutes after the depth of each indents was measured (Zygo surface profiler). After the heating, the depth of indents were measured by Zygo surface profiler again to get the change of indents' depth. As there was no change for 60°C heating, the sample was heated at 70°C for 15 minutes and the depth of each indents was measured again.

3. Results and Discussion

3.1 Self-healing examination

The depths of indents after nano indentation were measured as 4.9µm, 5.6µm, 4.9µm, 5.5µm and 5.1µm. Figure 2 shows the sample measuring for one indent. As there were some noise during the indents scanned, the lowest point of each indent scanning image was selected as the bottom of indent.

An example of the Zygo surface maps and optical microscope images are shown in Figure 3. From Figure 3 (a) and (d), the indents are very obvious from both methods. After 15 minutes heating at 60°C, as shown in Figure 3 (b) and (e), the sample indents seems to be narrower but the depths of indents had no change. After 15 minutes heating at 70°C, all three indents are not visible, as shown in Figure 3 (c) and (f). The samples were scanning by Zygo again and there was no indents found on the sample surface. All indents were removed due to the thermal self-healing ability of epoxy shape memory polymer.

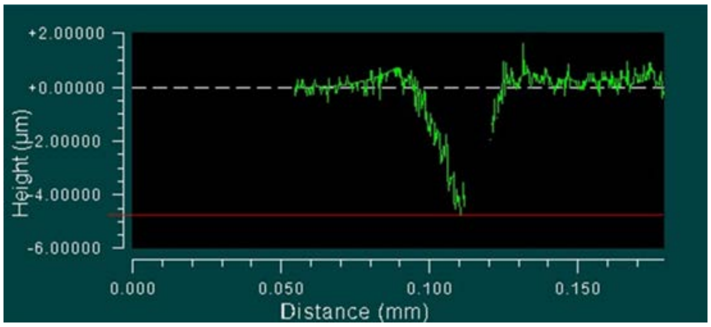

Figure 2: Example of indent depth measurement.

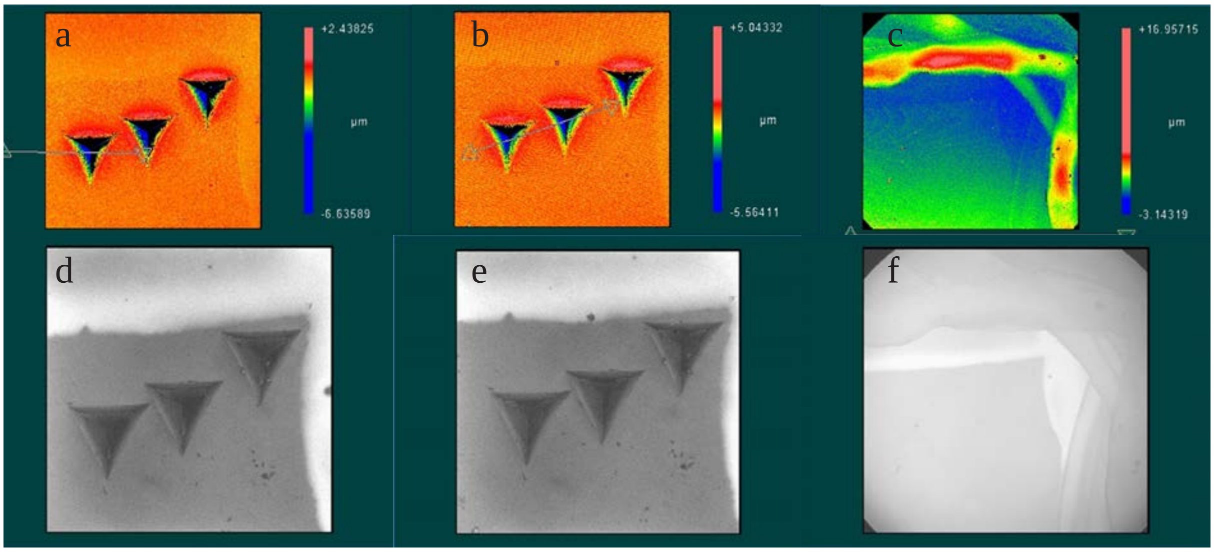

Figure 3: Surface mapping and optical microscope images for indents at room temperature, after 60°C and 70°C heating.

3.2 Nano Indentation data

The nano indentation testing data are shown in Figure 4. The indentation force was set to 50mN and the displacement was set to 10µm. The average hardness at max load obtained was 165±2MPa and the modulus at max load was 5.76±0.02GPa (as the Poisson's ratio of the polymer is unknown, the modulus is obtained by assuming the Possion's ratio as 0.4).

4. Conclusions

The self-healing of the shape memory polymer in thin film shape was examined. The five indents (depths from 4.9µm to 5.5µm) were not visible after 15 minutes heating at 70°C. The glass temperature T_g was measured to be around 70°C, which is consistent with Tao Xie's results.[2] The hardness of the thin film shape memory polymer was 165±2MPa and the modulus was 5.76±0.02GPa (assuming Possion's ratio 0.4).

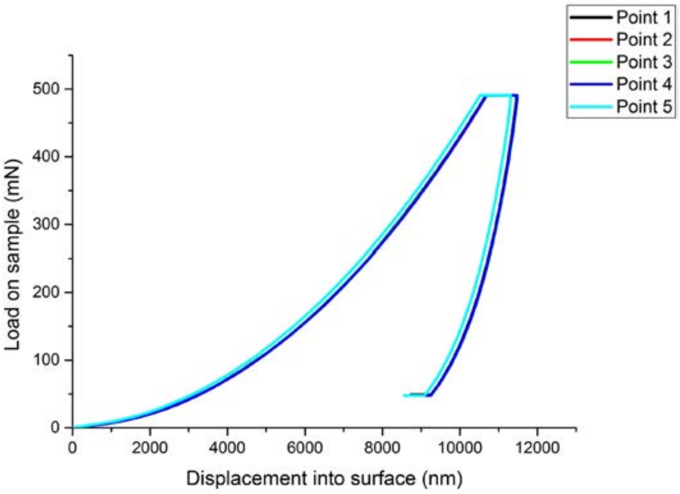

Figure 4: Loading force and displacement plot.

5. Future Work

In the automotive industries, the automobile is coated by the spray method. In the next step, the shape memory polymer should be tested whether it can be coated through spray method both in liquid or powdery shapes. Especially for the powdery shape, although the chemicals used are all liquids, but when the polymers are placed at room temperature for around 2 days after well mixing, the liquid polymer will turn to transparent solid. If the solid polymer can be ground into powder, then the polymer can be tested in spray method. But one issue is that, as the self-healing ability of this polymer is based on the cross link of chemical chains, we would like to know the relation between powder particle size and its self-healing ability and find the smallest possible size while maintaining self-healing ability maximum.

Acknowledgements

This paper is based on the papers of Tao Xie's team. This project is supported by Institute of Research for Technology Development of University of Kentucky and department of material engineering of University of Kentucky. The author would like to thank Professor Yang-Tse Cheng and Professor Douglass S. Kalika for guidance during experimentation.

Reference

1. Xie, T.; Rodak, D. E.; Rodgers, W. R. Shape Memory Epoxy Polymers. U.S. Patent 8618238 B2, Dec 1, 2013.

2. Xie, T.; Rousseau, I. A. Journal of Materials Chemistry **2010**, 3431-3441.

3. Schmidt, C.; Neuking, K.; Eggeler, G. Advanced Engineering Materials **2008**, 10(10), 922-927.

4. Toda, K.; Salazar, A.; Saito, K. Automotive Painting Technology, Springer Netherlands, 2013.

About the Author

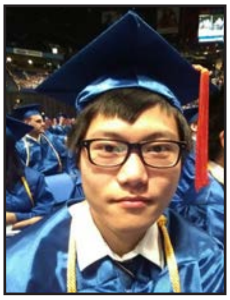

Ming Wang is a transfer student from China to University of Kentucky. He received his B.S. in Materials Science Engineering in University of Kentucky in this May. Before he transferred to University of Kentucky, his major in Qingdao University of Science and Technology (China) was Polymer Science Engineering.

Contact at: wangming1992@hotmail.com

Synthesis and Toxicity of Lipid-Coated-Titanium Oxide Nanoparticles

Louis R. Hollingsworth IV[1,2], Joseph H. Conduff[1], Connor J. Balzer[1], Sieu K. Tran[2], Waqas Hamid[2], and Lauren E. Rakes[2]

[1]Virginia Polytechnic Institute and State University, Department of Chemistry, 900 West Campus Drive, 480 Davidson Hall, Blacksburg, VA 24061

[2]Virginia Polytechnic Institute and State University, Department of Biological Sciences, Derring Hall Room 2125, 1405 Perry Street, Blacksburg, VA 24061

Abstract

Nanoparticles have a broad range of applications in novel materials and consumer products. Due to the unique properties of nanoscale materials, the toxic effects of various nanoparticles are largely unknown. Surface modifications to nanoparticles, such as membrane or lipid coatings, may reduce immunogenicity and environmental toxicity, but these effects remain largely uncharacterized. The synthesis of lipid-coated titanium oxide nanoparticles was optimized and toxicity was evaluated. Thermogravimetric analysis showed that 5 µM of tricarboxylic amphiphile sufficiently generated uniformly coated nanoparticles. Toxicity studies on *Zea mays* (corn) revealed that uncoated titanium oxide nanoparticles exhibited phytotoxicity, while lipid-coated nanoparticles had effects resembling deionized water. Scanning electron microscopy displayed visual evidence of nanoparticle absorption into the corn seedlings in experimental groups.

Keywords: Nanoparticle, titanium, oxide, titania, tricarboxylic, amphiphile, lipid, coating, toxicity, phytotoxicity, nanotechnology, scanning, electron, microscopy

1. Introduction

The development of nanotechnology is rapidly increasing, with an enormous number of applications in material science, consumer products, medical diagnosis and treatment, and drug delivery vehicles.[1] Currently, there are more than 1600 nanotechnology products available for consumer use logged in the Nanotechnology Consumer Products Inventory (CPI).[2] Research and commercial use necessitate disposal, thus, nanoparticles will inevitably be released into the environment. Questions arise as to the safety of such nanoparticles, especially concerning their effects on plant life consumed by humans.[3] Further, even less is known in regards to the effects of functionalized nanoparticles; functionalization of nanoparticles for specific commercial uses or to reduce environmental impact may be induced by surface modification. Thus, this project aims to test the phytotoxicity of coated nanoparticles.

1.1 Coating

Metal oxide (Iron oxide, titanium oxide, etc.) nanoparticles have nearly unlimited potential for research applications.[1] Applications of these nanoparticles range from solar cells to MRI contrast agents and drug delivery vehicles.[3,4] Challenges present themselves in developing reliable methods to uniformly coat metal oxide nanoparticles; the coating offers the advantage of controlling the spacing between the solid particle and the pliable outside surface. Compounds with a tricarboxylic "head" group (Figure 1) can attach to iron oxide nanoparticles.[5] In this manuscript we demonstrate that the same head group, when conjugated to a long-chain lipid (4-(2-Carboxyethyl)-4-(3-octadecyloxycarbonylamino) heptanedioic acid (3CCb18), Figure 1), can attach to titanium oxide nanoparticles (TiNPs). These TiNPs can be suspended in aqueous solution and subsequently used for further experimentation.

1.2 Toxicity

Due to their unique properties such as enhanced catalysis, lowered melting point, and increased conductivity, nanoparticles like TiNPs have potentially harmful effects to many organisms in the global ecosystem and ultimately pose a threat to humans.[1,3] Preliminary studies on the impact of nanoparticles on plants have shown both positive and negative effects. In one study, nano-titanium oxide (TiO_2) promoted the growth of spinach; however, the majority of phytotoxicity studies identified solid metal nanoparticles as toxic.[6] Nano-aluminum oxide inhibits root elongation in corn, cucumber, soybean, cabbage, and carrots, while nano-zinc oxide terminates the growth of various plant species.[7,8]

Although there have been many toxicity experiments conducted with uncoated nanoparticles, there has been little evaluation of functionalized or coated nanoparticles. Studies on the toxicity of nanoparticles and the effects of various coatings will elucidate the dangers of this technology and provide guidance for disposal and efficacious drug design. Phytotoxicity experiments aim to determine the effect of 3CCb18 coated (Figure 2) and uncoated TiNPs on the root development, seed germination, and overall germination index of *Zea mays* (corn). *Z. mays* was chosen based on availability, worldwide consumption, and previously conducted toxicity experiments.[7-9] Toxicity was quantified using the germination index, a simple metric reported in nanotoxicology text that takes into account both total germination and early seedling development.[9]

$$\text{Germination Index} = \frac{\textit{Experimental seeds germinated}}{\textit{Control seeds germinated}} * \frac{\textit{Experimental average root length}}{\textit{Control average root length}} * 100 \quad (1)$$

2. Methods

2.1 Nanoparticle Coating

Optimum modification of the TiO_2 surface was achieved by heating TiNPs (Sigma, 21 nm diameter) in a mixture of chloroform ($CHCl_3$), toluene (PhMe), 3CCb18, and triethylamine. 3CCb18 (5 μM, previously synthesized in lab) was stirred in a 250-mL round bottom flask with PhMe/$CHCl_3$ 1:1 v:v (40 mL). Triethylamine (9 μL) was added to the mixture to neutralize the carboxyls. Next, a suspension of aqueous TiNPs (0.3 mL) was added dropwise, and the mixture was stirred at 80 °C for 24 h. The final mixture had a milky white color with noticeable precipitate at the bottom of the round bottom flask. Isolation of suspended nanoparticles was best achieved by rotary evaporation.

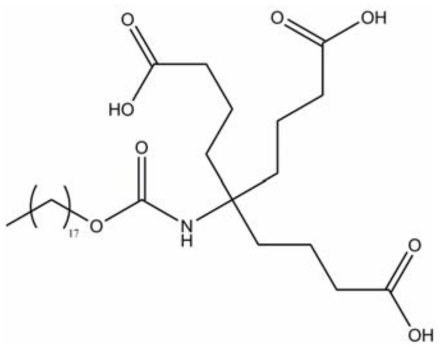

Figure 1: 3CCb18 unit for TiNP surface modification.

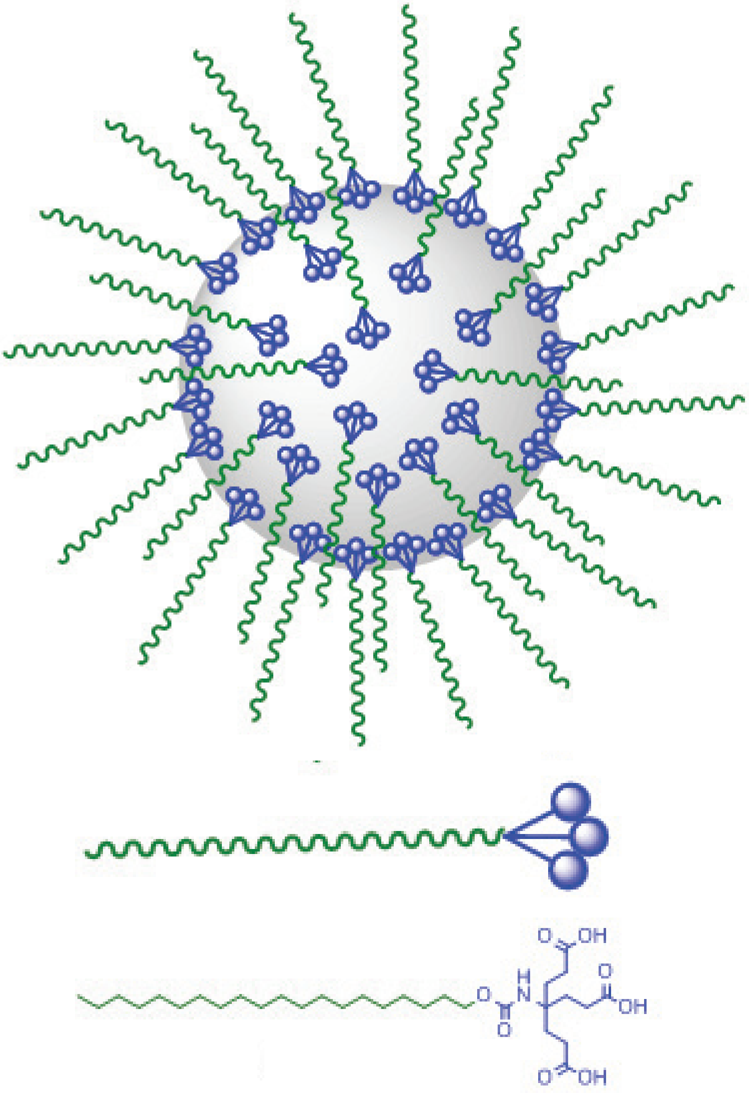

Figure 2: Graphic of 3CCb18-coated-TiNP.

The solvent was removed from the round bottom flask with rotary evaporation, and the nanoparticles were transferred to a small vial and dried under high vacuum for 24 h to give a cream-colored powder.

2.2 Thermogravimetric Analysis

The surface modification of the TiNPs was analyzed with thermogravimetric analysis (TGA) from 0 to 600 °C at 10 °C/min. Samples of TiNP powder, 3CCb18 lipid, and 3CCb18-coated-TiNPs (5-10 mg) were analyzed with a TA Instruments TGA Q500.

2.3 Phytotoxicity

To evaluate toxicity, the growth media of germinating *Z. mays* seeds was varied between three groups: coated and uncoated TiNPs as well as a DI water control. A modified procedure as published previously was followed.[9] Prior to conducting experimentation, nanoparticle solutions were prepared by adding TiNPs (0.04 g) to deionized (DI) water (20 mL) and sonicating for 1 h. Afterwards, the solutions were diluted further to 100 µg/mL by adding DI water (380 mL) and stirring thoroughly. The viability of the *Z. mays* seeds (Hirt's Gardens, Medina Ohio) was verified by suspending the seeds in DI water and selecting the seeds that settled to the bottom. The seeds were then soaked in 10% sodium hypochlorite solution, which acts as a surface sterilizing agent; after 10 min they were rinsed thoroughly in DI water. After rinsing, the seeds were sorted into three groups of thirty, which would be used for each nanoparticle solution. The three solutions evaluated were DI water (control), 3CCb18-coated-TiNPs, and uncoated TiNPs. Each group consisting of thirty seeds was then placed in solution and stirred for 2 h. Subsequently, nine petri dishes were prepared with Whatman filter and soaked with the corresponding nanoparticle suspension (5 mL) or DI water (5 mL). The seeds were drained, patted dry, and subsequently transferred to the petri dishes containing the filter paper, which were then sealed with parafilm and placed in a dark environment for 4 d. Root length and total germination measurements were taken, and germination index was calculated (Eq. 1).

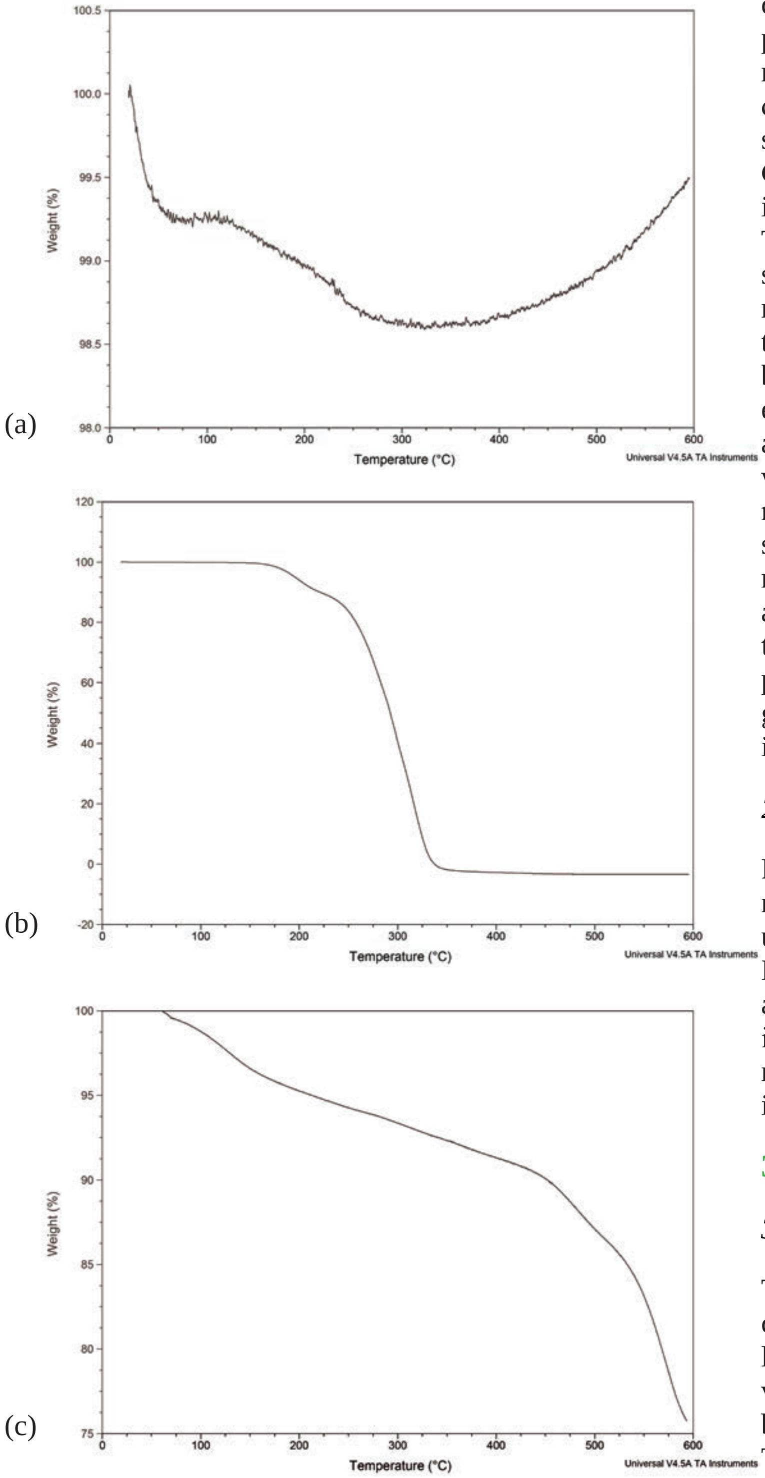

Figure 3: TGA analysis of various TiNPs. (a) Unmodified TiNPs show no significant weight loss. (b) 3CCb18 lipid-coated-TiNPs show 100% weight loss by 350 °C. (c) 3CCb18-coated-TiNPs show 25% weight loss by the end of the experiment, implying the surface of the nanoparticles was modified.

2.4 Scanning Electron Microscopy

Following procedure *2.3*, several samples were taken at random from each experimental group (DI water control, uncoated TiNP, coated TiNP) and analyzed with Scanning Electron Microscopy (SEM). *Z. mays* seeds were sliced open and sputter coated in Au/Pd 60:40. Samples were loaded into a LEO (Zeiss) 1550 field-emission SEM and electron micrographs were obtained. Visual analysis was used to identify TiNPs embedded in the *Z. mays* seedlings.

3. Results and Discussion

3.1 Coating and Thermogravimetric Analysis

The TGA of TiNPs and 3CCb18 lipid provide controls for comparison with coated TiNPs. TiNPs do not vaporize and lose zero weight percent (Figure 3a), whereas 3CCb18 lipid vaporizes completely at 350 °C and loses 100% of its weight by the end of the experiment (Figure 3b). With these control TGA experiments, it may be inferred that any lipid conjugated to a TiNP should vaporize by 350 °C, leaving uncoated TiNPs for the remainder of the experiment. Further TGA experiments were then conducted on coated TiNPs that utilized 5 µM of 3CCb18 during synthesis (Figure 3c); the loss of 7% of the initial mass and retention of 93% of the input weight at 350 °C shows that lipid molecules successfully coated the TiNPs.

Table 1: Germination rates, average root lengths of the seeds that germinated from each experimental group, and calculated germination index (Eq. 1) for each experimental group.

Group	Seeds Germinated (of 30)	Average Root Length of Germinated Seeds (cm)	Germination Index
Control	27	2.3 ± 1.5	100
TiNPs	23	1.7 ± 1.5	63
Coated TiNPs	21	2.9 ± 1.1	96

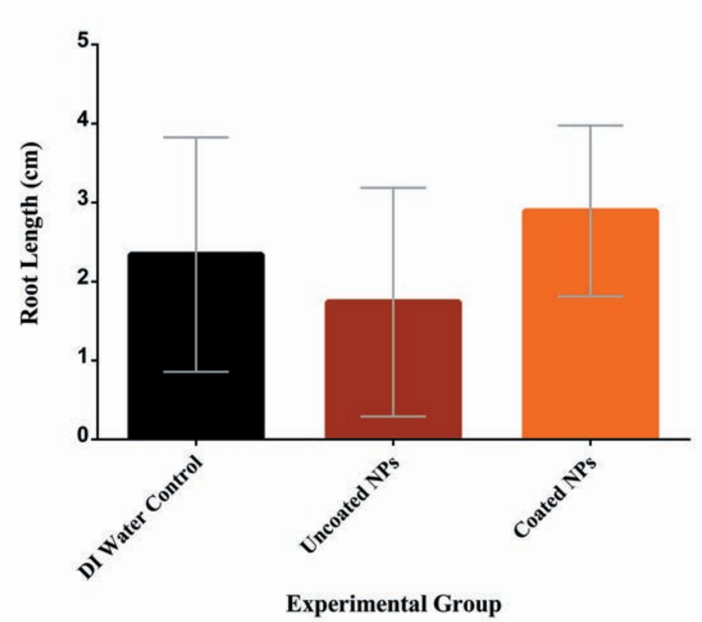

Figure 4: Average root length distribution of DI water, uncoated nanoparticle, and coated nanoparticle-treated experimental groups. Standard errors are displayed with error bars.

3.2 Phytotoxicity Assay

$p < 0.025$ using paired single factor ANOVA analysis. Uncoated nanoparticles had a germination index (Eq. 1) of 63.3 compared to 100 for the DI water control; hence, uncoated TiNPs have detrimental effects on *Z. mays* during early development. According to the literature, concentrations of 100 µg/mL of various nanoparticles begin to show negative effects on root growth and overall germination on different varieties of seeds.[8] The TiO_2 data presents similar results: an uncoated nanoparticle concentration of 100 µg/mL displayed prominent phytotoxicity. Both coated and uncoated nanoparticles showed a reduced percentage of seeds germinated compared to the control; yet, the coated nanoparticles' germination index was very close to 100, comparable to the control's growth rate. These results suggest that coated nanoparticles had little or no phytotoxic effects on seed germination, whereas uncoated nanoparticles exhibited prominent phytotoxicity. Additionally, average root growth was enhanced in coated nanoparticles (Figure 4); this positive effect may be explained by the lipid coating. This coating may have helped hydrophobic molecules absorb more effectively into corn, increasing nutrient uptake and providing for better growth. Alternatively, the lipid may have been hydrolyzed and removed from the coating on the TiNPs, creating a fatty alcohol that provided the *Z. mays* seeds with a source of energy and a component utilized in cell membranes. Experimental results are summarized in Table 1.

3.3 Microscopy

SEM micrographs show the presence of TiNPs in both coated and uncoated experimental groups, suggesting that their uptake contributed to experimental results (Figures 5a, 5b, and 5c). Elemental analysis was conducted in tandem to SEM spectroscopy to confirm the presence of titanium (data not shown)

4. Conclusions

The TGA data suggest that there is a strong interaction between the tricarboxylic acid head group and the TiO_2 core. This shows that the coating procedure and tricarboxylic head group can be used to build novel uniformly coated metal oxide nanoparticles, and a tricarboxylic-acid head group will associate strongly with TiO_2.

Phytotoxicity evaluation used *Z. mays*, a worldwide staple of food consumption. SEM showed that *Z. mays* uptakes nanoparticles (Figures 5b and 5c). Alarmingly, if the seeds carry these TiNPs to their gametes, they may pass into the human body if ingested. Uncoated TiNPs hindered root growth at a concentration of 100 µg/mL, while a solution of 3CCb18-coated-TiNPs at the same concentration promoted root growth when compare to a DI water control (Table 1 and Figure 4). Collectively, these results show that precautions must be taken to prevent the release of TiNPs into the environment. Further analysis of environmental retention must be conducted in order to better assess the direct implications of nanoparticles on the environmental health and human safety.

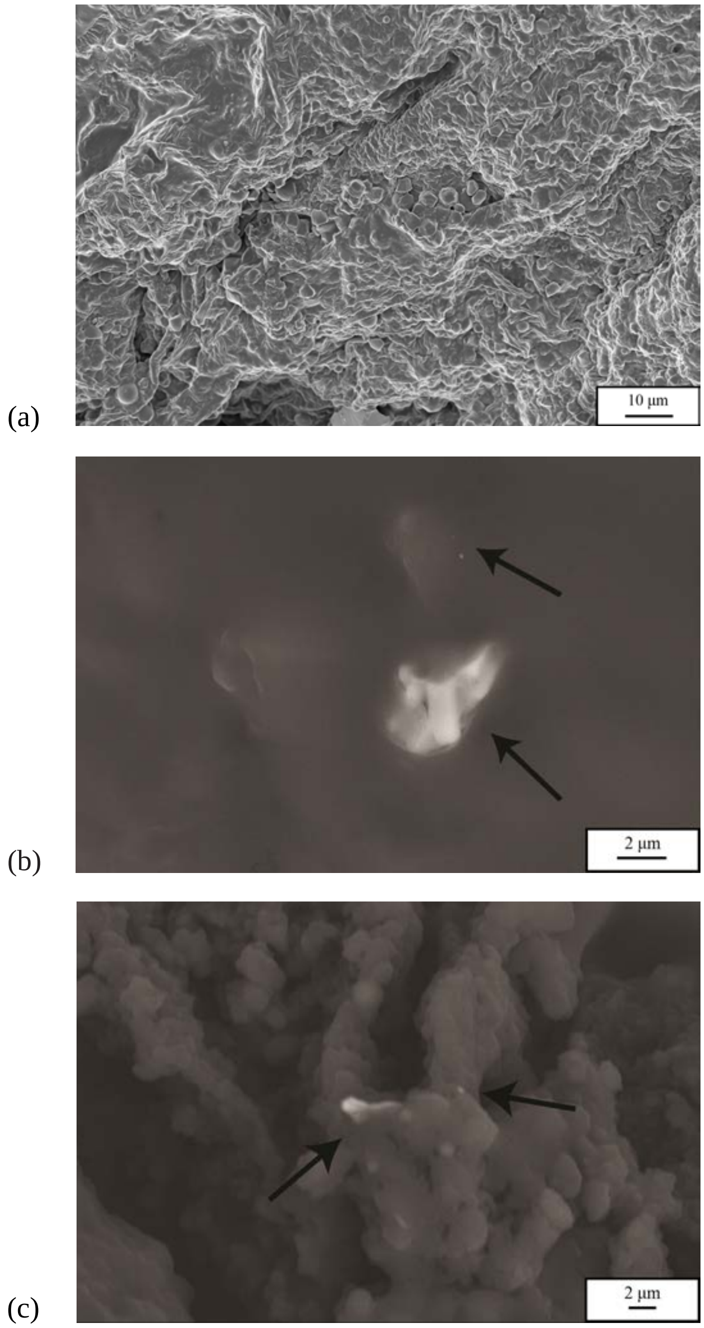

Figure 5: SEM micrographs displaying cross sections of the corn seedlings from the experimental groups. Areas of interest are highlighted with arrows. (a) Control seedlings with no nanoparticles visible in the root's wide-field cross section. (b) Uncoated TiNP experimental group showing a large aggregate of TiNPs present in the seed tissue. (c) Coated TiNP experimental group showing a small aggregate of TiNPs present in the seedlings.

5. Future Work

This paper details initial synthesis and toxicity data for a lipid-coated-nanoparticle; more experiments are necessary to elucidate the long-term exposure effects on plant life and mechanism of toxicity. Additionally, we aim to use the knowledge gained from this study to ultimately create and optimize a minimally toxic nanoparticle for drug delivery applications.

5.1 Nanoparticle Synthesis

Surface modifications of nanoparticles enable unique properties for functionalization. We will synthesize and conjugate polymer linker molecules consisting of a polyethylene glycol spacer and a cholestanol anchor to the solid metal nanoparticle. Hydrophobic interactions with the cholestanol anchor will enable the spontaneous formation of a phospholipid bilayer around the nanoparticle, allowing the incorporation of both hydrophobic and hydrophilic compounds for drug delivery purposes. Further tests on the uniformity of coatings are also necessary before proceeding to the encapsulation of compounds.

5.2 Biological Evaluation

Ongoing biological evaluation is necessary to assess the environmental and human impacts of nanoscale devices. Several different coatings on many types of nanoparticles should be assessed with a variety of concentrations of nanoparticles. Further phytotoxicity and cytotoxicity studies using a broad array of plant and animal models for a statistically representative conclusion on nanoparticle toxicity. Further understanding of toxicity mechanisms will help in designing more effective nanoparticles for commercial use and in shaping public policy regarding nanoparticles utilized in consumer products.

Acknowledgements

This manuscript is based on results obtained through a honors biology project in conjunction with chemistry undergraduate research. The authors would like to express our gratitude to our advisor, Professor Richard D. Gandour, for his guidance and resources throughout the project. We thank Professor Amanda J. Morris and Mr. Andrew Haring for providing TiO_2 nanoparticles. SEM work was conducted at the Nanoscale Characterization and Fabrication Lab (NCFL) at Virginia Tech; the authors would also like to acknowledge Mr. Stephen McCartney for the use of the SEM and his flexibility, and the department of biology for SEM funding.

References

1. Nel, A.; Xia, T.; Mädler, L.; Li, N. Science **2006**, 311 (5761), 622-627.

2. Matthews, J. N. A. Physics Today **2014**, 67.

3. Srivastava, V.; Gusain, D.; Sharma, Y. C. Industrial and Engineering Chemistry Research **2015**, 54 (24), 6209–6233.

4. You, J.; Chen, C.; Dou, L.; Murase, S.; Duan, H.; Hawks, S. A.; Xu, T.; Son, H. J.; Yu, L.; Li, G.; Yang, Y. Advanced Materials **2012**, 24 (38), 5267-5272.

5. Xie, Q.; Williams, A. A.; Gandour, R. D.; Esker, A. R. Polymer Preprints **2007**, 48(2), 966–967.

6. Hong, F.; Zhou, J.; Liu, C.; Yang, F.; Wu, C.; Zheng, L.; Yang, P. Biological Trace Element Research **2005**, 105 269-79.

7. Yang, L.; Watts, D. J. Toxicology Letters **2005**, 158 (2), 122-32.

8. Lin, D.; Xing, B. Environmental Pollution **2007**, 150 (2), 243-250.

9. Kumari, M.; Ernest, V.; Mukherjee, A.; Chandrasekaran, N., In Vivo Nanotoxicity Assays in Plant Models. In Nanotoxicity, Reineke, J., Ed. Humana Press: 2012; Vol. 926, pp 399-410.

About the Authors

Louis Hollingsworth is a junior obtaining degrees in chemical engineering, biochemistry, and chemistry. He has extensive research experience, including internships at a bioengineering laboratory at George Washington University (2013), a structural biology laboratory at the National Institutes of Health (2014), and a biomedical laboratory at Harvard University (2015). Additionally, Bobby currently conducts chemical synthesis with Professor Richard Gandour in the Department of Chemistry at Virginia Tech and is a member of Virginia Tech's chemical engineering design team, Chem-e-Car. He intends to pursue a Ph.D. in a field related to cancer drug design at a university at the forefront of translational medicine. Contact at: bobbyh11@vt.edu

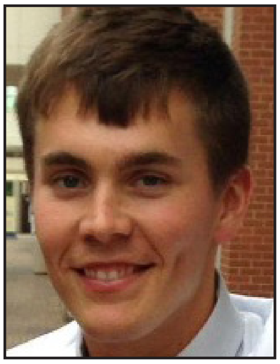

Joseph Conduff graduated from Virginia Tech in 2014 with a B.S. in Biochemistry. He worked in the laboratory of Dr. Richard Gandour for five semesters during his undergraduate career, conducting research on chemical synthesis and the surface modification of nanoparticles. Joey is currently a first year medical student at Virginia Commonwealth University School of Medicine.

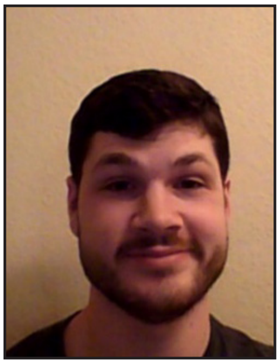

In addition to his contributions to the Gandour lab at Virginia Tech, Connor Balzer worked for the International Petroleum Products and Additives Company (IPAC) Technical Center developing petroleum products as well as in-house petroleum specification tests. He graduated summa cum laude from Virginia Tech in May of 2014 with an honors degree in Biochemistry and a minor in Chemistry. He is currently attending graduate school at the University of Oregon working on a Ph.D. in their Chemistry and Biochemistry program. His research interests include drug development and protein evolution.

Sieu Tran is a Junior at Virginia Tech majoring in Mathematics (Applied Computational Option) and Biological Sciences (Microbiology/Immunology Option). He hopes to earn an M.D.-Ph.D. after his undergraduate education to become a physician-scientist. His current research lies in Integro-Differential Algebra and Its Discrete Version (Mathematics), Language, Violence and Nonviolence in Clinical Environment (Linguistics), Mucosal Immunology and Gastrointestinal Pathophysiology Laboratory (Immunology), and Examination of the Functional Significance of Influenza Virus Morphology and Mechanisms of Influenza Virus Assembly and Budding (Virology). Sieu studied abroad at the University of Kent in Canterbury, England.

Waqas Hamid is currently a third year undergraduate student at Virginia Tech majoring in biochemistry through the College of Agriculture and Life Sciences. He is a member of the PHI SIGMA Biological Sciences Honor Society, VT-AMP, and the Biochemistry Club as well as a MAOP undergraduate scholar. Waqas is currently conducting undergraduate research at the University's Plant, Pathology, and Physiology Department under the supervision of Dr. Guillaume Pilot. He is currently investigating the relationship between the presence of amino acids and the stress response released by plants.

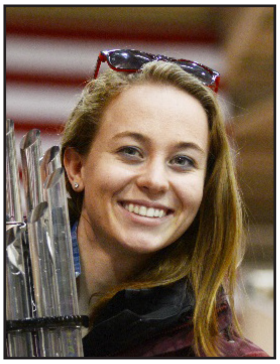

Lauren Rakes is a sophomore from Blacksburg, Virginia currently pursuing two degrees in Biology and Psychology. In addition to her academics, she works as a Hokie Sports photographer for Virginia Tech Athletics. In her spare time, Lauren regularly volunteers as a track coach for Blacksburg Middle School, and is an official partner of the Special Olympics. After college, Lauren wishes to go to medical school and pursue pediatrics.

Bacterial Cellulose as a Potential Bone Graft

Kennedi K. Lowman[1,2,3]

[1]Albany State University, [2]Virginia Polytechnic Institute and State University, [3]Bioengineering/ Bioinformatics Summer Institute- Virginia Polytechnic Institute and State University School of Biomedical Engineering and Sciences ICTAS Stanger St Blacksburg, VA 24061

Abstract

Each year tissue engineering costs the United States $2 million dollars. Bacterial Cellulose (BC), a hydrogel with a fine fiber network, is produced by the bacterium *Acetobacter xylinum* that can be used as a protective coating. In contrast to other polymers, BC possesses high tensile strength, high water holding capabilities, and high mechanical properties. The purpose of the current study is to determine if individual fibers of BC can be functionalized with calcium by applying an electric field. BC was grown and calcium was deposited simultaneously using Corn Steep Liquor (CSL) media, with the addition of fructose, in channels 4 cm long x 5 mm wide x 2.5 mm deep. The channels contained platinum electrodes supplying an electric field of 3 to 7.5 volts for 72 hours in the presence of $CaCl_2$. BC pellicles formed and were then examined using the Environmental Scanning Electron Microscope (ESEM). Energy-Dispersive X-ray Spectroscopy (EDS) was also used to determine the composition in each sample. Calcium was found deposited on the BC fibers at 5.5 volts. Lower voltages, such as 4.0 volts, resulted in no calcium deposition on the fibers. The presence of Carboxymethyl Cellulose (CMC) is critical for the calcium deposition. Calcium deposition will occur at 5.5 volts suggesting there may be a specific electric field requirement for calcium deposition on BC.

Keywords: hydroxyapatite, bacterial cellulose, tissue engineering, bone grafts

1. Introduction

Tissue engineering research is a growing field where researchers experiment with more efficient and inexpensive ways to create scaffolds. These scaffolds will repair or replace whole tissues quicker than previous methods. Researchers are trying to create tissue scaffolds where cell proliferation occurs in the microstructure like it would in the human body.[1] Manufacturing challenges inhibit clinical trials from taking place on existing scaffold fabrication techniques.[2]

Worldwide there are over 2 million bone grafts performed every year. These procedures cost the US billions of dollars every year. There are three types of bone grafts: autografts, allografts, and synthetic grafts;[3] autografts and allografts are most common. Autografts harvest autologous bone from the iliac crest where a long surgical procedure is usually accompanied by residual pain. Typical complications include blood loss, nerve injury, infection, hernia fracture, cosmetic defects, and occasional chronic pain at the donor site.[4] Between autografts and allografts, allografts are the most frequently chosen bone substitutes because of the availability of tissue and its ability to be customized through manufacturing. These synthetic bone grafts should be biocompatible, show minimal fibrotic reaction, undergo remodeling, and support new bone formation. Additionally, mechanically synthetic bone substitutes should have similar strength to the bone it is replacing.[4] In our experiment, we are creating the initial steps for fabricating a synthetic graft by using BC and calcium. The presence of calcium is vital to repair fractures in the bone and initiate bone growth.[3] This type of research is being conducted to create safer, more efficient bone substitutes. By creating a more efficient product to replace bone grafts millions of dollars would be saved worldwide.[3, 5]

BC is a primary metabolite that is mainly used as a protective coating. Cellulose is a biopolymer that is represented as a microbial extracellular polymer. Bacteria forms subfibrils, which are the thinnest naturally-occurring fibers.[6] The subfibrils are crystallized into microfibrils, which form bundles that turn into ribbons. The ribbons accumulate into a fine fiber network forming a mat called a pellicle during static conditions (S-BC). Static conditions refer to the cells at the oxygen-rich liquid/air interface.[6,7] The pellicles form parallel but disorganized planes. S-BC fibrils are extended and piled on top of one another in a more criss-cross pattern.[6]

The strain of bacteria cellulose used most commonly is *Acetobacter xylinum*. *A. xylinum* is a model microorganism for cellulose studies. It is a gram-negative, acetic acid bacterium.[6] *A. xylinum* grows rapidly and can be maintained under controlled environments in a laboratory setting.

Bone is a composite of collagen and hydroxyapatite. Hydroxyapatite is a chemical composite of natural bone with the chemical formula $Ca_{10}(PO_4)_6(OH)_2$; this ideally mimics synthetic bone structures.[3] Previous experiments created calcium-deficient hydroxyapatite by immersing the BC pellicle into a calcium solution followed by a phosphate solution. Our approach uses electric fields to control the fiber orientation and to deposit calcium throughout the forming structure. We are studying the effects of electric fields on BC growth and calcium deposition using CSL media with the addition of $CaCl_2$.

The purpose of this study is to coat individual BC fibers with calcium by applying an electric field to the BC pellicle. The difference between this study and previous studies is that we are trying to apply calcium to each layer of BC as it grows whereas previous studies dipped the pellicle in a calcium solution after it had already formed. Electrolysis is used as a result to coat the BC fibers with calcium. With the right parameters, calcium can be deposited on every fiber in the BC pellicle.

2. Materials & Methods

2.1 Preparation of Media

Corn steep liquor (CSL) media was used during this experiment with the addition of fructose as a culture media. *A. xylinum* bacteria were grown for this experiment in a flask in the incubator for 3 days at 27 °C in the culture media.

2.2 Fabrication of Micro-growth Channels

Polydimethylsiloxane (PDMS) liquid was poured over the stamp of a 4 cm long x 5 mm wide x 2.5 mm deep channel. The stamp and PDMS were set on a hot plate allowing the PDMS to harden for 30 minutes. After taking the mold off the stamp, two holes were punched into each channel, one at each end. The mold was washed with soap, ethanol, and DI water and dried with pressurized air. It was then placed in plasma cleaner with two glass slides for a total of four minutes. The glass slides and mold were bonded together with channels facing down towards the slide.

2.3 Cellulose Production and Deposition

A 1000uL pipette tip was inserted into one side of the channel and a pipette tip with a mixture of 20 mL media, 2 mL of $CaCl_2$, and 1 mL of bacteria was inserted in the other end to fill the channel up. Platinum wire was fed through each tip and connected to a DC supply with a voltage of 3.5, 5.5, 6.0, or 7.0 to apply electric fields to the channels. The experiments were left to run for 72 hours at the set voltage.

2.4 Sample Preparation for ESEM

The PDMS was peeled off the glass slides and the pellicles were pulled out of the channels with tweezers and placed in test tubes of DI water. The test tubes were placed in the sonicator for an hour at 60 °C. Afterwards, new DI water replaced the old and the test tubes were immersed into liquid nitrogen. Immediately after immersing in liquid nitrogen, the test tubes were placed in a jar and connected to a freeze dryer for two days. After the pellicles were freeze dried, they were cut and mounted onto SEM specimen holders with the surface and cross-sectional pieces facing upwards. They were placed in a sputterer and coated with palladium for 45 seconds.

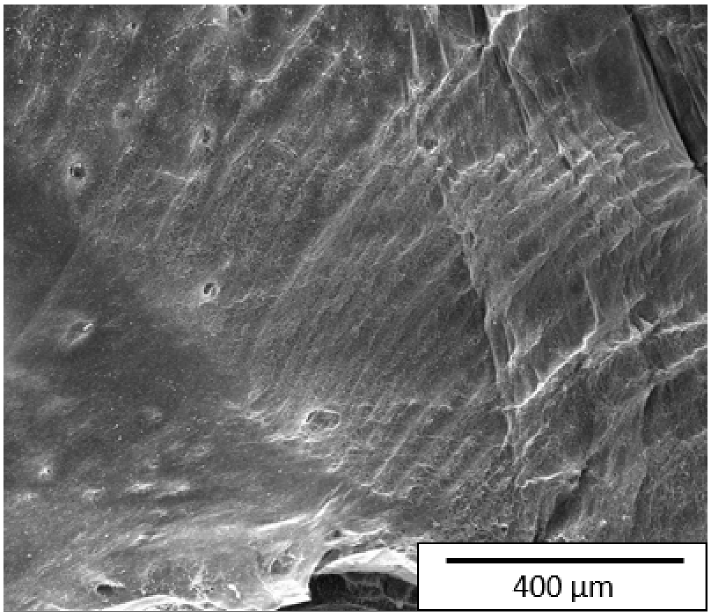

Figure 1: ESEM images of the surface of a pellicle at a voltage of 5.5.

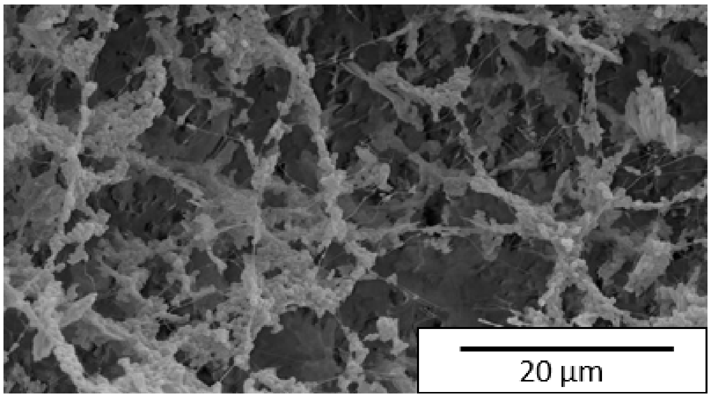

Figure 2: Wire deposition near the 5.5V electrode hole.

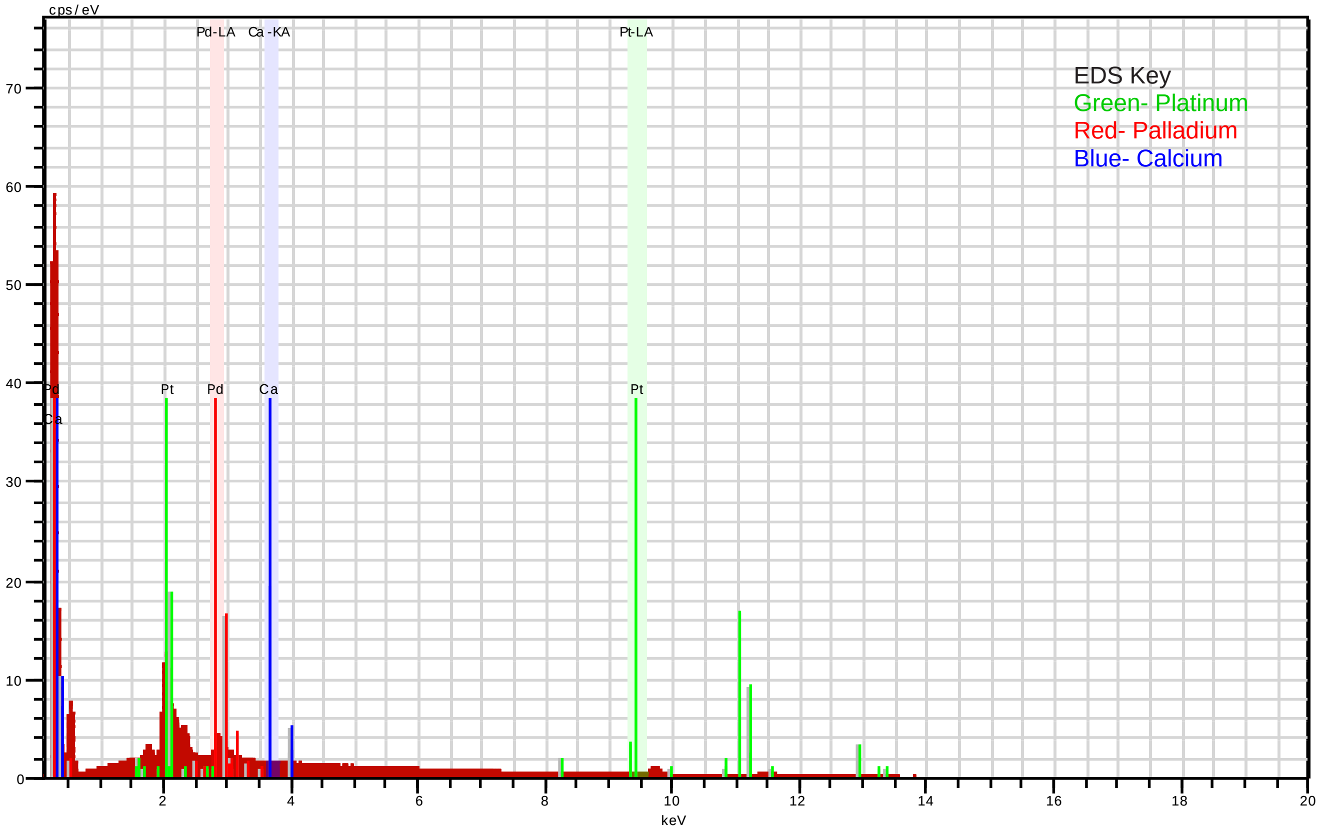

Figure 3: Materials deposited in the 5.5V sample.

3. Results

The ESEM was used to observe the surface and cross section of the pellicle pieces for traces of calcium on the BC fibers. Observing the overall surface of the pellicles revealed no calcium on the fibers. However, the fibers near the holes, where the electrodes were placed, calcium was observed at 5.5V.

EDS analysis was carried out for the 5.5V sample and small amounts of calcium along with palladium from the coating, and platinum were detected in the sample. After observing the electrode hole during our first visit to the ESEM, we took a closer look at the electrode holes during the next set of trials to observe any material deposition.

We experimented with some of our trials and added Carboxymethyl Cellulose (CMC) to the solution. Under the ESEM, the BC pellicles showed crystal formation on the fibers

Through EDS, we found a greater amount of materials deposited in our sample such as calcium, palladium, oxygen, carbon and potassium. Potassium was a material in our media. Carbon and oxygen are BC pellicle growth components.

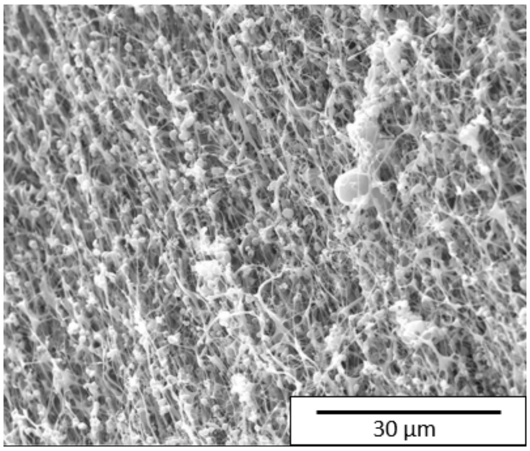

Figure 4: Materials deposited on the BC fibers at 5.5 V.

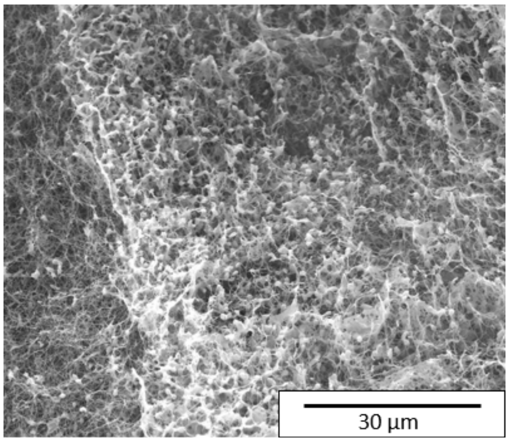

Figure 5: At closer observation EDS reveals calcium on the BC fibers.

4. Discussion

At low voltages, fiber alignment occurs. BC grows at 3.5V to 5.5V but would not grow at 6.0V or 7.0V. When exposed to higher electric fields, the bacteria halts its production of cellulose and it's possible that at these electric fields it may even kill the bacteria. The first couple of trials did not show calcium deposited on the BC fibers but the EDS analysis picked up palladium and platinum. Palladium was used to coat our samples while platinum electrodes were used to apply an electric field. Since BC is made up of carbon and oxygen the EDS showed high values of these materials.

We experimented with some of our trials and added CMC to the solution and received positive results. Previously, CMC was used to initiate a calcium-deficient hydroxyapatite.[3] The CMC physical absorption onto cellulose is thought to occur due to a co-crystallization process but the mechanism is still not well understood. Observing the BC pellicles under the ESEM showed particles or crystals on our fibers as seen in Figure 3. In the experiments without CMC, we found 0.70 atomic percent of calcium in our pellicle, whereas when we added CMC, our atomic percent of calcium increased to 1.23. Many trials were not conducted using CMC until we realized that CMC was helpful for another group's experiments.[3] The experiments without CMC did not show calcium on the fibers when viewed under the ESEM. Also, increasing the amount of calcium and molarity in some later trials the fibers remained to show no calcium deposition. Although we did not get a high quantity of calcium onto each fiber we were able to deposit calcium by applying a low voltage electric field to each channel.

5. Conclusion

Calcium was successfully deposited onto BC fibers at 5.5 V. However, deposition was only seen locally on the BC and not throughout the entire pellicle. When CMC, a negative polymer, was added to the media, more deposition was seen.

In the future, we could try and find some calcium-coated electrodes. Also, mixing CMC and a phosphorus solution, such as phosphate buffered saline (PBS), into the media may help deposit phosphorus and calcium on each fiber of the pellicle to form hydroxyapatite. More experiments on finding the right channel size to grow the BC in is an important factor for future research since a lot of our trials' solution did not form pellicles even after 72 hours.

Acknowledgements

This work was performed at Virginia Tech by a student in the Bioengineering/ Bioinformatics Summer Institute (BBSI) under the supervision of Dr. Rafael Davalos. The project was funded by the NIH/NSF Award Number 0609225. The author would like to thank her graduate mentor Andrea Rojas.

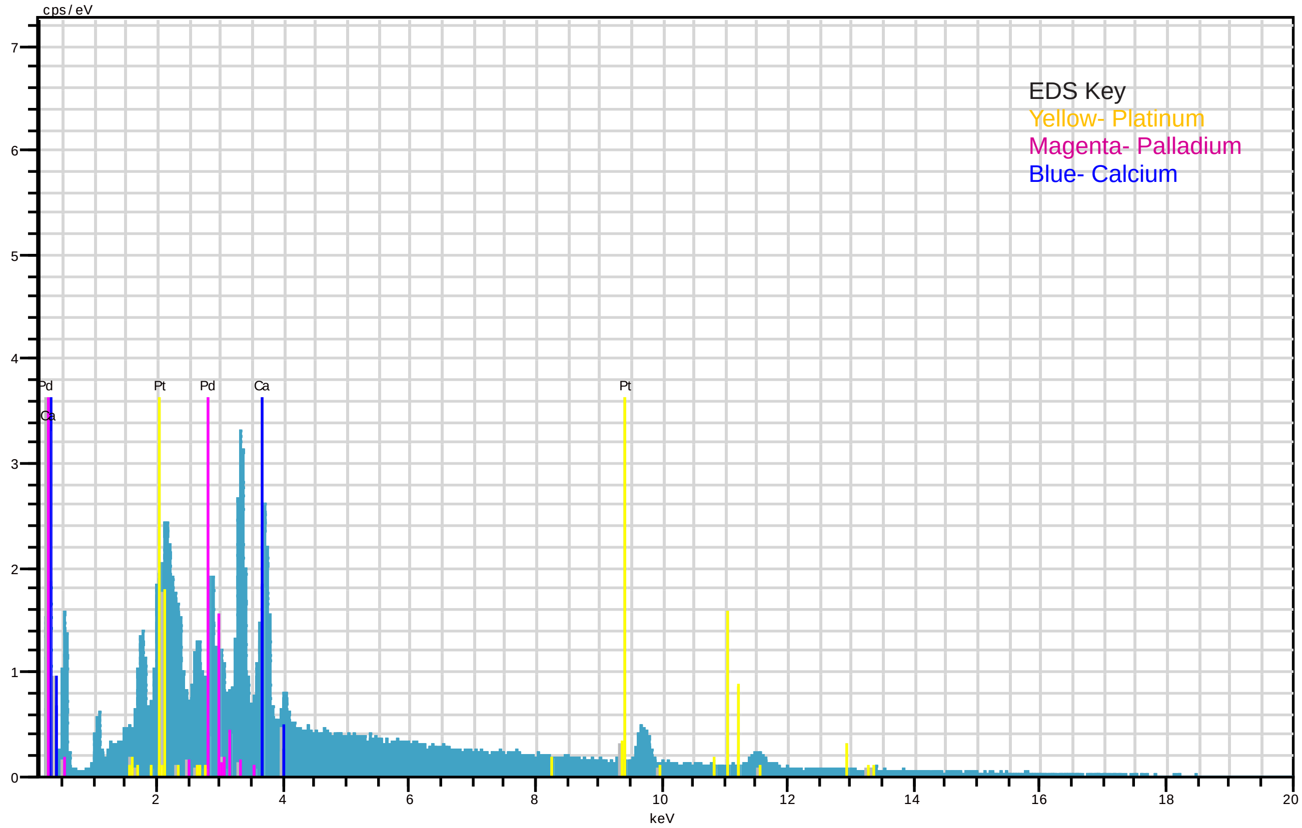

Figure 6. EDS results show calcium deposition at 5.5 V.

References

1. Chua, C. K.; Leong, K. F.; Tan, K. H.; Wiria, F. E.; Cheah, C. M. Journal of Materials in Science: Materials in Medicine **2004**, 15(10), 1113-1121.

2. Sano, M. B.; Rojas, A.D.; Gatenholm, P; Davalos, R. V. Annals of Biomedical Engineering **2010**, 38(8), 2475-2484.

3. Zimmermann, K. A.; LeBlanc, J. M.; Sheets, K. T.; Fox, R. W.; Gatenholm, P. Materials Science and Enginering C. **2009**.

4. Giannoudis, P. V.; Dinopoulos, H.; Tsiridis, E.; Injury **2005**, 36(3), 20-27.

5. Suchanek, W.; Yoshimura, M. Journal of Materials Research **1998**, 3(1), 94-117.

6. Bielecki, S.; Krystynowicz, A.; Turkiewicz, M.; Kalinowska, H. Biopolymer Online **2005**.

7. Ross, P.; Mayer, R.; Benziman, M. Microbiology and Molecular Biology Reviews **1991**, 55(1), 35-58.

About the Author

Kennedi Lowman is a native of Columbus, GA. She loves reading, writing poems, hanging with family & friends, spending time with her nieces & nephews, cooking, & playing recreational sports. Kennedi would love to travel outside of the continental US more. Fall 2010, Kennedi graduated with a Bachelor of Science degree in Biology with a concentration in Biotechnology from Albany State University in Albany, GA. In the Spring of 2015, she graduated Cum laude with a Bachelor of Science degree in Clinical Laboratory Science from Tuskegee University in Tuskegee, AL. She currently works at Northside Medical Center in Columbus, GA as a Medical Technologist. Her ultimate career goal is to become an R&D scientist. Kennedi is undecided about what she would like to further her research in right now, but cancer is at the top of her list, specifically breast cancer. Contact at: klowman87@gmail.com

Processing and Characterization Techniques for a Mica Filled Polymer Composite

Sarah Whipkey, Chance Roman, and Kevin Seay

Virginia Polytechnic Institute and State University, Department of Materials Science and Engineering,
Blacksburg, VA 24061

Abstract

Mica particulates (filler) were combined with polymethyl methacrylate (matrix) to form a polymer matrix ceramic composite (PMCC). Mica concentrations in the range of 10-80 wt% mica with particulate sizes in the range of 53-212 µm were used. Dynamic mechanical analysis was used to conduct stress/strain tests on these composites in order to observe the resulting elastic moduli with varying mica particulate size and concentration. The elastic moduli showed an overall increase with increasing mica concentration in all but one tested particulate size, which exhibited a peak modulus at 60 wt% mica filler. Statistical analysis showed that both the mica concentration and mica particulate sizes were significant to the resulting elastic moduli, as well as the interaction between these two factors. Optical microscopy was used to observe the interface between the polymer matrix and mica particulates in order to determine the degree to which the two materials bonded to each other. It was observed that the PMMA and mica showed good bonding, meaning the formed materials were successfully combined into a cohesive composite.

Keywords: Polymer matrix ceramic composites (PMCC), muscovite mica, polymethyl methacrylate (PMMA), dynamic mechanical analysis (DMA).

1. Introduction

1.1 Background

Composite materials are an important sector of materials science, as the combination of constituents in a composite allows for a range of properties that would never be achievable from the individual components.[1] Polymers are often combined with a filler material, such as a ceramic, to increase their strength and hardness, and reduce the effect of temperature on their behavior.[2]

When designing a composite material, many factors must be considered in order to achieve the desired properties. Considering a polymer matrix ceramic composite, the ceramic filler shape used can significantly alter a material's properties.[1] Filler shapes can include geometries such as spheres, blocks, flakes and fibers.[1] Filler geometries with high area-to-volume aspect ratios tend to have better mechanical properties, as the greater surface area allows for more stress transfer between the composite components.[1] One such filler material that has a relatively high aspect ratio is muscovite mica $[2Al_2K_4(Si_6Al_2)O_{20}(OH)_4]$.[3] Another critical factor of composite design involves the interfacial adhesion between the ceramic and the polymer binder.[1] This interface is typically described as the weakest point in a composite system, and therefore must be carefully considered during its design.[1] The orientation of the composite filler material is also critical in determining the composite properties.[1]

1.2 Mica-polymer Composites

Mica is used as a reinforcing filler in many polymeric composites because of its functional, morphological, and surface characteristics.[4] Mica readily breaks down into smaller thin flakes with very high area-to-volume ratios, which can be used as reinforcement in composites if properly aligned.[1] Mica powder is commonly used as reinforcement for polymer composites in products such as paints, coatings and cements to reduce sagging, shrinkage, cracking, and UV susceptibility.[1] In general, mica is characterized as being highly crystalline, having smooth surfaces between sheet layers, and being an inert material.[1]

The addition of mica to a polymer can result in significant improvements to the material properties such as raise the heat distortion temperature, increase tensile and flexural strengths, reduce isotropic shrinkage and permeability, enhance the dielectric and thermal properties, and improve surface properties.[4] Mica has been previously studied in combination with a wide variety of plastic thermosets and elastomers such as polypropylene, polyethylene, polycarbonate, Nylon 6, Nylon 66, polyester, and styrene.[4]

Mica-polymer composites are often favored due to the composite's improved strength with the addition of the mica.[1] The mica filler tends to immobilize the polymer chains, effectively preventing the polymer chains from slipping past each other, resulting in the increased strength.[1] Due to mica flakes being an inert material, there is typically no chemical bonding between mica and polymer chains, consequently the surface adhesion between the mica and the polymer is usually poor.[1] As a result, this surface adhesion must be carefully considered when designing a mica-polymer composite. In order to help improve the surface adhesion, sometimes coupling agents, which act as a binder between the polymer matrix and filler, are used in polymer composites.[1] Coupling agents that could be considered with mica to form a composite include silanes, zirconates, titanates, and stearic acid.[1] Mica-polymer composites can be formed in a variety of ways, including hot compaction, extrusion, and pultrusion.[4-6]

1.3 Previous Mica-polymer Composite Research

Polypropylene is a commonly used polymer for polymer-mica composites, and various experiments have been conducted on this composite system.[2,7,8] Mica has been shown to be a low-cost way of improving polypropylene performance by improving chemical resistance, dimensional stability, and reducing gas diffusivity, and has been applied to a wide range of uses, including automotive parts, fan blades, dashboard panels, floor and grill panels, and ignition system parts.[2,9]

Previous studies on mica-filled polypropylene showed an optimized mica concentration of 20 wt% to minimize crack propagation and increase flexural and impact strengths in the polymer composite.[2,7] The mixing parameters that have been reported to effect the mica-polypropylene system include mixing concentration, method of mica addition to the polymer, and initial particle size.[8] Corresponding to the potential breakdown of this composite system, it has also been reported that mechanical degradation is likely to occur first by the gradual weakening of larger mica flakes to form smaller flakes, and the most rapid degradation will take place when the mica is incorporated into the molten polymer resin.[8] Another related composite system has been tested with mica-filled polyester, in which the flexural strength and elastic modulus was found to increase with increasing mica concentration while the tensile strength decreased.[10]

One mica-polymer combination where previous research was not found was the use of polymethyl methacrylate (PMMA) [(C5O2H8)n] as the matrix. This polymer is a synthetic resin produced from the polymerization of methyl methacrylate.[11] A transparent and rigid plastic, PMMA is often used as a substitute for glass in products such as shatterproof windows, skylights, illuminated signs, and aircraft canopies.[11] PMMA is typically a low cost polymer material that can be easily handled and processed, however, the polymer is also typically weak and brittle under an applied stress.[11] The introduction of mica as filler into the PMMA matrix could possibly improve specific properties of the composite and open the door for new applications.

1.4 Direction of Work

The primary goal of this project is to design a repeatable ceramic-reinforced polymer composite with predictable properties in order to demonstrate the effects of added ceramic filler into a polymer matrix. Muscovite mica was chosen as a filler material with PMMA to form a polymer matrix ceramic composite (PMCC). Dynamic mechanical analysis (DMA) was used to measure the elastic modulus and tensile strength of the composite system as the wt% and particulate size of the filler material varied. Optical microscopy was also performed to determine the degree of bonding between the matrix and the filler in the fabricated composites. The various experimental stages are described succinctly in the section that follows.

2. Experimental Procedure

2.1 Dry Ball Milling of Mica Flakes

The mica material was received in flakes from the supplier in the approximate particle size range of 3-7 mm. The subsequent particle size reduction was done by dry ball milling in which 100 grams of mica were placed in an alumina milling jar with alumina milling media and placed in the roll mill machine. The roll mill was set to 50% the maximum rotational speed and run for approximately 24 hours.

2.2 Particle Size Distribution of Mica Flakes

After ball milling, the mica particulates were sieved according to AFS standard 1105-03-S to obtain specific particle size ranges. The sieved particles were separated into twelve flake sizes in the range of greater than 3 mm to less than 53 μm.

2.3 Uniaxial Pressing of Samples

Using a standard laboratory analytical scale, mica percentages were weighed and mixed with PMMA. Samples of concentrations of 10-80 wt% mica were made using five mica particulate sizes in the range of <53 μm to 212 μm, and a reference sample of 100% PMMA was also created.

The samples were pressed using a Buehler TechPress II® with an isooctane Buehler release agent applied to all surfaces interacting with the material to ensure easy release of the sample after pressing. The press was programmed with a 7 minute preheat phase to 165°C. Samples were then heated to 177°C, followed by an 11 minute cooling cycle, held at a constant pressure of 3700 psi. The polymer in the pressed sample had a hard consistency and a colorless-transparent appearance which made further sample preparations (e.g., cutting and polishing) and visual observations of the imbedded mica easier.

2.4 Dynamic Mechanical Analysis (DMA)

The pressed samples were cut using a low speed cutting saw (Buehler Isomet®1000) into rectangular samples approximately 37 mm long, 2 mm wide and 0.5 mm thick. Three samples of each pressed composite were tested in a TA Instruments Q800 DMA system under ambient conditions. Stress/strain tests were conducted using an 8 mm dual cantilever clamp to hold the samples. Run conditions were a preload force of 0.001 N, a force ramp rate of 2 N/m^3, and an upper force limit of 18 N. The tests were run until the sample fractured or the force reached the maximum possible by the DMA system (18N).

2.5 Optical Microscopy of Component Interface

Two PMCC samples with 10 wt% mica filler were mounted into an epoxy using metal clips to ensure the samples maintained a flat surface against the bottom of the mounting cup. These samples were placed under vacuum at 93 kPa with a cup of epoxy liquid mounting media mix, in order to remove as much air from the epoxy as possible. After evacuation, the epoxy was poured into the cup with the samples, brought to atmospheric pressure, and allowed to cure overnight. The encapsulated samples were ground and polished using a Buehler Ecomet 3® polishing unit with 400 and 600 grit sandpaper for 3 minutes. Further polishing was completed using 12.5, 5, and 1 µm alumina polishing media and water mixture for 5, 10, and 30 minutes respectively on a Buehler TexMet® pad. Optical microscopy was then used to observe the interface between the mica particulates and PMMA, as well as the orientation of the mica particulates in the polymer matrix.

3. Results & Discussion

3.1 Dynamic Mechanical Analysis

Shown in Figure 1 is a representative stress/strain data plot for the tested samples using the TA Instruments Universal Analysis software. The figure shows one PMMA sample with no mica filler (dashed line) and one sample with a 10 wt% filler mica of 53-75 µm size (solid line). The elastic moduli were determined for the tested samples from the linear sections of the stress/strain plots. Each sample condition was replicated three times, and the average elastic moduli values for each replication condition are shown below in Figure 2. As the mica filler concentration increased in the samples, it became more difficult to produce viable composites, as the samples crumbled immediately after pressing. Due to this effect, only four of the five mica particulate sizes were pressed for the 70 wt% mica filler samples and one of the five particulate sizes was pressed for the 80 wt% mica filler samples.

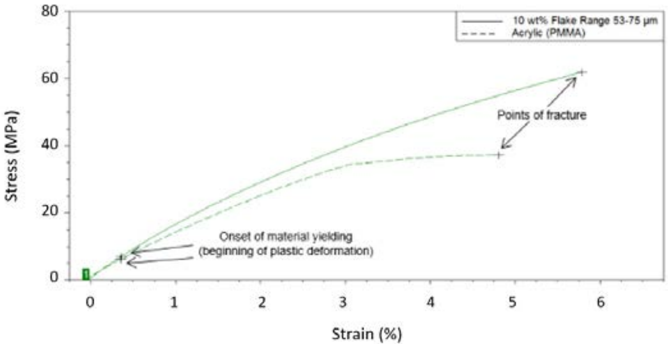

Figure 1: Stress-Strain graphs for one PMMA sample and one composite sample with a 10 wt% of 53-75 µm mica filler.

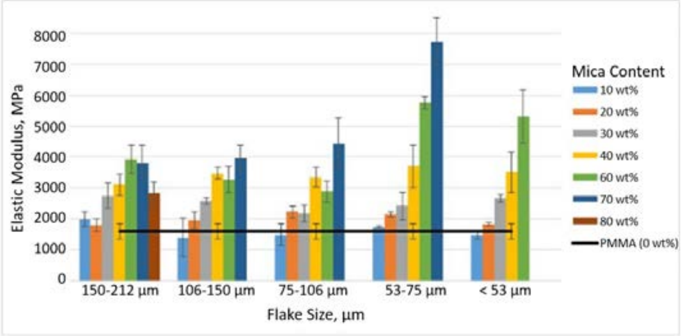

Figure 2: Average elastic moduli (ordered by decreasing mica particulate size and by increasing mica concentration).

Figure 2 shows the average elastic modulus for each sample concentration tested, sorted by the mica particulate sizes. It is noted that there is an overall increasing trend in elastic moduli with increasing mica filler concentration. The largest mica particulate size samples (150-212 µm) showed that a maximum elastic modulus was reached at 60 wt% mica filler, with a decrease in modulus to the 70 and then 80 wt% mica filler samples. The next two smallest mica filler particulate size ranges (106-150 µm and 75-106 µm) showed a slight decrease in modulus from 40 to 60 wt% mica filler, followed by another increase in modulus with the 70 wt% mica filler samples. The increase in elastic modulus was expected to a point, where a peak modulus was anticipated before a decrease in modulus, like the behavior observed in the largest flake size samples. The overall increase seen in the other four flake sizes was not expected.

Compared to the pure PMMA samples tested (shown by the black horizontal line in Figure 2), the 10 wt% mica filler samples demonstrated elastic moduli similar to that of PMMA, while the increasing mica concentration samples showed a steady increase from the elastic modulus of the PMMA samples with increasing mica concentration.

A two-way analysis of variance was conducted for the experimental elastic moduli with mica concentration and particulate size as two independent variables. It was determined that both concentration and flake size were significant to the experimental results, as well as the interaction between the two. When observing the elastic moduli results across varying flake sizes, a relationship is not as clear as the overall trend of increasing elastic modulus with increasing concentration. The statistical interaction between the flake size and concentration most likely contributes to the lack of a clear trend with varying flake size.

3.2 Optical Microscopy

Optical microscopy was conducted on mounted samples to observe both the mica particulate orientation and mica-polymer matrix adhesion. Figure 3 shows the orientation of the mica flakes for the 10 wt% mica filler sample with 150-212 µm particulate size range. The figure shows that the mica flakes seem to have developed a degree of orientation in the transverse direction to the uniaxial press during the composite formation. This orientation also means that the samples were tested mechanically in the transverse direction to the force applied.

After the orientation of the mica was observed, the adhesion of the mica to the PMMA was investigated at various magnifications. This observation was done by looking at a fractured sample with a larger mica flake size than the five tested flake size ranges in order to facilitate observations. The fractured sample in Figure 4 shows component adhesion with no delamination between the mica and polymer, demonstrating that the PMMA and mica successfully bonded together to form a cohesive composite.

4. Conclusion

When polymethyl methacrylate is reinforced with mica filler, the overall elastic modulus increases with increasing mica filler concentration. Both the mica concentration and particulate size were shown to be statistically significant to the resulting elastic modulus, as well as the interaction between the two. It is unclear as to why there was not a peak modulus observed followed by a decrease with increasing mica concentration, which was expected due to the matrix eventually becoming more mica filler than PMMA. This effect was observed in previous literature,however, the experiment showed that only one of the mica flake sizes behaved in this way, while the others showed an overall increasing elastic modulus with increasing mica concentration.[2,7,8,10]

Optical microscopy on the fractured composite surface showed that a significant bond formed between the PMMA and mica particulates and that there was no need to utilize a coupling agent to develop the bonding. The lack of separation between the polymer matrix and the mica particulates in the fractured composite showed that mica has a strong binding affinity with PMMA. This allowed for a truly cohesive composite to be formed rather than particulates present within another material as two separate entities. Overall PMMA and mica are able to be combined into a repeatable composite that can be used to demonstrate the behavior of polymer matrix composites.

5. Future Work

In order to continue this experiment towards the development of a repeatable composite system, further testing would be needed to characterize the properties of the composite from this work. Further mechanical testing would be useful, such as the mechanical properties of the composite system in tension, since only bending was observed in this experiment. Other orientations of the applied test force are possible to be tested as well, e.g. parallel and oblique. Thermomechanical

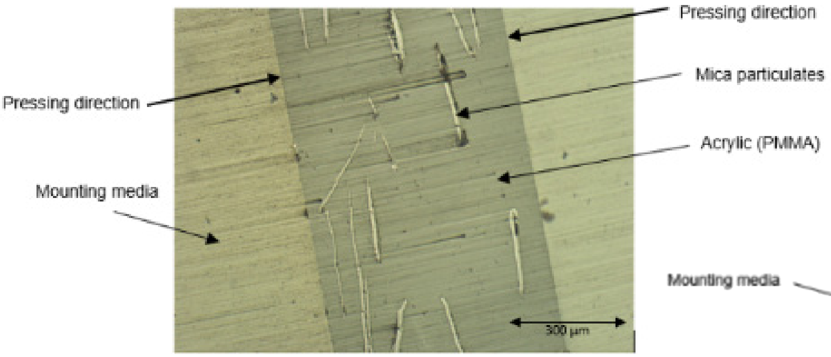

Figure 3: Orientation of mica particulates for 10 wt% mica filler samples with 150-212 µm particulate size range.

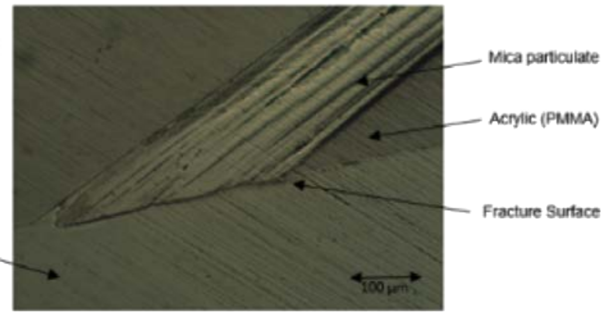

Figure 4: Fractured adhesion surface of the PMMA and mica filler particulate for 10 wt% mica sample with 150-212 µm particulate size range.

testing could also be done to observe how the composite behaves under varying temperature conditions, as only ambient temperatures were tested in this study due to time restrictions. The electrical properties of the composite could also be analyzed, as both mica and PMMA are insulating materials, and the possibility exists for the composite to be a successful insulator. With a range of these properties tested and recorded, a system could be developed for the two components in which certain properties could be optimized for specific polymer/composite applications in the future.

Acknowledgements

This project was conducted as part of a senior design project with the guidance of Dr. Carlos Suchicital and Dr. Thomas Staley. Further thanks goes to Mr. Hesham Elmkharram and the graduate teaching assistants at Virginia Tech for their laboratory support and to the Materials Science and Engineering Department at Virginia Tech for their support for this project.

References

1. Mallick, P.K. Fiber-Reinforced Composites, Marcel Dekker, Inc.: New York, **1993**.

2. Vu-Khanh, T.; Sanschagrin, B.; Fisa, B. Polymer Composites. 1985, 6, 249-260.

3. Norton, F. H. Elements of Ceramics, 2nd ed.; Addison-Wesley Publishing Company: Massachusetts, 1974.

4. Verbeek, J.; Christopher, M.; Thomas, S.; et al. Mica-Reinforced Polymer Composites. In Polymer Composites; Ed.; Wiley-VCH: Germany, 2012; Vol. 1; pp 673-714.

5. Michler, G.H.; Balta-Calleja, F.J. High Stiffness and High Impact Strength Polymer Composites by Hot Compaction of Oriented Fibers and Tapes. In Mechanical Properties of Polymers based on Nanostructure and Morphology; Ed.; Taylor and Francis Group: Florida, 2005; pp 683-722.

6. Bader, M.G. Reinforced Thermoplastics. In Handbook of Composites: Fabrication of Composites; Ed.; Elsevier Science Publishing Company, Inc.: New York, 1983; Vol. 4; p 177-218.

7. Xavier, S.F.; Sharma, Y.N. Polymer Composites **1986**, 7, 42-49.

8. Fisa, B.; Sanschargrin, N.; Favis, B. Polymer Composites **1984**, 5, 264-276.

9. Mica Composite. http://www.micaworld.in/micacomposite.html (accessed April 27, 2014).

10. Sreekanth, M.S.; Bambole, V.A; Mhaske, S.T.; Mahanwar, P.A. Journal of Mineral and Materials Characterization and Engineering **2009**, 8, 271-282.

11. Encyclopedia Britannica Online. Polymethyl methacrylate (PMMA). http://www.britannica.com/EBchecked/topic/1551203/polymethyl-methacrylate-PMMA. (accessed May 4, 2015).

About the Authors

Sarah Whipkey graduated with a Bachelor of Science from the Department of Materials Science and Engineering at Virginia Tech in May 2015. She has been accepted into the graduate program at Alfred University for ceramic engineering beginning Fall 2015.

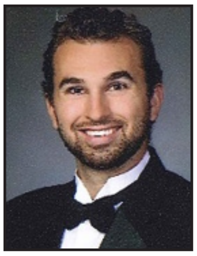

Chance Roman graduated with a Bachelor of Science from the Department of Materials Science and Engineering at Virginia Tech in May 2015. He has accepted a position with Freeport McMoran: Copper & Gold in Bagdad, Arizona.

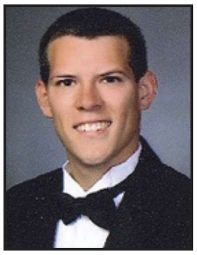

Kevin Seay graduated with a Bachelor of Science from the Department of Materials Science and Engineering at Virginia Tech in May 2015. He will be working for Kratos Defense and Security Solutions Inc. at Dahlgren Naval Base in Virginia.

Crossword

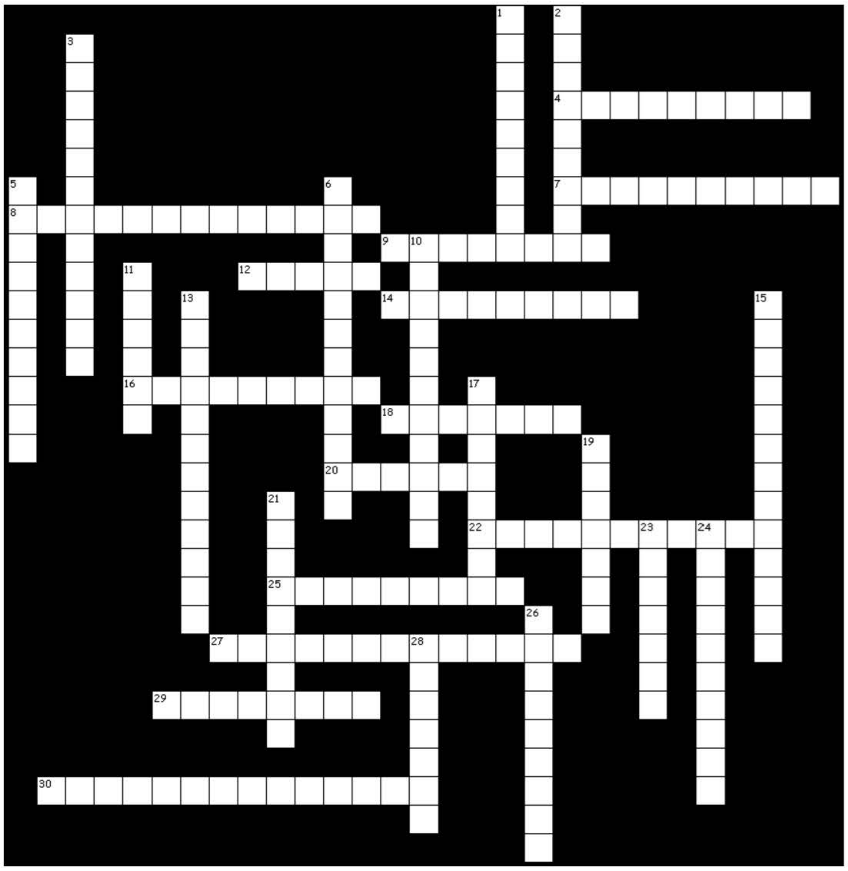

Across

4 A resource that is not depleted when used.

7 Ability of a material to dissolve in a solvent such as water, alcohol, acid, or others.

8 Property of a material that kills bacteria and other microorganisms and inhibits their growth.

9 Ability of a material to withstand applied stress without failure.

12 A mixture of metals or a metal and another element. Defined by metallic bonding character.

14 A material that has no long range order or repeating structure.

16 A material made from two or more constituent materials.

18 A point defect in a crystal where an atom is missing.

20 A material phase that takes the shape of its container and maintains nearly constant volume independent of pressure.

22 A reaction or process that requires or is accompanied by the absorption of heat.

25 Ability of a material to absorb energy and plastically deform without fracturing.

27 A material that is not harmful to living tissue.

29 A container in which metals may be melted.

30 Small scale structure of a material which can be revealed by a microscope.

Down

1 The net movement of atoms or molecules down a chemical potential gradient.

2 A polymer with many cross-linking branches in the molecule.

3 Opposite of resistivity

5 The distance between any two points in a wave with the same phase.

6 A particle having at least one dimension smaller than 100 nm.

10 A measure of the average kinetic energy of molecules or atoms in a system. Hint: measured with a thermometer.

11 To rapidly cool a hot metal casting or forging by dipping into a cooling medium such as water or oil.

13 The degree of magnetization that a material undergoes in response to an applied magnetic field.

15 A material that generates charge in response to an applied mechanical stress.

17 Material property that resists permanent deformation from scratching or indentation.

19 Repeated 3-dimentional arrangement of atoms in a solid.

21 Having properties that are invariant with respect to direction.

23 A system's thermal energy per unit temperature that is unavailable for conversion into mechanical work. Can also be viewed as the degree of disorder in a system.

24 A study of the physical and chemical properties of metals and their production.

26 Tissue that is surgically transplanted from one person to another.

28 Porous ultralight material derived from a gel by replacing the liquid in the gel with a gas.

Find the solutions online at: jumr.mse.vt.edu

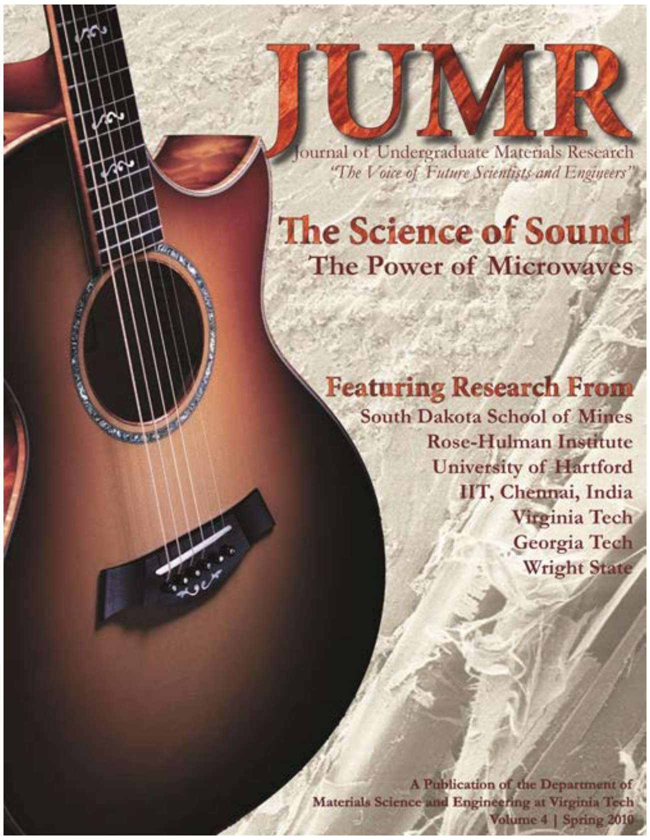

JUMR

Journal of Undergraduate Materials Research

"The Voice of Future Scientists and Engineers"

The Science of Sound

The Power of Microwaves

Featuring Research From

South Dakota School of Mines

Rose-Hulman Institute

University of Hartford

IIT, Chennai, India

Virginia Tech

Georgia Tech

Wright State

A Publication of the Department of

Materials Science and Engineering at Virginia Tech

Volume 4 | Spring 2010

PUBLISH.
GAIN RECOGNITION.
BE PART OF SOMETHING EXCITING.

Submit your paper for consideration in Volume 6

If you are an undergraduate student at any institution working on a materials-related project, here is your chance to become published. Your submitted paper will undergo a peer-review for consideration in Volume 6 of the Journal of Undergraduate Materials Research.

JUMR is an open access journal focused on giving undergraduate researchers a peer-reviewed platform to present their research.

All the articles in JUMR are written by undergraduates from universities around the world, including the feature articles, which focus on a single aspect of materials science and engineering.

Undergraduates with projects involving materials research, design, or characterization are encouraged to submit their work and experience an important part of academia.

More information, including instructions for submission, past publications, and the people who make this possible can be found at www.jumr.mse.vt.edu.